STRESS MAPPING OF TEXTILE COMPOSITE MATERIALS AND ITS

APPLICATION IN INTERFACIAL SHEAR BEHAVIOR

Except where reference is made to the work of others, the work described in this dissertation is my own or was done in collaboration with my advisory committee. This dissertation does not include proprietary or classified information.

_____
Ebraheem Hassan E. H. Shady

Certificate of Approval:

_____   _____
Peter Schwartz   Yasser Gowayed, Chair
Professor   Professor
Department of Textile Engineering   Department of Textile Engineering

_____   _____
B. Lewis Slaten   Stephen L. McFarland
Professor   Dean
Department of Consumer Affairs   Graduate School

STRESS MAPPING OF TEXTILE COMPOSITE MATERIALS AND ITS

APPLICATION IN INTERFACIAL SHEAR BEHAVIOR

Ebraheem Hassan E. H. Shady

A Dissertation

Submitted to

the Graduate Faculty of

Auburn University

in Partial Fulfillment of the

Requirements for the

Degree of

Doctor of Philosophy

Auburn, Alabama
December 16, 2005

STRESS MAPPING OF TEXTILE COMPOSITE MATERIALS AND ITS

APPLICATION IN INTERFACIAL SHEAR BEHAVIOR

Ebraheem Hassan E. H. Shady

_____
Signature of Author

_____
Date of Graduation

DISSERTATION ABSTRACT

STRESS MAPPING OF TEXTILE COMPOSITE MATERIALS AND ITS

APPLICATION IN INTERFACIAL SHEAR BEHAVIOR

Ebraheem Hassan E. H. Shady

Doctor of Philosophy, December 16, 2005
(M. S. Mansoura University, Egypt, 1998)
(B. S. Mansoura University, Egypt, 1993)

168 Typed Pages

Directed by Yasser A. Gowayed

Mapping of the stress distribution in composite materials, both at the fiber/matrix interface and at the composite constituents themselves, is important to understand the material mechanical response. Stress mapping can help predict composite behavior under certain stresses especially failure or delamination. In this work, two analytical models were proposed to map the stress distribution at fiber, matrix and fiber/matrix interface. The first model dealt with the fiber in the longitudinal direction considering axisymmetric conditions. The second model addressed the fiber stress distribution in the transverse direction. Both models were verified using finite element models.

As an application for the stress mapping models, interfacial shear behavior was chosen for its importance in modeling and design of composite materials. Two fabric structures were used to manufacture five different panels for each fabric. The number of fabric layers for each plate ranged from 5 to 9 layers systematically altering the volume fraction and nesting characteristics of each plate. Four-point flexural tests were used to obtain a pure bending state between load noses. The maximum tensile stress and crack initiation stress at the bottom layer were experimentally evaluated.

Experimental data was processed using the Graphical Integrated Numerical Analysis software (pcGINA) to obtain the maximum stress in the target laminate and this value was used as the input for the two analytical models. The value for the maximum interfacial shear stress which is responsible for crack initiation in the laminate was calculated using the models and results were compared to pull-out fiber test values obtained from literature. Good agreement was observed between the model results and the literature data.

ACKNOWLEDGMENT

First of all, I would like to thank Allah (God), all mighty, for his guidance and all his gifts.

I am deeply indebted to my advisor, Professor Yasser Gowayed, for his constant support, allowing me to pursue my research in the manner that I saw fit and believing in me when even I didn't know what I was doing. He was always there to support me with his encouragement and many fruitful discussions.

I would like to thank the committee members and the faculty and staff of the Department of Textile Engineering. I also like to thank all my professors in Auburn University and in Mansoura University in Egypt.

Finally, I would like to thank all my family, specially my mother, because without her I wouldn't even be where I am today and my father, may Allah bless his soul, who encouraged and supported me when I decided to direct my career towards research and teaching. Special thanks are due to my wife Amany for her presence beside me and endless support which continues to give me strength.

Style manual or journal used: Experimental Mechanics, Composites Science and

Technology, Serial Title Abbreviation followed as in Elsevier Engineering

Information on World Wide Web (www.engineeringvillage2.org)

Computer Software used: Microsoft Word XP, Microsoft Excel XP, ANSYS 7.0,

MATLAB 7.0 and pcGINA

TABLE OF CONTENTS

LIST OF FIGURES

xv

LIST OF TABLES

I. INTRODUCTION

1.1 Background

In the last two decades, textile composites showed a potential for enhancing the drawbacks of the conventional unidirectional composites due to their integrated yarn architecture. One of the main classes of textile composite is woven-fabric composite, which consists of two groups of yarns, known as warp and weft, interlaced at right angles giving woven-fabric composites several advantages over unidirectional fibrous composites:

- Low production costs can be achieved.
- The handling of woven fabrics is relatively easy.
- The weaving and interlacing of the yarns creates a self supporting system that can be controlled to form complex shapes.
- Mechanically, the geometry of a fabric provides bi-directional stiffness in the plane of loading, superior impact tolerance and good interlaminar stiffness in the out of plane direction.

However, these advantages are at the cost of reduced overall in-plane stiffness properties due to the undulation (crimp) of the yarns.

1

Currently, most woven-fabric structures used are plain, twill and satin weaves for their simplicity in design and manufacturing. However, changing fabric architecture can achieve the best possible combination of cost, weight, thickness, in-plane and out-of-plane stiffness and strength properties. This can be accomplished by changing the weave structure, fiber type, yarn count, etc. There are unlimited number of possible architectures.

The combined requirements of lightweight and high strength in many civil and military applications under high strain rate loading conditions open the field of woven fabric composites to be used as structural materials. Furthermore, textile composites show significant tolerance to damage before failure which may include different interacting modes, such as matrix cracking, interfacial sliding, and fiber damage in different positions occurring simultaneously and over small spatial and sequential scales. The local stress and strain fields accompanied with these phenomena are difficult, if not impossible, to be obtained experimentally. Hence, accurate, predictive analytical tools are required to give insights into the original physical mechanisms relating to damage.

Analysis of failure in composite materials has traditionally followed two different levels:
- Micro-mechanics.
- Macro-mechanics.

The micro-mechanics approach considers microscopic inhomogeneities and direct interaction of composite constituents at the micro-structure level. The advantage of the

2

micro-mechanics approach is that detailed information can be directly obtained about the local interaction between composite constituents. However, the numerical modeling combined with complicated fiber geometries often requires exceedingly fine grids and hence results in excessive computing cost.

Many models attempted to address micro-mechanical analysis at a manageable level. However, this is done by oversimplifying the mechanical behavior of the constituents, which leads to inaccurate results. Conducting stress analysis in practical composite laminates with the presence of million of fibers using micro-mechanical approach is a daunting task beyond the computational capacity of even the most-advanced supercomputers. Hence, current micro-mechanical models are mainly restricted to the strength prediction at the lamina level or unidirectional composites.

In the macro-mechanics approaches, the overall constitutive descriptions are developed from composite micro-structure in terms of the volume fraction, weave structure, and the interface conditions of the constituents. The mechanical properties of woven-fabric composites have high dependence upon the reinforcing yarn geometry and weave structure. It is necessary to create a geometric model for describing the fiber architecture and weave structure. The woven fabric can be treated as an assembly of unit cells which represents the smallest repeating pattern in the fabric structure. The unit cell includes sufficient details to represent the fabric geometry.

It is important to highlight the hierarchal nature of structural analysis, unit-cell models and micro-level models. Such relationship is similar to that of local-to-global finite element analysis but with an additional layer of analysis. At the composite part level, structural analysis, such as Finite Element Analysis, can define stress and strain distributions around holes, attachments, etc. These stress and strain values do not include the local effect of fiber/fabric geometries at the unit cell level. Utilizing information provided by structural analysis, unit-cell models are able to implement the effect of geometries and define average stress and strain distributions within a repeat unit cell. Micro-level models use the information provided by unit-cell models to map stress and strain distributions for fibers, matrix, fiber/matrix interface, etc. For example, for a composite plate with a hole, structural analysis will define stress and strain distribution around the hole treating the composite as an orthotropic material. Unit cell models utilize this information to map the stress and strain distributions to yarns and resin-pocket. Stresses and strains at the fiber level and fiber/matrix interfaces are further evaluated using micro-level models.

1.2 Objectives

The objective of this study, in summary, is to develop a novel closed-form micro-level stress/strain mapping for composite materials and merge it with a unit-cell level numerical approach. The procedure to reach this target will be as follow:

i.   Develop analytical models to map the stress distribution in the composite constituents, i.e. fiber, interface and matrix.

ii.   Verify analytical models with numerical tools such as FEM.

iii.   Connect these models to the unit-cell level numerical model

iv.   Implement the new combined model to understand interfacial shear stress distribution in woven laminates

v.   Manufacture composite samples and conduct four-point bending test to verify the analytical results with experiments. The four-point bending test is used to quantify the interlaminar shear strength of textile composite.

1.3 Organization of the dissertation

This study is presented in six chapters including this introduction chapter. The second chapter contains review of the literature focusing on numerical modeling and closed form solutions in fiber reinforced composites in general. The third chapter introduces the analytical models and their verifications. The fourth chapter covers the experimental work which includes manufacturing of composite samples and conducting the four-point bending test. The fifth chapter discusses the test results and compares the experimental data to analytical results. The sixth chapter concludes this work and presents recommendations and suggestions for future work.

II. REVIEW OF LITERATURE

2.1 Introduction

To improve composite reliability and damage tolerance for advanced structure applications reasonable through thickness and interlaminar strengths are required. Using woven-fabric composites can achieve such requirements. Also, the ability to precisely customize the composite micro-structure through efficient and accurate modeling can expand the material use rapidly.

In the mechanics of heterogeneous materials there is an interest in computing micro-level stress and deformation fields to understand their local failure and damage. A major need in the design of woven fabric composites is to assess suitable stress levels under the conditions to be experienced during service. For this class of composite, the computation of the local distributions of stresses in the fiber and matrix is considerably more complex than for unidirectional ply laminates due to the interlacing of the fiber tows. Limited attempts have been carried out on woven composites modeling and analysis. For more complicated and advanced applications, especially those concerned with damage tolerance, information about local distributions of stresses in the fiber and matrix constituents are of main importance.

2.2 Review of existing models for stress-mapping

In this section a quick review of research works dealing with mapping of stress mapping at a unit-cell level, as well as, fiber, matrix and fiber/matrix interface will be presented. As previously mentioned, the approaches that deal with stress mapping can be divided into two main categories, micro-mechanics and macro-mechanics approaches. Each of these approaches can use either closed form solution or numerical analysis.

2.2.1   Micro-mechanics models

Micro-mechanics approaches deal with composite constituents at a micro-structure level to obtain local interaction information such as elastic properties and stress and strain distributions. The main drawback to using these models with textile composites is their focus on fibers or inclusions surrounded by matrix without considering the effect of the preform architecture. In most approaches, the link between the micro-mechanical model and the geometry of the fabric preform does not exist. This may have a minor effect on prediction of the composite elastic constants, however, it may lead to unrealistic stress and/or strain mapping.

2.2.1.1 Composites with inclusions

The effect of inclusions on the stress distribution in homogeneous materials has been studied extensively due to its importance in deformation and failure analysis of advanced

heterogeneous composites. Eshelby's work (1957, 1959) on the effect of elastic inclusions forms the foundation of several methods developed to analyze the response of composite materials. In his work, Eshelby solved the general problem of elastic field inside and at the interface of an ellipsoidal inclusion bounded by an infinite matrix domain. He concluded that the stress field inside the inclusion is uniform and the interfacial stress in the matrix may be readily evaluated in terms of equivalent transformation strains.

Weng and Tandon (1984, 1986) adopted the analysis derived by Eshelby to derive an expression for the stress distribution in a matrix with inclusions. The idea of their approach is based on the concept that under a given applied external stress the average stress in the matrix is perturbed from the applied stress due to the presence of oriented inclusions with different aspect ratios and moduli, figure 2-1. The matrix and inclusions are assumed to be linearly elastic and homogeneous. The matrix is assumed isotropic while the inclusions can be treated as anisotropic and well separated. The volume average of the perturbed parts over the matrix and the inclusions has to vanish to satisfy the equilibrium conditions. The solution is derived by replacing the inclusion with a material similar to the matrix material subjected to the same boundary stresses. Stress is calculated as two parts; average and perturbed. The perturbed stress is the result of the transformation of inclusion material from the matrix material to the inclusion material. The effect of inclusions on each other as a form of stress concentration was not considered in this model.

Matrix
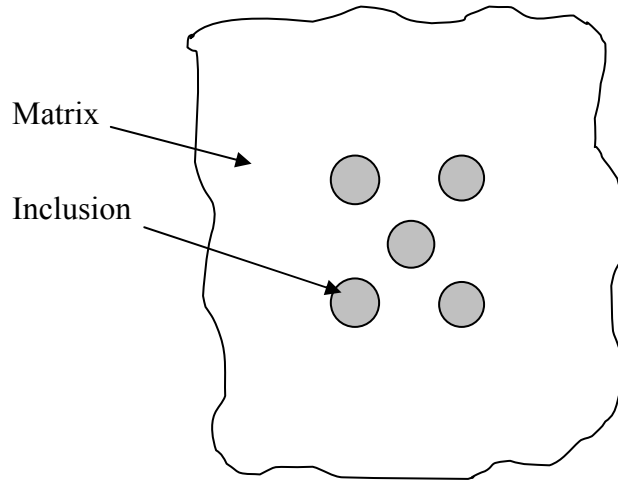
Inclusion

Figure 2-1. Composite reinforced with aligned inclusions (Weng 1984)

Hashin (1991) investigated the effect of imperfect interfaces on the mechanical properties of the composite by representing the interface imperfection as a thin compliant interphase with much lower elastic moduli.

Molinari and El Mouden (1996) derived an analytical approximate model to account for the interaction between the inclusions at finite concentrations. The model determined the overall elastic properties and local stresses of a composite material. The material considered is composed of elastic ellipsoidal homogeneous inclusions, possibly of different phases, distributed in a homogeneous elastic matrix. This approach was based on the work of Zeller and Dederichs (1973), who formulated the problem of heterogeneous elasticity in terms of an integral equation. From that integral equation, and by taking the homogeneous matrix as a reference medium, the average stresses-strains in the inclusions was obtained as solutions of a linear system of equations.

9

Wu *et al.* (1999) presented a micro-mechanical model to predict the stress fields and the elastic properties for three-phase materials with imperfect interfaces, based on the "average stress in matrix" concept derived by Mori and Tanaka (1973). This approach represented the local fields in a coated inclusion embedded in an unbounded matrix medium subjected to the average matrix stresses/strains at infinity. Equations to calculate the effective elastic moduli for this kind of composite were also derived. The resulting effective shear modulus for each material and the stress fields in the composite were presented for a transverse shear loading situation.

Honein *et al.* (2000) used a derived solution (Honein *et al.*, 1992a, b) of two circular elastic inclusions under anti-plane shear deformation to evaluate the material forces, the expanding and the rotating moments acting on inclusions, figure 2-2. The inclusion/matrix interface is assumed to be perfectly bonded. The J, L and M path-independent integrals were used to perform the calculations.
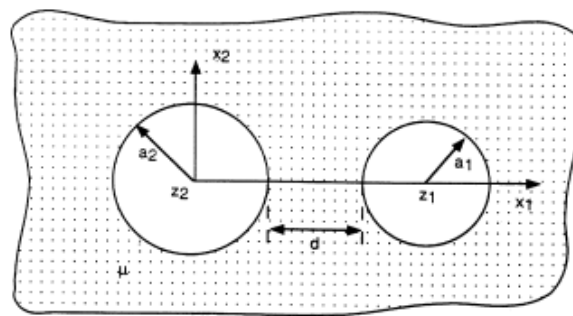
Figure 2-2. Two circular inclusion under arbitrary ant-plane deformation (Honein *et al.* 2000)

10

2.2.1.2   Fiber reinforced composites

Meguid and Zhu (1995) examined the elastic behavior of two dissimilar materials containing circular inhomogeneities near their interface finite element analysis, figure 2-3. In this study a novel finite element approach using the complex potentials of Muskhelishvili was formulated and the stress field resulting from the presence of a single and two interacting inhomogeneities near the interface of two dissimilar materials was examined. The effect of the direction of the externally applied load upon the resulting stress concentration at the inhomogeneities was evaluated.

Abdelrahman and Nayfeh (1998) extended their analysis (Nayfeh and Abdelrahman, 1997) on the stress distribution in straight fiber reinforced composites to cases involving undulated fiber reinforcement, figure 2-4. The undulation is assumed to be restricted to a single plane. They identified and analytically described local tangents to the fiber for a given geometric undulation. The global coordinates were transformed and the loads were applied to the local coordinate systems including the tangent directions and their normal in the plane of undulation. Results obtained for straight fibers were used to straight segmented fiber segments along the tangents and supplemented by local stresses that inherently rise in oriented direction with respect to the loading direction.
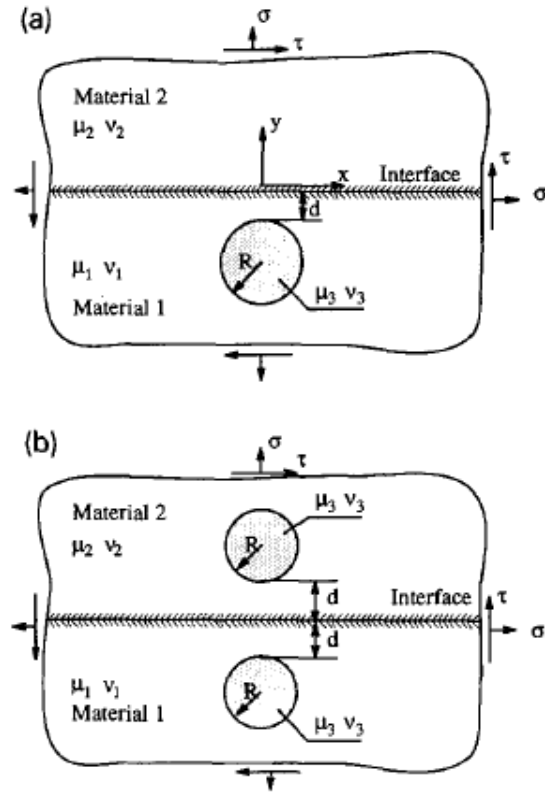
Figure 2-3. Two dissimilar materials containing: (a) one single inhomogeneity near interface; and (b) two interacting inhomogeneities across interface, (Meguid and Zhu 1995)
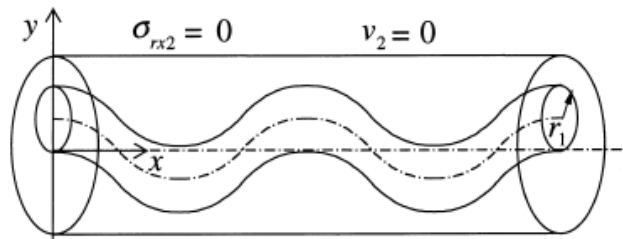
Figure 2-4. Representative unit cell (Abdelrahman and Nayfeh 1998)

Cheng *et al*. (1998) developed a method to determine the local elastic field and the overall elastic behavior of a heterogeneous medium based on the singular integral equation approach via a Green's function technique. This technique is used to solve a problem of a rectangular packed composite with square fibers. The Eshelby tensor and the contour integral are used to solve the problem. The singular integral was evaluated in closed form for assumed polynomial strain distributions.

Cheng *et al*. (1999-a) proposed an approximate superposition technique to calculate the stress fields around individual fibers in composite materials. This method uses the closed form solution for an isolated fiber to construct the local stress and strain fields, figure 2-5. The problem is formulated in terms of eigenstrains and Green's function solutions. The resulting local fields are validated by comparing the results to results from a method based on singular integral equations. The proposed method is general and can be used for periodic fiber arrangements.
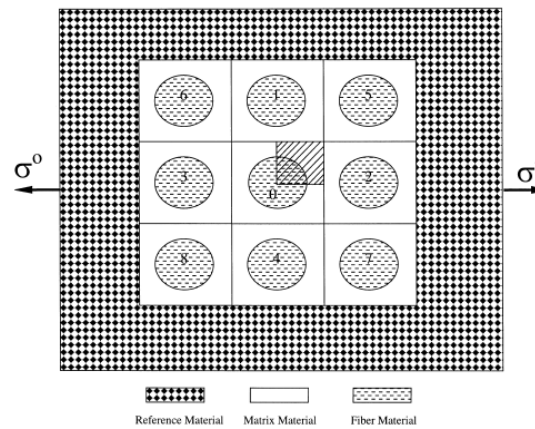
Figure 2-5. Reference fiber 0 and its eight nearby neighbor fibers, 1–8, embedded in the reference media (Cheng *et al*. 1999-a)

Cheng *et al*. (1999-b) also used Green's function approach to express the stress field for an infinite isotropic matrix material with a rectangular inclusion under a quadratic polynomial eigenstrain as an integral formula. This integral is non-singular for exterior points of the inclusion and can be evaluated in a closed form, while the integral is singular for interior points of the inclusion. This singular integral yielded a closed form expression for the interior region. Therefore, the stresses at both interior and exterior points of the inclusion were determined analytically.

Morais (2001) presented a model to predict the stress distribution along broken fibers in a unidirectional composite, figure 2-6. It was assumed that the matrix behaved in an elastic/perfectly-plastic manner and that the interfacial shear strength is not lower than the matrix shear yield stress. The model is based on a concentric cylinder approach where the composite is treated as a hollow cylinder surrounding the fiber. Axisymmetric stress analysis was performed. Polar coordinates were used to set the equations of the stress equilibrium along the debonded length, and the formulated second order differential equation was solved. The integration constants were calculated from the assumed boundary conditions, equilibrium, continuity and the system boundary conditions.

Benedikt *et al*. (2003) examined the visco-elastic stress distributions and elastic properties of unidirectional graphite/polyimide composites as a function of the volume fraction of fibers. They determined the stress distributions using two different methods - a finite element method (FEM) where the fiber arrangements were assumed to be either square or hexagonal and a Eshelby/Mori and Tanaka approach to account for the

presence of multiple fibers. The showed that the Eshelby/Mori-Tanaka approach can be used for the calculations of stresses inside and outside graphite fibers in case the volume fraction of the fibers does not significantly exceed 35% in the case of the square fiber array and 50% for the hexagonal fiber distribution. Also, it was shown that the elastic properties of unidirectional graphite/polyimide composites can be accurately determined using the analytical Eshelby/Mori-Tanaka method even for large volume fractions of fibers.
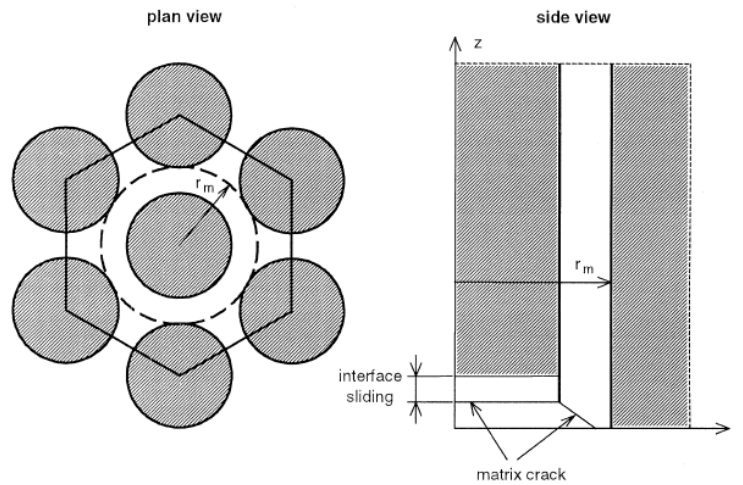
Figure 2-6. Schematic of the model (Morais 2001)

Akbarov and Koskar (2003) studied the stress distribution in an infinite elastic body containing two neighboring fibers. Both fibers are located along two parallel lines and each of them has a periodical curve with the same period. The curving of each fiber is out of phase with the other, figure 2-7. Uniformly distributed normal forces act in the direction of the fibers at infinity. The authors investigated a homogeneous body model

15

with the use of the three-dimensional linear theory of elasticity. They analyzed the normal and shear stresses arising as a result of fiber curving. The impact of the interaction between the fibers on the distribution of these stresses was also studied.
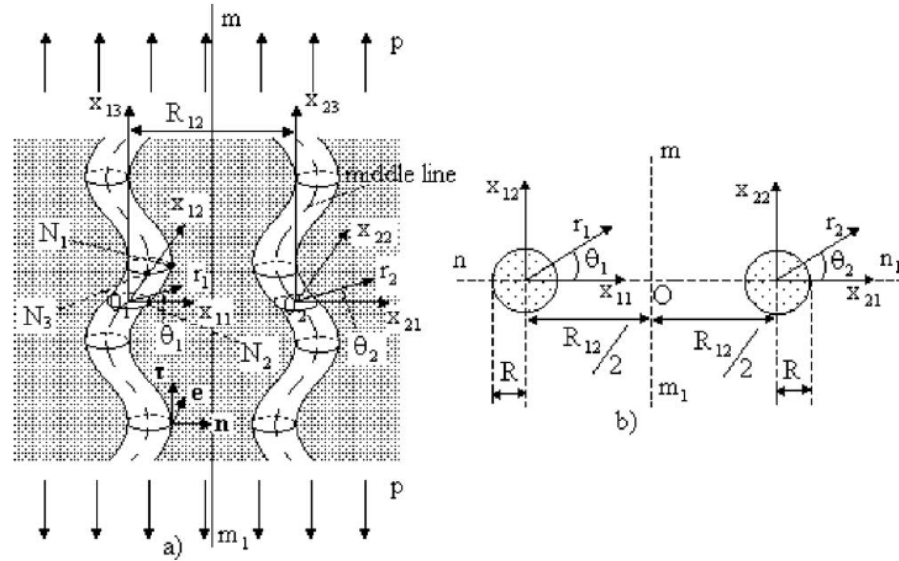
Figure 2-7. The geometry of the material structure and chosen coordinates (Akbarov and Koskar 2003)

Jiang *et al*. (2004) developed an analytical model for three-dimensional elastic stress field distribution in short fiber composites subjected to an applied axial load and thermal residual stresses. Two sets of the matrix displacement solutions, the far-field solution and the transient solution, were derived based on the theory of elasticity. These two sets were superposed to obtain simplified analytical expressions for a matrix three-dimensional stress field and a fiber axial stress field in the entire composite system including the fiber end regions with the use of the technique of adding imaginary fiber. The components of matrix three-dimensional stress field satisfied the equilibrium and compatibility

conditions in the theory of elasticity. The components of the fiber axial stress field satisfied the equilibrium requirements within the fiber and the fiber/matrix interface. The stress field components also satisfied the overall boundary conditions including the surface conditions, the interface continuity conditions and the axial force equilibrium conditions. The analytical model validity was examined with finite element numerical calculations.

Rossoll *et al*. (2005) presented analysis of longitudinal deformation of continuous fiber reinforced metals considering elastic and elastic-plastic matrix behavior. Analytical results were compared with finite element analyses (FEA) for varying fiber distributions, ranging from single fiber unit cells to complex cells.

2.2.2 Macro-mechanics models

Stress mapping and mechanical properties of woven-fabric composites depend on the reinforcing yarn geometry. It is important to generate a geometric concept describing the architecture. The idea is to discretize the composites into unit cells that include enough details of the geometry to predict the most important features of the composite behavior. The unit cell, in general, is defined as the smallest repeating pattern in the structure. In this section, macro-mechanics approaches based on unit-cell models will be reviewed. The unit-cell analysis used two analytical methods - closed form method and numerical method.

2.2.2.1 Closed form solutions

Ishikawa and Chou (1982) developed three basic analytical models to predict the in-plane thermo-elastic behavior of various woven-fabric composites. All models are one-dimensional (1D) models because they only consider the undulation of the yarns in the loading direction. First, the mosaic model considered the composite as an assembly of asymmetric cross-ply lamina. An upper bound for the stiffness is predicted by connecting the cross-ply lamina in parallel and a lower bound is predicted by connecting all pieces in series. In this model the yarn actual waviness was neglected. Second, the crimp model as an extension of the first model, considered the continuity and undulation of the yarns in the loading direction. However, the undulation of the yarns running perpendicular to the loading direction is neglected. Finally, the bridging model for satin composites was developed to simulate the load transfer amongst interlaced regions. Since the classic laminated plate theory is the basis of each of these models, only the in-plane properties are predicted. These models did not consider the actual yarn cross-sectional shape, the presence of a gap between adjacent yarns and the influence of crimp on fabric thickness. Therefore, no predictions are made for the fiber volume fraction or the fabric cover factor.

Ko and Chou (1989) developed three-dimensional fabric geometry model to study the compressive behavior of braided metal-matrix composites. The model is based on two important assumptions. First, each yarn system in the composite unit cell is treated as a unidirectional lamina. Second, the stiffness matrix of the composite unit cell can be

calculated as the weighted sum of the stiffness matrices of the different yarn systems by connecting all yarn systems in parallel and assuming an iso-strain condition in all yarn systems. This model gave a good prediction of the tensile behavior for braided composites.

Gowayed and Pastore (1992) reviewed different analytical methods for textile structural composites and used some experimental works to compare and evaluate these analytical methods. The introduced methods were divided into two main categories; an elastic techniques and a Finite Element Methods (FEM). The elastic technique included all stiffness average methods, modified matrix method and fiber inclination method. On the other hand, the FEM included the Finite Cell Model (FCM) and the discrete and continuum techniques. The results showed that stiffness predictions using the elastic techniques, except for the Modified Matrix Method, agreed well with the experiments. Although these techniques are easy to be implemented and tactless to geometric description, they need a failure criterion. In contrast, the Finite Element Methods were able to relate the external forces to the internal displacements but they are very sensitive to the geometric descriptions and hard to be implemented.

Naik and Shembekar (1992) developed a two-dimensional model (2D) which considered the undulation of yarns in warp and weft directions. In this model the unit cell is divided into different blocks such as straight cross-ply, undulated cross-ply, and pure matrix blocks. Two schemes are used to combine the different blocks: the parallel-series and the series-parallel models. In the parallel-series model, the blocks are assembled in parallel

19

across the loading direction utilizing an iso-strain assumption. Then, these multi-blocks are assembled in series along the loading direction utilizing an iso-stress assumption. On the basis of experimental work, the parallel-series model is recommended for the prediction of in-plane elastic constants.

Pastore *et al*. (1993) used Bezier patches to model the geometry of textile composites and discussed particular requirements to model textile composites. They also presented techniques to quantify the material inhomogeneities through 3D geometric modeling and methods to transform them into elastic properties. They chose the spline functions because of their natural flexibility to characterize the displacement functions.

Pastore and Gowayed (1994) modified the fabric geometry model (FGM) to predict the elastic properties of textile reinforced composites. They discussed and presented solution for two of the major drawbacks of the FGM. These problems are the incompatibility of the basic transverse isotropy assumption with the theoretical mathematical derivation and the inconsistency of the transformation matrices associated with the stiffness calculations. The basic idea behind the FGM is to treat the fibers and matrix as a set of composite rods having various spatial orientations. The local stiffness tensor for each of these rods is calculated and rotated in space to fit the global composite axes. The global stiffness tensors of all the composite rods are then superimposed with respect to their relative fiber volume fraction to form the composite stiffness tensor. This technique is called a stiffness averaging method.

Hahn and Pandy (1994) developed a three-dimensional (3D) model for plain-fabric composites. This model is simple in concept and mathematical implementation. The yarn undulations are considered sinusoidal and described with shape functions. In the elastic analysis a uniform strain throughout the plain-weave composite unit cell is assumed.

Naik and Ganesh (1995) developed closed-form expressions for in-plane thermo-elastic properties of plain-weave fabric lamina. Shape functions were used to define the yarn cross-section and undulation. The predicted constants corresponded well to the results obtained with the parallel-series model.

Vaidyanathan and Gowayed (1996) presented logical methodology to predict the optimum fabric structure and fiber volume fraction to meet a set of target elastic properties for textile composite. The stiffness averaging technique was used in the design steps to predict the composite elastic properties. After identifying the solution for the optimization problem, two commercial software packages, DOT and GINO, were used to solve different case studies. The quality of results from the two software packages was evaluated.

Gowayed *et al*. (1996) presented a modified technique to solve the problem of unit cell continuum model, presented by Foye (1992), based on finite element analysis using heterogeneous hexahedra brick elements to predict the elastic properties of textile composites. Due to the large differences in the fiber and matrix stiffness, the use of these elements initiated mathematical instabilities in the solution which affected the accuracy

21

of the results. The solution was based on a micro-level homogenization approach using a self-consistent fiber geometry model. In addition, the geometrical model was integrated with the modified mechanical analysis to guarantee accurate representation of complex fabric preforms. The prediction results of the modified technique matched well with experimental results for in-plane property tests for five-harness satin weave carbon/epoxy composite and three-dimensional weave E-glass/poly (vinyl ester) composite.

Vandeurzen *et al*. (1996) presented three-dimensional geometric and elastic modeling of a large range of two-dimensional woven fabric lamina. The model predicted the shear moduli for the fabric composite, the fiber volume fraction, the orientation of the yarn and the fractional volume of each micro-cell. In addition, the geometric model was able to evaluate some textile properties as cover factor and fabric thickness

Barbero *et al*. (2005) developed an analytical model to predict a complete set of orthotropic effective material properties for woven fabric composites based only on the properties of the constituent materials. They used the existing periodic microstructure theory applied at the meso-level to model the undulating fiber/matrix tows as periodic inclusions, and predicted the overall material properties of a plain weave fabric reinforced composite material. The representative volume element (RVE) was discretized into fiber/matrix bundles, figure 2-8. The surfaces of the fiber/matrix bundles are fit with sinusoidal equations based on measurements taken from photomicrographs of composite specimens and an idealized representation of the plain weave structure was created. The

model results showed good agreement with compared experimental data from literatures, including interlaminar material properties.
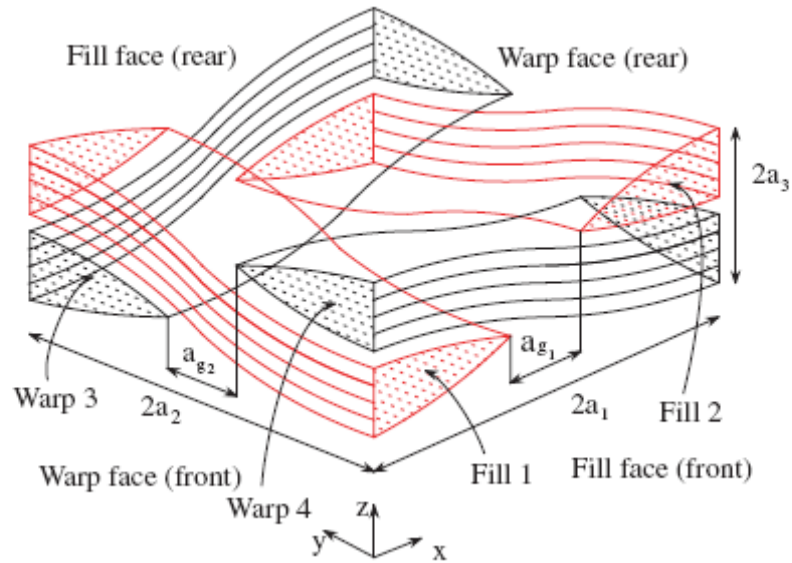
Figure 2-8. Meso-scale analysis of a plain weave fabric RVE (1/2 period shown in-plane (x-y)), (Barbero *et al*. 2005)

2.2.2.1.1 Advantage of closed form solutions:

- Require simple input of geometric parameters and material properties.

- The overall constitutive descriptions are developed from composite structure in terms of the volume fraction and the interface conditions of the constituents.

2.2.2.1.2 Disadvantage of closed form solutions:

- Mainly restricted to the stiffness and strength prediction at the lamina level or unidirectional composites.

- Focused on simple and/or idealized systems for fiber description.

- Do not consider the effect of the neighboring fibers.

- Are not able to provide quantitative predictions of composite failure mainly because interlaminar stresses have been neglected.

2.2.2.2 Numerical models

Numerical models in general use a finite element (FE) frame work to perform the constitutive stress/strain relations using stress or energy equations. Finite element models can be used to analyze the elastic behavior and the internal stress/strain state of woven-fabric composites. Due to the complexity of yarn architecture, finite element modeling is most helpful and accurate to model each material group, fiber/matrix, discretely.

Jara-Almonte and Knight (1988) developed a specified boundary stiffness/force (SBSF) method for finite element sub-region analysis. The boundary forces calculated from the global analysis at the global/local boundary were specified on the local model. The mesh refinement for the local model was done such that the number of nodes on the global/local boundary for the refined local model was the same as the number of nodes for the global model.

Guedes and Kikuchi (1990) studied the applicability of the homogenization theory for stress analysis of various linear elastic composite materials with periodic microstructures including woven fiber reinforced composites. They presented the effectiveness of using adaptive mesh refinement over uniform mesh refinement to predict the homogenized material constants.

Luo and Sun (1991) proposed three global/local methods to determine the ply level stresses in thick fiber-wound composite cylinders assuming that the change in temperature was uniform and axial force, torque and normal tractions on inner and outer surfaces of the cylinder were constant. In the first method they used the continuity conditions of the macroscopic strains and stresses in a section of the cylinder to determine the ply level strains and stresses. In the second method they used the macroscopic axial strain, torsional strain and radial stress along with continuity conditions to solve an assumed displacement field for each ply. In the third method, an extension of the second method, they used the imbalance in axial force and torque as input to perform another round of global/local analysis.

Woo and Whitcomb (1993) used single field macro elements to determine the global/local response of a plain weave composite subjected to a uniaxial stress in the warp direction. Displacements from a global model were imposed along the entire global/local boundary. This procedure predicted stress distribution away from the global/local boundary but with large errors near the boundary.

Whitcomb and Woo (1994) developed multi-field macro elements based on an efficient zooming technique wherein suitably refined local mesh was included in the global model without adding any additional degrees of freedom. Hirai used static condensation to reduce the internal degree of freedom of the refined local mesh to the boundary degrees of freedom (Hirai *et al*. 1984). Whicomb *et al.* used multi-point constraints to reduce the boundary degrees of freedom to that of the macro element used for the global analysis. They used global/local method to predict the stress distribution in a unit cell subjected to uniaxial stress in the warp direction. The prediction using multi-field macro elements were shown to be more accurate than that using the single-field macro elements but still large errors were predicted near the global/local boundary.

Whitcomb *et al*. (1995) describe two global/local procedures which used homogenized engineering material properties to accelerate global stress analysis of textile composites and to determine the errors which are inherent in such analyses. The response of a local region was approximated by several fundamental strain or stress modes. The magnitudes of these modes were determined from the global solutions and used to scale and superpose solutions from refined analyses of the fundamental modes.

2.2.2.2.1   Advantage of the numerical models

- They are helpful and accurate to model each material group, fiber/matrix, discretely and can have extremely complicated geometric details of composite constituents.

26

- They are able to deal with the changing of geometric characteristics of the layers, such as thickness and relative layer shifts.

2.2.2.2.2 Disadvantage of the numerical models

- The constitutive relations are independent of the scale of the micro-structure.

- FE approach requires large computer memory and calculation power. Therefore, most of the analyses were only performed for simple fabrics, like balanced plain-woven fabrics.

- Most of the time spent is related to the creation and verification of a correct fabric geometry.

- There are major problems in analyzing and interpreting the results in a 3D domain of a rather complex geometry.

2.3 Review of delamination

Delamination is considered to be the most common life limiting growth mode in composite structures, other than 3D textile composites. Thus it is a fundamental issue in the evaluation of laminated composite structures for durability and damage tolerance.

Blackketter *et al*. (1993) presented a progressive failure analysis of a plain weave composites. The composite response was almost linear for in-plane extension and highly nonlinear for in-plane shear. The nonlinearity was mainly a result of progressive damage.

However, little information was provided on damage evolution and load redistribution within the composite during the loading process. They did not examine the sensitivity of the predictions to mesh refinement or any other approximations inherent in the analyses.

Wisnom and Jones (1995) proposed a method to predict delamination using a failure envelope constructed between the measured interlaminar shear strength and the predicted bending strain for delamination under pure bending which was calculated from a simple equation for the strain energy release rate, and the fracture energy of the material. Two flexural tests, three-point and four-point bending, were performed for glass/epoxy prepreg laminated composite. Samples loaded in three-point bending were found to fail by unstable delamination from the ends of the plies. However, the four-point samples failed in flexure before delamination propagation. The results showed that a linear interaction between the interlaminar shear stress and surface bending strain at the location of the cut was found to fit the data well.

Wisnom (1996) analyzed the short-beam shear test of carbon fiber/epoxy composite assuming that the deformation is concentrated at the resin layers between plies. He used a two-dimensional finite element model (FEM) with linear elastic continuum elements to represent the plies, and non-linear springs to model the interfaces assuming there is sufficiently large number of plies or there is a stress concentration causing the maximum stress to occur at certain interface. The analysis of the linear elastic strain energy release rate showed that there is not sufficient energy for the small cracks to propagate, however, the approach predicted that small cracks can have important effect on interlaminar shear

strength. He concluded that linear elastic fracture mechanics is not suitable for analyzing short-beam shear specimens.

Whitcomb and Srirengan (1996) used three-dimensional (3D) finite element analysis to simulate progressive failure of a plain weave composite subjected to in-plane extension. They examined the effects of different characteristics of the finite element model on the predicted behavior. It was found that predicted behavior is sensitive to mesh refinement and the material degradation model. The results showed that the predicted strength decreased significantly with increasing the waviness.

Srirengan *et al*. (1997) developed a global/local method based on modal analysis to facilitate the three-dimensional stress analysis of plain weave composite structures, figure 2-9. The global response of studied region was decomposed into a few fundamental macroscopic modes which were either strain modes, calculated from the boundary displacements, or stress modes, calculated from the boundary forces. Failure initiation was found to match reasonably well with the conventional finite element prediction obtained using a detailed mesh for the entire plate. This method is considered computationally far less intensive and reasonably accurate when compared to the traditional finite element method.

Hutapea *et al*. (2003) developed a theory to provide a connection between macro-mechanics and micro-mechanics models in characterizing the micro-stress of composite laminates in regions of high macroscopic stress gradients. They present the micro-polar

homogenization method to determine the micro-polar anisotropic effective elastic moduli and investigated the effects of fiber volume fraction and cell size on the normal stress along the artificial interface resulting from ply homogenization of the composite laminate. They focused on the stress fields near the free edge where high macro-stresses gradient occur.
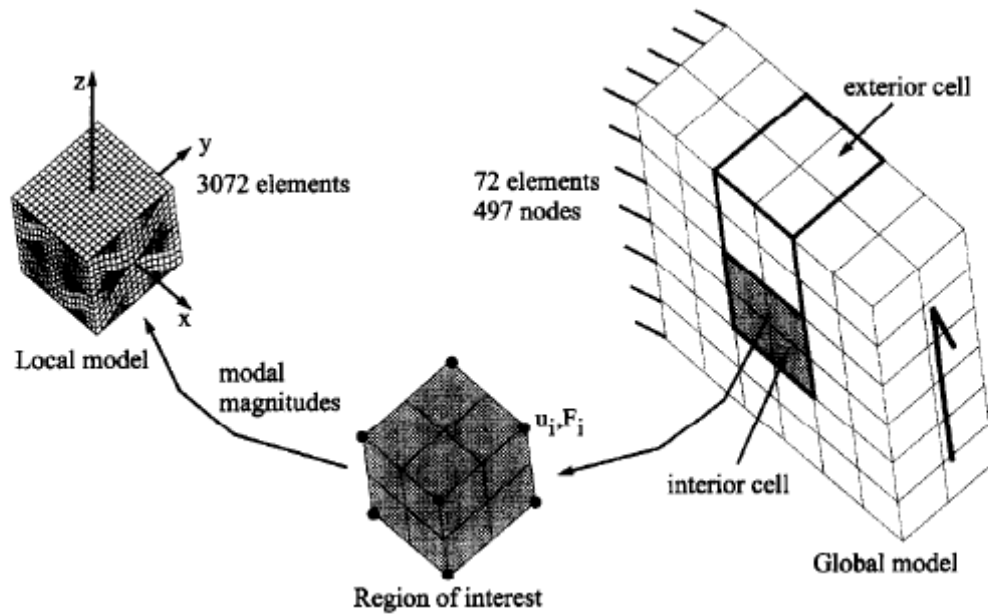
Figure 2-9. Schematic of the modal technique for global/local stress analysis, (Srirengan *et al*. 1997)

Bahei-El-Din *et al*. (2004) presented a micro-mechanical model derived from actual microstructures for 3D-woven composites showing progressive damage. Local damage mechanisms that are typically found in woven systems under quasi-static and dynamic loads were modeled using a transformation field analysis (TFA) of a representative volume element (RVE) of the woven architecture. The damage mechanisms were typical

to those observed in quasi-static and impact tests of woven composite samples, and include matrix cracking, frictional sliding and debonding of the fiber bundles and fiber rupture. This model offered a consistent approach to estimate the effects of the material heterogeneity and damage on wave distribution and reduction in shockwave problems. The solution is acquired as the sum of the elastic, undamaged response and the contribution of an auxiliary transformation stress field for a selected subdivision of the RVE. The predicted overall response showed the progressive decay of the stiffness.

Le Page *et al*. (2004) developed a representative two-dimensional finite element model to analyze matrix cracking in woven fabric composites. The finite element model has enabled the effects of relative layer shift and laminate thickness to be examined in the framework of the stiffness and matrix cracking behavior of plain weave fabric laminate. It was found that the effects of layer shift and laminate thickness are minor; however there are much large differences in the energy release rates interrelated with matrix crack formation. Using a two-dimensional model made the effects of micro-structural variation in the through-width direction to be neglected.

2.4 Problem Statement

In the previous sections, micro-mechanics and macro-mechanics models that dealt with stress mapping in composite material were reviewed. It can be seen from this review that macro/structural models based on unit-cell analysis, using closed form solutions or numerical models, were not able to provide detailed stress distribution at the constituent

31

level. On the other hand, micro-mechanics models lacked the macro-geometric resolution necessary to predict important phenomena such as failure.

Possible merging macro-structure models with micro-structure models will allow stress mapping that is sensitive to composite geometry and structure. In this work a closed form micro solution is presented to map stress/strain at the fiber and matrix levels. A macro-mechanics model based on unit-cell analysis (e.g. pcGINA) developed by Gowayed (1996) will be used to evaluate stresses/strains at the macro-level then the newly developed micro-stress model will use these stresses/strains as input. By doing this, a more realistic stress distribution within the composite constituents will be accomplished.

III. ANALYTICAL MODELS

3.1 Introduction

In this chapter a micromechanics model is created to evaluate the 3D stress and strain distribution in for an n-phase material (e.g., fiber, matrix and at fiber matrix interface). The model is built at the micro-level with global stress and strain data obtained through structural analysis and a unit-cell model as described in the previous chapter. The proposed model is divided into two parts - a 3D longitudinal model and a 2D transverse model. Both models are verified singly using Finite Element Analysis and jointly via comparison to other research work.

3.2 The 3D longitudinal model

A cylinder model has been used to represent a fiber surrounded by two hollow cylinders, which represent the surrounding interface and matrix as an example for an n-phase material. A constant stress is applied to the whole composite in the z-direction (Figure 3-1). Axisymmetric stress analysis is performed to predict the stress distribution in this model.
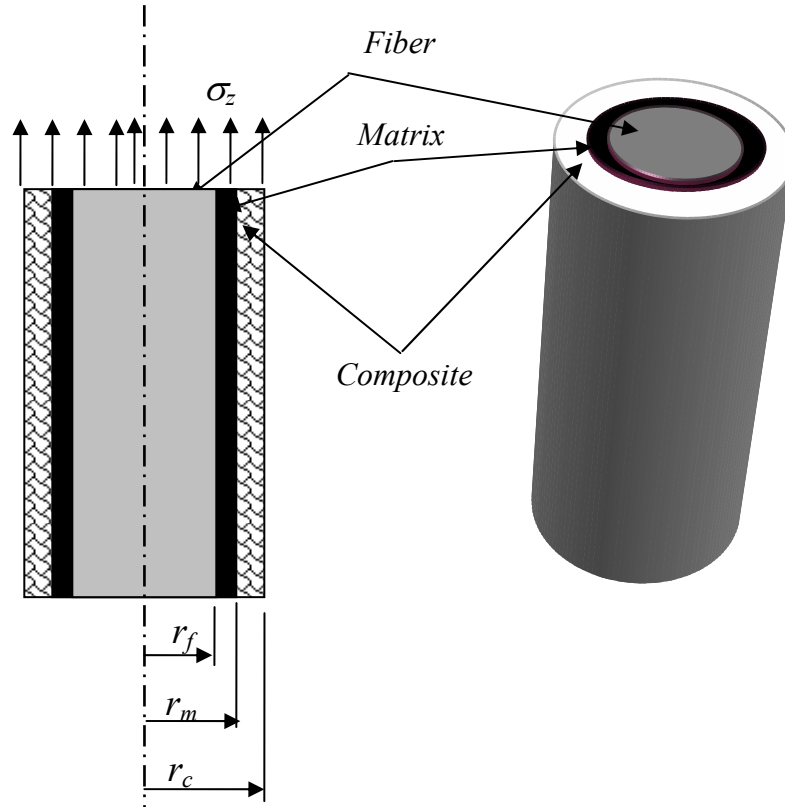
Figure 3-1: 3D model with axial stress

The force equilibrium in the radial direction in each cylinder is:

$$\frac{\partial \sigma_r}{\partial r} + \frac{\sigma_r - \sigma_\theta}{r} + \frac{\partial \tau_{rz}}{\partial z} = 0 \qquad (3\text{-}1)$$

Where, r and θ are the radial and circumferential directions, respectively.

σ_r, σ_θ and τ_{rz} are radial, hoop and shear stresses, respectively.

$$\sigma_\theta = \sigma_r + r\frac{\partial \sigma_r}{\partial r} + r\frac{\partial \tau_{rz}}{\partial z} \qquad (3\text{-}2)$$

If u_r is the radial displacement, the circumferential and radial strains can be represented as:

$$\varepsilon_\theta = \frac{u_r}{r}, \qquad or \qquad u_r = \varepsilon_\theta \cdot r$$

$$\varepsilon_r = \frac{\partial u_r}{\partial r} = r\frac{\partial \varepsilon_\theta}{\partial r} + \varepsilon_\theta \tag{3-3}$$

$$\varepsilon_\theta = \frac{1}{E_\theta}\left(\sigma_\theta - \upsilon_{r\theta}\sigma_r\right) - \frac{\upsilon_{z\theta}}{E_z}\sigma_z \tag{3-4}$$

By inserting equation (3-2) in equation (3-4):

$$\varepsilon_\theta = \frac{1}{E_\theta}\left(\sigma_r + r\frac{\partial \sigma_r}{\partial r} + r\frac{\partial \tau_{rz}}{\partial z} - \upsilon_{r\theta}\sigma_r\right) - \frac{\upsilon_{z\theta}}{E_z}\sigma_z \tag{3-5}$$

Differentiate ε_θ by r,

$$\frac{\partial \varepsilon_\theta}{\partial r} = \frac{1}{E_\theta}\left(\frac{\partial \sigma_r}{\partial r} + r\frac{\partial^2 \sigma_r}{\partial r^2} + \frac{\partial \sigma_r}{\partial r} + r\frac{\partial^2 \tau_{rz}}{\partial z\partial r} + \frac{\partial \tau_{rz}}{\partial z} - \upsilon_{r\theta}\frac{\partial \sigma_r}{\partial r}\right) \tag{3-6}$$

The axial stress σ_z is constant within each region, which means that $\dfrac{\partial \sigma_z}{\partial r} = 0$

By inserting equation (3-5) and equation (3-6) in equation (3-3):

$$\varepsilon_r = \frac{r}{E_\theta}\left(r\frac{\partial^2 \sigma_r}{\partial r^2} + r\frac{\partial^2 \tau_{rz}}{\partial z\partial r} + \frac{\partial \sigma_r}{\partial r} + \frac{\partial \tau_{rz}}{\partial z} + (2 - \upsilon_{r\theta})\frac{\partial \sigma_r}{\partial r}\right)$$

$$\tag{3-7}$$

$$+ \frac{1}{E_\theta}\left(r\frac{\partial \sigma_r}{\partial r} + r\frac{\partial \tau_{rz}}{\partial z} + (1 - \upsilon_{r\theta})\sigma_r\right) - \frac{\upsilon_{z\theta}}{E_z}\sigma_z$$

But the radial strain has another form.

35

$$\varepsilon_r = \frac{1}{E_r}\left(\sigma_r - \upsilon_{\theta r}\sigma_\theta\right) - \frac{\upsilon_{zr}}{E_z}\sigma_z \qquad (3\text{-}8)$$

Again inserting equation (3-2) in equation (3-7) to get:

$$\varepsilon_r = \frac{1}{E_r}\left(\left(1-\upsilon_{\theta r}\right)\sigma_r - \upsilon_{\theta r}\cdot r\frac{\partial\sigma_r}{\partial r} - \upsilon_{\theta r}\cdot r\frac{\partial\tau_{rz}}{\partial z}\right) - \frac{\upsilon_{zr}}{E_z}\sigma_z \qquad (3\text{-}9)$$

Now, equation (3-7) = equation (3-9) and also $E_r = E_\theta$

$$r^2\frac{\partial^2\sigma_r}{\partial r^2} + r^2\frac{\partial^2\tau_{rz}}{\partial z\partial r} + r\frac{\partial\tau_{rz}}{\partial z} + r\cdot\left(2-\upsilon_{r\theta}\right)\frac{\partial\sigma_r}{\partial r}$$

$$+ r\frac{\partial\sigma_r}{\partial r} + r\frac{\partial\tau_{rz}}{\partial z} + r\cdot\upsilon_{\theta r}\frac{\partial\sigma_r}{\partial r} + r\cdot\upsilon_{\theta r}\frac{\partial\tau_{rz}}{\partial z} = 0$$

$$r^2\frac{\partial^2\sigma_r}{\partial r^2} + \left[r\left(2-\upsilon_{r\theta}\right) + r + r\cdot\upsilon_{r\theta}\right]\frac{\partial\sigma_r}{\partial r} + r^2\frac{\partial^2\tau_{rz}}{\partial z\partial r} + \left(2r + r\cdot\upsilon_{r\theta}\right)\frac{\partial\tau_{rz}}{\partial z} = 0$$

$$r^2\frac{\partial^2\sigma_r}{\partial r^2} + 3r\frac{\partial\sigma_r}{\partial r} + r^2\frac{\partial^2\tau_{rz}}{\partial z\partial r} + r\left(2+\upsilon_{r\theta}\right)\frac{\partial\tau_{rz}}{\partial z} = 0 \qquad (3\text{-}10)$$

From the force equilibrium on the fiber (figure 3-2)
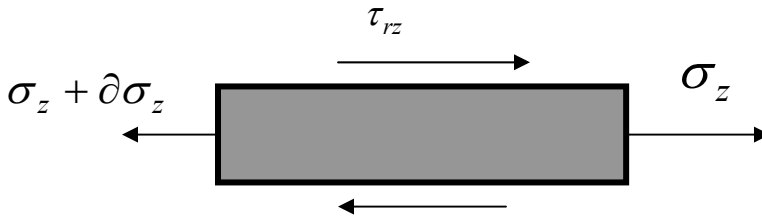
Figure 3-2: Forces on a fiber element in the longitudinal direction

36

$$\sigma_z \cdot \pi \cdot r^2 - (\sigma_z + \partial \sigma_z) \cdot \pi \cdot r^2 = \tau_{rz} \cdot 2 \cdot \pi \cdot r \cdot \partial z$$

$$\frac{\partial \sigma_z}{\partial z} = \frac{2 \cdot \tau_{rz}}{r}$$

Differentiation by r will get:

$$\frac{\partial^2 \sigma_z}{\partial z \partial r} = \frac{-2 \cdot \tau_{rz}}{r^2} + \frac{2}{r} \frac{\partial \tau_{rz}}{\partial r}, \text{ and it was assumed that } \frac{\partial \sigma_z}{\partial r} = 0$$

So, $\dfrac{\partial \tau_{rz}}{\partial r} = \dfrac{\tau_{rz}}{r}$

Assuming that $\dfrac{\partial \tau_{rz}}{\partial z} = 0$, then equation (3-10) will be:

$$r^2 \frac{\partial^2 \sigma_r}{\partial r^2} + 3r \frac{\partial \sigma_r}{\partial r} = 0 \tag{3-11}$$

The solution for this second order differential equation is:

$$\sigma_r = M + \frac{N}{r^2} \tag{3-12-a}$$

$$\sigma_\theta = M - \frac{N}{r^2} \tag{3-12-b}$$

Where: M, N are integration constants that can be determined from the boundary conditions.

The cylinders representing the fiber, the surrounding matrix and the composite can be analyzed as follows:

a) Fiber:

The radial stress (σ_r) must remain finite at r = 0 which means that N should equal zero.

$$\sigma_{rf} = K_f$$

$$\sigma_{\theta f} = K_f$$

b) Matrix

$$\sigma_{rm} = M_m + \frac{N_m}{r^2}$$

$$\sigma_{\theta m} = M_m - \frac{N_m}{r^2}$$

c) Composite

$$\sigma_{rc} = M_c + \frac{N_c}{r^2}$$

$$\sigma_{\theta c} = M_c - \frac{N_c}{r^2}$$

This reduced the number of constants to five in addition to the three axial stresses (σ_{zf}, σ_{zm} and σ_{zc}) and the following boundary conditions can be used to obtain the values of these constants.

Boundary Conditions:

At r = r_f (r_f is the radius of the fiber)

i) $\quad \sigma_{rf}(r_f) = \sigma_{rm}(r_f)$

ii) $\quad u_{rf}(r_f) = u_{rm}(r_f)$

iii) $\quad \varepsilon_{zf}(r_f) = \varepsilon_{zm}(r_f)$

38

At r = r_m (r_m is the outer radius of the matrix)

$$iv) \qquad \sigma_{rm}(r_m) = \sigma_{re}(r_m)$$

$$v) \qquad u_{rm}(r_m) = u_{rc}(r_m)$$

$$vi) \qquad \varepsilon_{zm}(r_f) = \varepsilon_{ze}(r_f)$$

At r = r_c (r_c is the outer radius of the composite)

$$vii) \qquad \sigma_{rc}(r_c) = known$$

The force balance in the axial direction gives

$$viii) \qquad \sum F_z = \sigma_z \cdot r_c^2$$

$$\sigma_{zf} \cdot r_f^2 + \sigma_{zm} \cdot \left(r_m^2 - r_f^2\right) + \sigma_{zc} \cdot \left(r_c^2 - r_m^2\right) = \sigma_z \cdot r_c^2$$

3.2.1 Model verification

After determining the stress constants, the radial stress, the radial displacements and circumferential stress can be determined at any radius. To verify the model, a 3D finite element model (FEM) was built using the data shown in Table 3-1. All materials are considered isotropic. The radial stresses outside the hollow cylinders were assumed to be zero in this analysis; nevertheless, other values can be used.

A Matlab® code using symbolic math was developed for the 3D longitudinal model and is listed in Appendix A. The radial displacement, the radial stress and the hoop stress are calculated by the model in each region and extracted from the finite element model. The

results showed perfect agreement between the model and the FEM as shown in the figure 3-3 for the radial displacement, figure 3-4 for the radial stress and figure 3-5 for the circumstantial or hoop stress.

Table 3-1: Fiber, interface and matrix properties used to verify the model

	Fiber	Interface	Matrix
Radius (μm)	6	6.5	9.5
Modulus of Elasticity (E) (GPa)	370	15	330
Poisson ratio	0.17	0.2	0.12
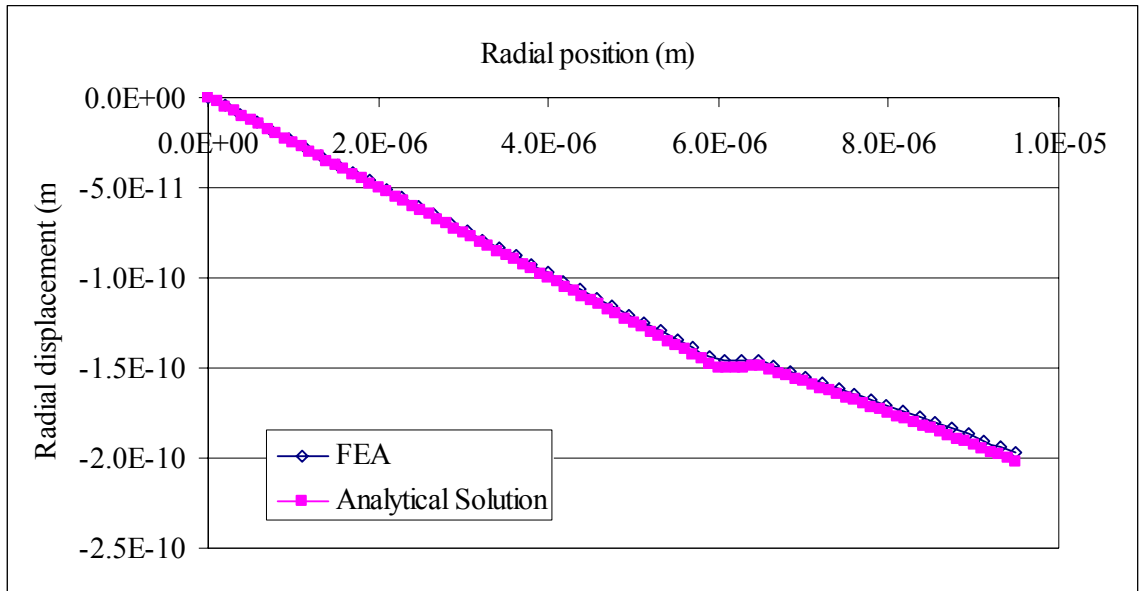
Figure 3-3: Radial displacement
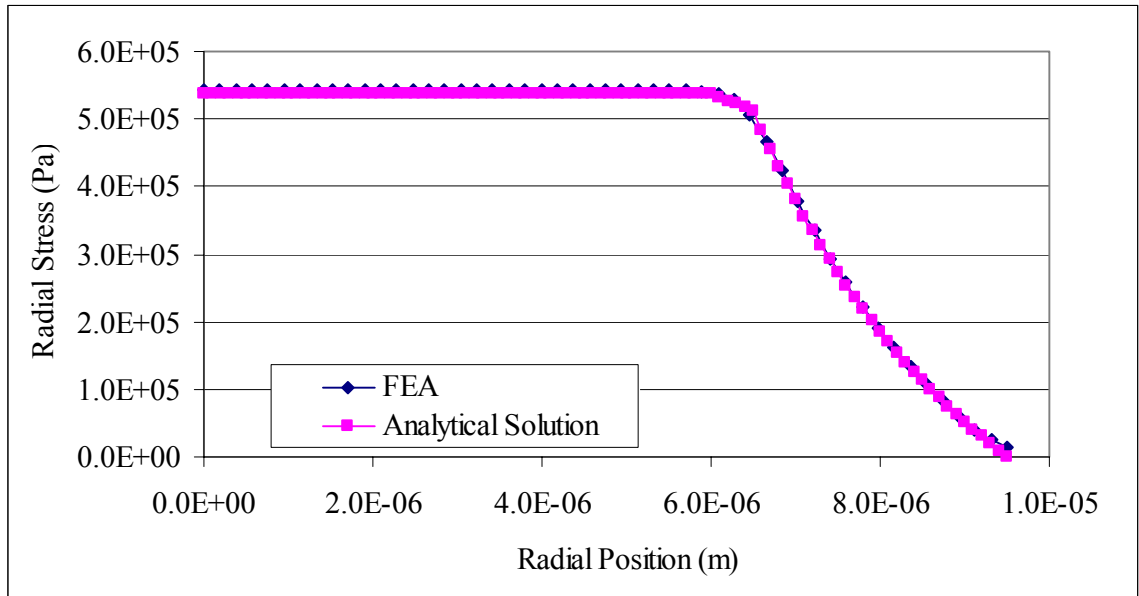
Figure 3-4: Radial stress
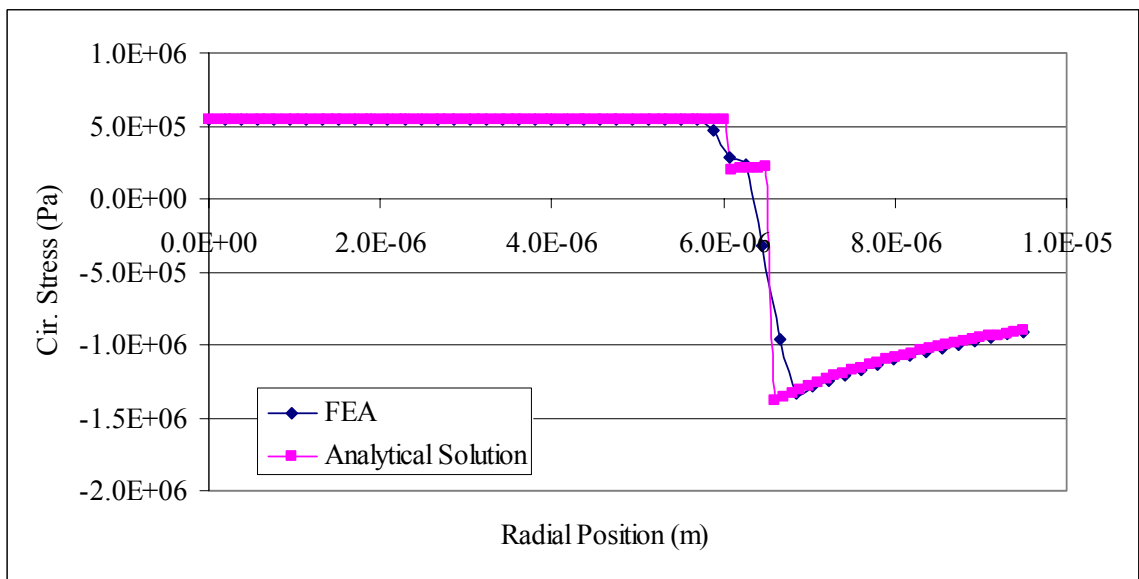
Figure 3-5: Circumstantial or hoop stress

3.3 The 2D transverse model
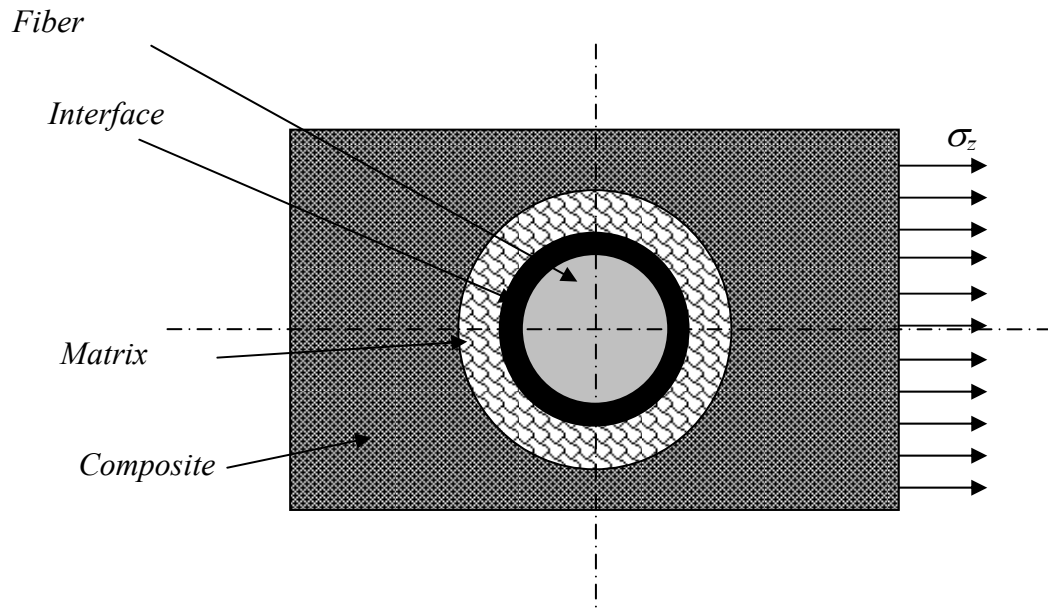
Figure 3-6: 2D model with transverse stress

In this model, a general solution to a bi-harmonic equation "Kolosov Mukhelishvili complex potential" was adopted to obtain a set of equations to represent the stresses and displacements for each region for an n-phase material (e.g., fiber/interface/matrix). The original set of equations was originally derived by Savin (1961) for concentric rings surrounding a hole in an infinitely large plate. The equations were modified to introduce a material (e.g., fiber) in the place of the hole. In this section the derived equations and the equations for the fiber are presented. The detailed derivation and the equations modification is presented in Appendix C.

a) Fiber's equations

$$\sigma_r = \frac{P}{2}\left[A_f + \left(\frac{B_f}{2}\right)\cdot\cos(2\cdot\theta)\right]$$

$$\sigma_\theta = \frac{P}{2}\left[A_f - \left(\frac{B_f}{2} - 6\cdot C_f\,\frac{r^2}{R^2}\right)\cdot\cos(2\cdot\theta)\right]$$

$$\tau_{r\theta} = \frac{P}{2}\left[3\cdot C_f\,\frac{r^2}{R^2} - \frac{B_f}{2}\right]\cdot\sin(2\cdot\theta)$$

$$u_r = \frac{P\cdot R}{8\mu}\left\{\left[A_f(\eta-1)\frac{r}{R}\right] + \left[C_f(\eta-3)\frac{r^3}{R^3} + B_f\,\frac{r}{R}\right]\cdot\cos(2\cdot\theta)\right\}$$

$$u_\theta = \frac{P\cdot R}{8\mu}\left[C_f(\eta+3)\frac{r^3}{R^3} - B_f\,\frac{r}{R}\right]\cdot\sin(2\cdot\theta)$$

b) Interface's equations

$$\sigma_r = \frac{P}{2}\left[\left(A_c - \frac{1}{2}B_c\cdot\frac{R^2}{r^2}\right) + \left(\frac{C_c}{2} - 2D_c\cdot\frac{R^2}{r^2} - \frac{3}{2}E_c\cdot\frac{R^4}{r^4}\right)\cdot\cos(2\cdot\theta)\right]$$

$$\sigma_\theta = \frac{P}{2}\left[\left(A_c + \frac{1}{2}B_c\cdot\frac{R^2}{r^2}\right) - \left(\frac{C_c}{2} - 6\cdot F_c\,\frac{r^2}{R^2} - \frac{3}{2}E_c\cdot\frac{R^4}{r^4}\right)\cdot\cos(2\cdot\theta)\right]$$

$$\tau_{r\theta} = \frac{P}{2}\left[3\cdot F_c\,\frac{r^2}{R^2} - \frac{C_c}{2} - D_c\cdot\frac{R^2}{r^2} - \frac{3}{2}E_c\cdot\frac{R^4}{r^4}\right]\cdot\sin(2\cdot\theta)$$

$$u_r = \frac{P\cdot R}{8\mu}\left\{\left[A_c(\eta-1)\frac{r}{R} + B_c\cdot\frac{R}{r}\right] + \left[F_c(\eta-3)\frac{r^3}{R^3} + C_c\,\frac{r}{R} + D_c\cdot(\eta+1)\frac{R}{r} + E_c\cdot\frac{R^3}{r^3}\right]\cdot\cos(2\cdot\theta)\right\}$$

$$u_\theta = \frac{P\cdot R}{8\mu}\left[F_c(\eta+3)\frac{r^3}{R^3} - C_c\,\frac{r}{R} - D_c\cdot(\eta-1)\frac{R}{r} + E_c\cdot\frac{R^3}{r^3}\right]\cdot\sin(2\cdot\theta)$$

c) Matrix's equations

$$\sigma_r = \frac{P}{2}\left[\left(A_m - \frac{1}{2}B_m \cdot \frac{R^2}{r^2}\right) + \left(\frac{C_m}{2} - 2D_m \cdot \frac{R^2}{r^2} - \frac{3}{2}E_m \cdot \frac{R^4}{r^4}\right)\cdot \cos(2\cdot\theta)\right]$$

$$\sigma_\theta = \frac{P}{2}\left[\left(A_m + \frac{1}{2}B_m \cdot \frac{R^2}{r^2}\right) - \left(\frac{C_m}{2} - 6\cdot F_m \frac{r^2}{R^2} - \frac{3}{2}E_m \cdot \frac{R^4}{r^4}\right)\cdot \cos(2\cdot\theta)\right]$$

$$\tau_{r\theta} = \frac{P}{2}\left[3\cdot F_m \frac{r^2}{R^2} - \frac{C_m}{2} - D_m \cdot \frac{R^2}{r^2} - \frac{3}{2}E_m \cdot \frac{R^4}{r^4}\right]\cdot \sin(2\cdot\theta)$$

$$u_r = \frac{P\cdot R}{8\mu}\left\{\left[A_m(\eta-1)\frac{r}{R} + B_m \cdot \frac{R}{r}\right] + \left[F_m(\eta-3)\frac{r^3}{R^3} + C_m \frac{r}{R} + D_m \cdot (\eta+1)\frac{R}{r} + E_m \cdot \frac{R^3}{r^3}\right]\cdot \cos(2\cdot\theta)\right\}$$

$$u_\theta = \frac{P\cdot R}{8\mu}\left[F_m(\eta+3)\frac{r^3}{R^3} - C_m \frac{r}{R} - D_m \cdot (\eta-1)\frac{R}{r} + E_m \cdot \frac{R^3}{r^3}\right]\cdot \sin(2\cdot\theta)$$

d) Composite's equations

$$\sigma_r = \frac{P}{2}\left[\left(1 - \frac{1}{2}A_e \cdot \frac{R^2}{r^2}\right) + \left(1 - 2B_e \cdot \frac{R^2}{r^2} - \frac{3}{2}C_e \cdot \frac{R^4}{r^4}\right)\cdot \cos(2\cdot\theta)\right]$$

$$\sigma_\theta = \frac{P}{2}\left[\left(1 + \frac{1}{2}A_e \cdot \frac{R^2}{r^2}\right) - \left(1 - \frac{3}{2}C_e \cdot \frac{R^4}{r^4}\right)\cdot \cos(2\cdot\theta)\right]$$

$$\tau_{r\theta} = -\frac{P}{2}\left[1 + B_e \cdot \frac{R^2}{r^2} + \frac{3}{2}C_e \cdot \frac{R^4}{r^4}\right]\cdot \sin(2\cdot\theta)$$

$$u_r = \frac{P\cdot R}{8\mu}\left\{\left[(\eta-1)\frac{r}{R} + A_e \cdot \frac{R}{r}\right] + \left[2\frac{r}{R} + B_e \cdot (\eta+1)\frac{R}{r} + C_e \cdot \frac{R^3}{r^3}\right]\cdot \cos(2\cdot\theta)\right\}$$

$$u_\theta = \frac{P\cdot R}{8\mu}\left[-2\frac{r}{R} - B_e \cdot (\eta-1)\frac{R}{r} + C_e \cdot \frac{R^3}{r^3}\right]\cdot \sin(2\cdot\theta)$$

Where:

> R is r_m

> P is the stress applied on the system

> μ is the shear modulus for each region

> $\eta = 3 - 4\nu$ for each region

> A, B, C …etc. are constants to be determined by applying the stress equilibrium and displacements compatibility on the interfaces.

3.3.1 Model verification

To verify the 2D transverse model, at an elementary level, the model's results are compared to the famous mechanics problem of estimating the stress concentration around circular cut-out in an infinite sheet subjected to tensile stress, figure 3-7. The results matches with the solution of this problem as shown in figure 3-8. At $\theta = 90$, the stress concentration is equal to 3. At $\theta = 0$ or 180, the stress concentration is equal to -1. The stress concentration around the cut-out is represented by a cosine curve, which is similar to the solution of this problem.
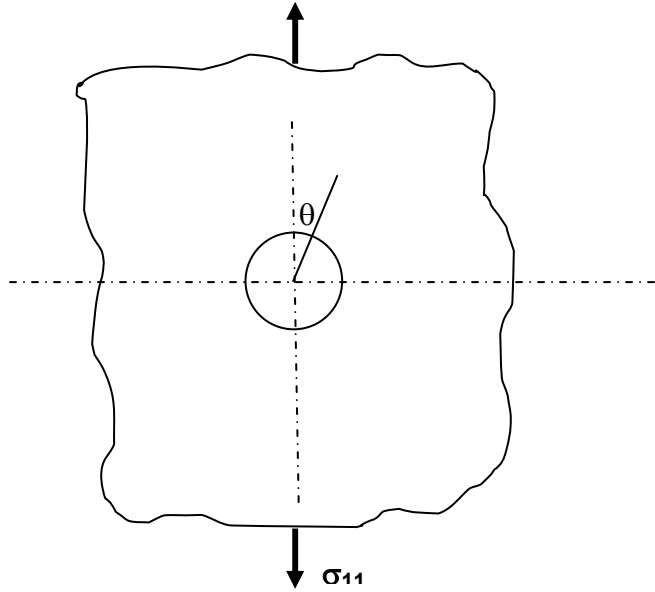
Figure 3-7: Circular cut-out in an infinite sheet subjected to tensile stress

In addition, using the material data of the fiber, interface and matrix in Table 3-1, a 2D finite element model (FEM) was built and its results is compared to the 2D transverse model as shown in figure 3-9. It can be seen that the radial displacement results of the FEM is very close to the 2D model's results. A Matlab® code using symbolic math was developed for the 2D transverse model and is listed in Appendix B.

46
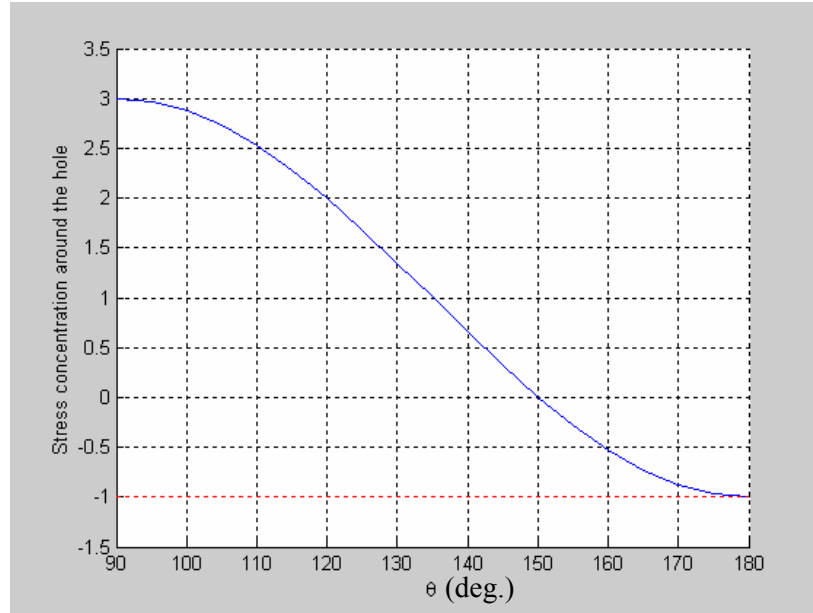
Figure 3-8: Stress concentration around a circular cut-out in an infinite sheet subjected to

tensile stress
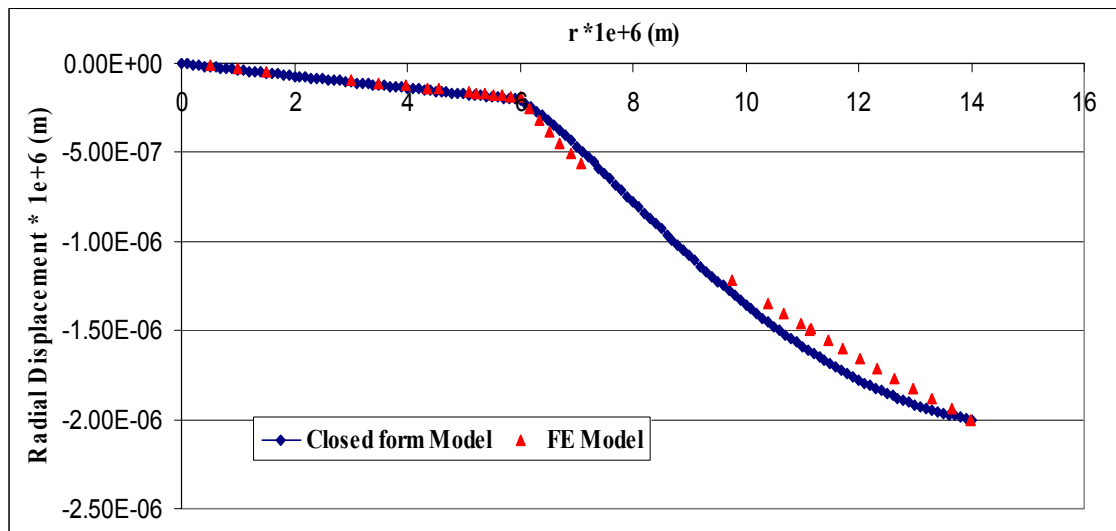
Figure 3-9: Radial displacement in the fiber, interface and matrix at $\theta = 90$

3.3.2 The effect of neighboring fibers

3.3.2.1 Using the superposition technique

To test the effect of the neighboring fibers, a superposition technique of Horii and Nemat-Nasser (1985) was adopted. The idea of the superposition technique is to divide the problem into a homogeneous problem and number of sub-problem depending on the number of fibers in the main problem. As shown in figure 3-10, the tested problem consists of five fibers each one is surrounded by a ring of matrix and all the fiber are in an infinitely large plate. The plate material properties are the same as the composite properties. The plate is subjected to a remote tensile stress. The target is to estimate the stress concentration on the central fiber considering the effect of the other four fibers.
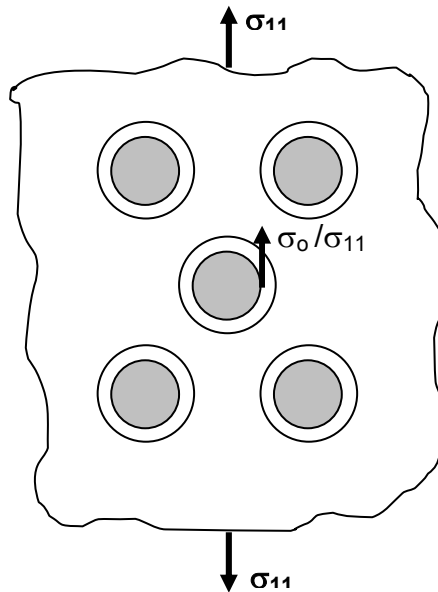
Figure 3-10: The main problem; central fiber surrounded by four fibers

This problem is divided into six sub-problems as shown in figure 3-11. The first sub-problem, a homogeneous problem, represents only a plate without any fibers and subjected to a remote tensile stress. The rest of the five sub-problems represent each surrounding fiber. In each one, the fiber will be considered alone in the plate and subjected to fictitious traction around its boundary. In the cases of sub-problems without tensile stress acting on the plate, the set of equations representing the plate were modified from Savin's work to satisfy the free stress condition at the far field. The stress equations were derived to be as follows:

$$\sigma_r = \frac{P}{2}\left[\left(-\frac{1}{2}\beta_{-1}\cdot\frac{R^2}{r^2}\right)+\left(-2\alpha_{-1}\cdot\frac{R^2}{r^2}-\frac{3}{2}\beta_{-3}\cdot\frac{R^4}{r^4}\right)\cdot\cos(2\cdot\theta)\right]$$

$$\sigma_\theta = \frac{P}{2}\left[\left(\frac{1}{2}\beta_{-1}\cdot\frac{R^2}{r^2}\right)-\left(-\frac{3}{2}\beta_{-3}\cdot\frac{R^4}{r^4}\right)\cdot\cos(2\cdot\theta)\right]$$

$$\tau_{r\theta} = -\frac{P}{2}\left[\alpha_{-1}\cdot\frac{R^2}{r^2}+\frac{3}{2}\beta_{-3}\cdot\frac{R^4}{r^4}\right]\cdot\sin(2\cdot\theta)$$

$$u_r = \frac{P\cdot R}{8\mu}\left\{\left[\beta_{-1}\cdot\frac{R}{r}\right]+\left[\alpha_{-1}\cdot(\eta+1)\frac{R}{r}+\beta_{-3}\cdot\frac{R^3}{r^3}\right]\cdot\cos(2\cdot\theta)\right\}$$

$$u_\theta = \frac{P\cdot R}{8\mu}\left[-\alpha_{-1}\cdot(\eta-1)\frac{R}{r}+\beta_{-3}\cdot\frac{R^3}{r^3}\right]\cdot\sin(2\cdot\theta)$$

No significant difference was found in the stress concentration around the central fiber after considering the effect of the surrounding fibers. This not a surprise since the 2D transverse model considered the effect of the surrounding fibers when equations for a composite plate were used. The plate material was considered as the composite materials which gives the effects of the neighbor fibers.
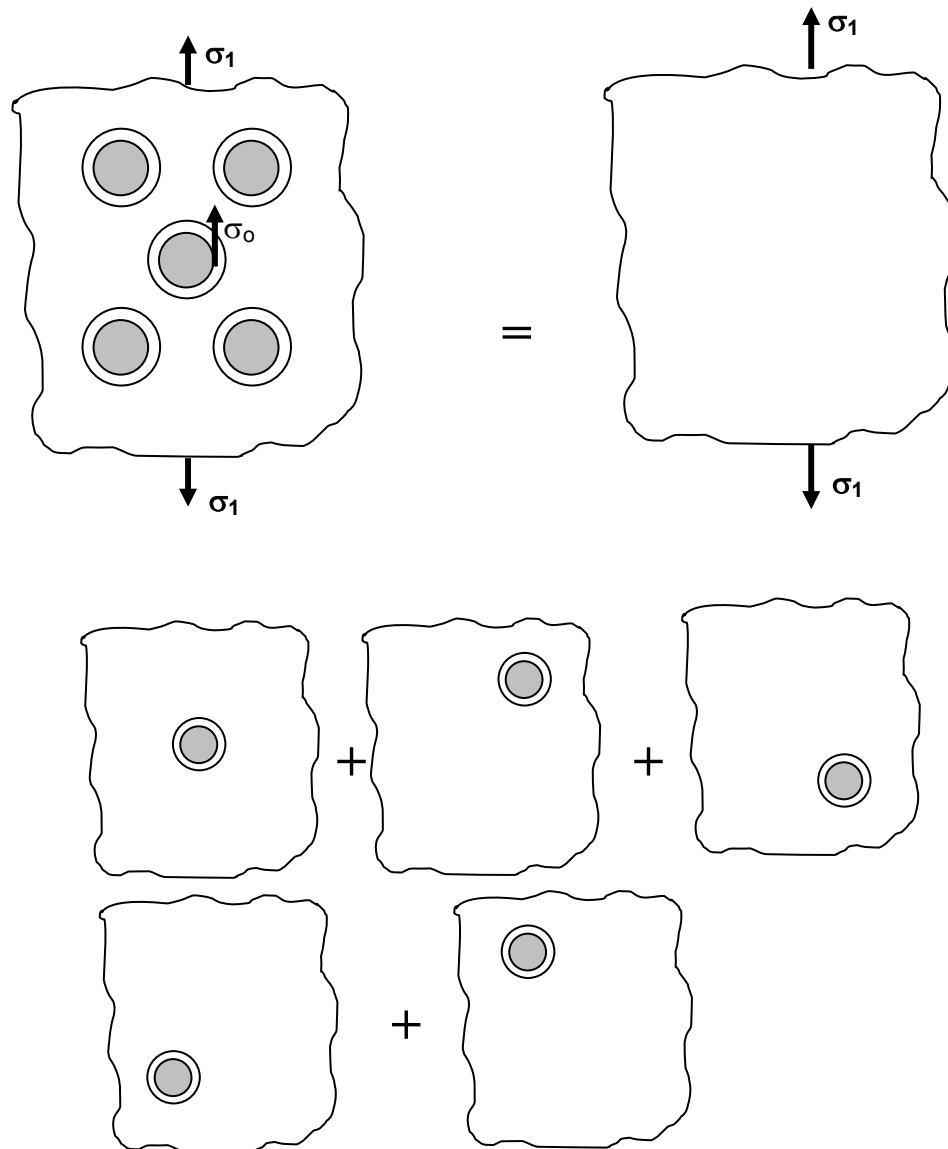
Figure 3-11: Superposition scheme for the main problem

3.3.3   Comparison to other 2D models

In this section the 2D transverse model's results will be compared to the research work

done by Weng in 1984. Weng presented a 2D model expressing stress distribution in a

matrix with inclusions. The matrix and inclusions were assumed to be linearly elastic and

homogeneous. The model estimated the stress concentration on the edge of the inclusion

at $\theta = 90$ as a function of fiber to matrix ratio of Young's modulus $\dfrac{E_f}{E_m}$ for various fiber

volume fractions. The ratio of fiber to matrix Young's moduli, $\dfrac{E_f}{E_m}$, varies from zero,

which presents a hole or void, to one, which represents pure matrix. The stress

concentration was estimated for different volume fractions starting from zero, or single

inclusion, to 75%.

Figure 3-12 shows the results of the two models, the current model and Weng's model.

The dashed lines represent Weng's results and the solid lines represent the 2D transverse

model. As shown in the figure, all curves converge to one when the moduli ratio equals

one (i.e., no stress concentration in pure matrix). Also it can be recognized that the stress

concentration decreases with the decrease in $\dfrac{E_f}{E_m}$. When $\dfrac{E_f}{E_m}$ equals to zero, the case of a

hole, the stress concentration should be 3 as reported by the current model and verified in

section 3.3.1. On the other hand, Weng's results are below 3 for both zero and 25% fiber

volume fraction. The results of the current model are close to Weng's results for fiber

volume fraction equal to 50% and slightly lower than his values at other volume fractions.
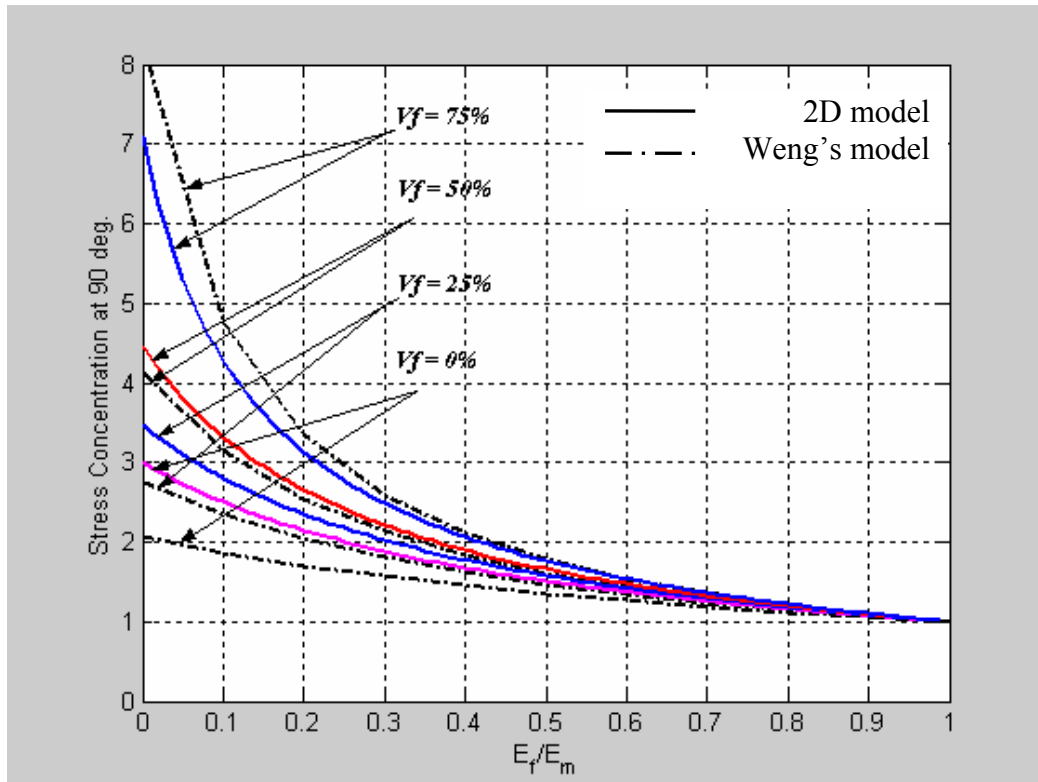
Figure 3-12: Stress concentration at the edge of inclusion as a function of fiber to matrix Young's modulus ratio for different fiber volume fraction

IV. EXPERIMENTAL WORK

4.1 Background

In this chapter the interfacial shear behavior of woven composite materials will be investigated as an application for the stress mapping models that were presented in the previous chapter. Although woven fabric composites exhibit better interlaminar shear behavior than unidirectional composites because of yarn waviness which resists delamination, shear delamination is often considered a weak mode of failure since cracks can still rapidly progress along the un-reinforced region between fabric layers.

In general, textile composites are being considered for higher intra- and interlaminar strength and damage resistance. Interlaminar shear is the stress with which the plies adhere to each other only in the region between the plies. This shear strength is usually not very high in laminated composites because only the relatively weak matrix resin is present to carry the shear stresses in this region. Interlaminar shear stresses are typically induced by an out-of-plane load such as bending stresses.

4.1.1 Modes of interlaminar shear stress

There are types of interlaminar stress that can act to separate one ply from another, figure 4-1:

- Mode I (peeling),
- Mode II (pure shear) and
- Mode III (tearing).
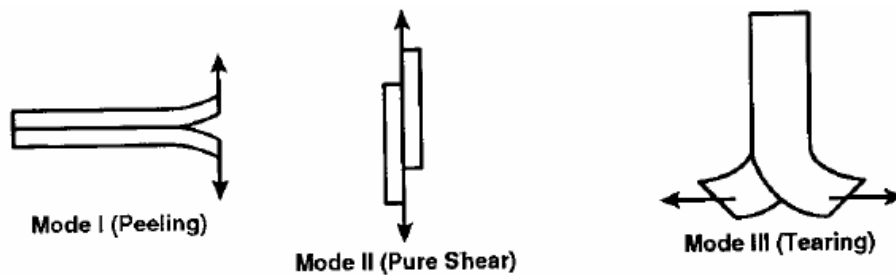
Figure 4-1: Modes of interlaminar shear stress [Nettles 1995]

For laminated composite materials, mode II (pure shear) is of the interest in the current study and bending stresses will be used to give rise to Mode II shear stresses to induce delaminations.

4.1.2 Measuring the interlaminar shear strength

It is important to select the proper method to measure the interlaminar shear strength. Several testing methods are available among which the following three test techniques are favored [Li et al. 1999]:

a) The short-beam shear test and 3-point bend of short beam,

b) Four-point flexural test,

c) Double-notch shear test (double-notched compression DNC)

In the past, engineers have relied on the short beam shear test, as described in ASTM D2344, to examine interlaminar shear failure characteristics, and to provide an estimate of the interlaminar shear strength of composites [Kedward 1972 and Li *et al.* 1999]. As shown in figure 4-2, this test involves the use of a three point flexure specimen, with span to depth ratio chosen to induce interlaminar shear failure. Due to its simplicity, the test method is often used for quality control. However, the test provides only an estimate of the apparent interlaminar shear strength [Short 1995 and Whitney 1989].

Based on observed failure modes, stress analysis and fracture surfaces obtained in conjunction the short-beam shear specimens, considerable difficulty is encountered in interpreting experimental data. In particular, there is evidence that compression stresses in regions where high shear stress components exist tend to induce initial damage in the form of vertical cracks. Such initial damage appears to be necessary in order to induce horizontal interlaminar failures. For specimens without vertical cracks, the failure mode appears to be compressive buckling or yielding in the upper portion of the beam under combined compression and shear [Whitney 1989].

Closer inspection of short beam shear test specimen failure indicates the presence of micro-buckling and micro-cracking in the region near the load nose. It has also been

noticed that initial damage in the form of vertical cracks may be necessary to induce the horizontal interlaminar failures observed. Thus, despite its simplicity and popularity, the short beam shear test method is not appropriate for a general study of interlaminar shear failures of composite materials, for generating design information, or even for a material screening tool [Short 1995 and Whitney 1989].
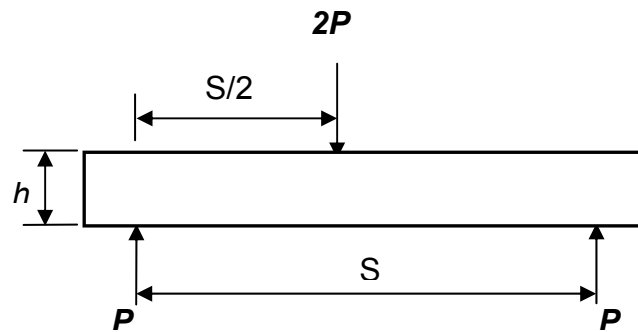
Figure 4-2: Short beam shear test (ASTM D2344)

The four-point flexural test, as shown in figure 4-3, is similar to the three-point bending test, but with use of two loading noses instead of one. This will give larger value for the span-to-depth ratio. This larger value will lead to longer sample which is preferable to give more control on the tested samples. Also, the span-to-depth is an essential factor in any flexural test, so a suitable number of layers should be chosen to get reasonable thickness. Furthermore, it is important to note that the span between the two loading noses is under pure bending.
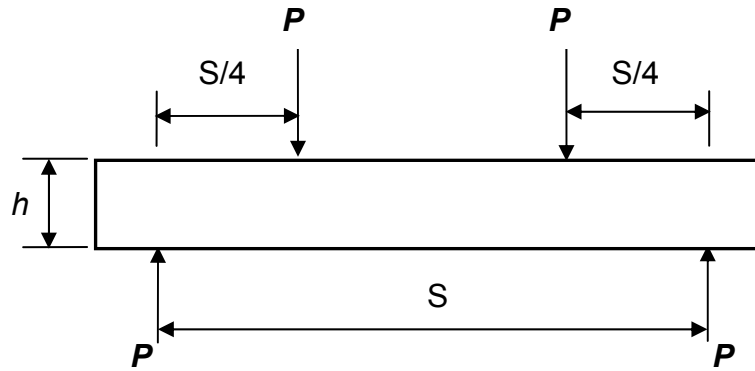
Figure 4-3: Four-point flexural test (ASTM D6272)

Double-notched compression (DNC) test, as shown in figure 4-4, is prescribed by ASTM D3846 as a standard test method for interlaminar shear strength. The ASTM recommends loading a double-notched shear specimen edgewise in compression with supporting fixtures to prevent buckling. Consequently, a shear failure occurs along the longitudinal shear plane between the notches. The measured shear strength may be affected by the supporting fixture/specimen contact friction during the test. The major advantage of DNC over the other techniques is that the interlaminar shear failure occurs consistently. In addition, DNC tests lead to lower shear strength than that of other test methods. The major drawback of DNC tests is the non-uniformity of the stress field in the gage section due in-part to the existence of highly concentrated stresses around notches of the DNC specimen.
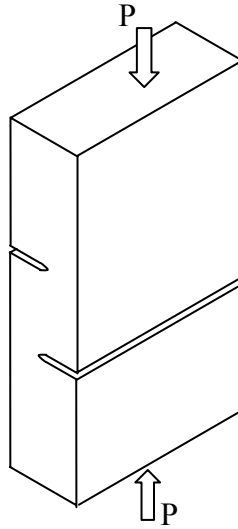
Figure 4-4: Double-notched compression shear test

After careful consideration, the four-point flexural test was chosen in this study because of:

- The existence of a pure bending region between load noses without complex stress-state.

- Test simplicity and straightforwardness of data analysis.

- It is economic in terms material, machining and time.

4.2 Materials

Two types of material were used to fabricate two-dimensional laminated plates: plain weave with E-glass fibers and twill weave with IM7 carbon fibers. Nominal factors provided by the suppliers are given in Tables 4-1. Figure 4-5 shows a plan view of the

fabrics. Shell resin EPON 828 provided by Miller-Stephenson Chemical Co., was used. Resin was mixed with hardener EPIKURE Curing Agent 9553 (formerly known as EPI-CURE 9553 Curing Agent) by weight ratio of 100:15.4.

a) Plain weave (E-glass fiber)   b) Broken twill weave (IM7 carbon fiber)
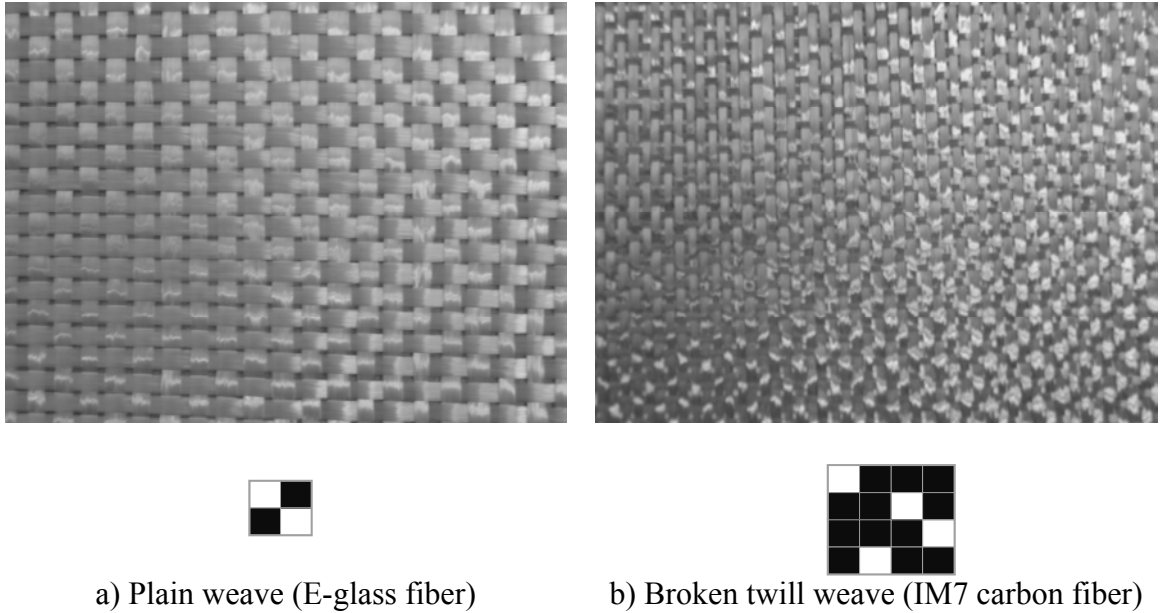
Figure 4-5: Plan view of the fabrics used in the study

Table 4-1: Specifications of fabrics used in the current study

	IM7 Carbon Fiber	Glass Fiber
Fabric structure	Broken twill weave	Plain weave.
Warp tow size (no. of filaments)	6K	3K
Weft tow size (no. of filaments)	6K	3K
Fabric weight (g/m^2)	209	607
Density (g/cm^3)	1.78	2.54
Warp counts /cm	4.5	2
Warp counts /cm	4.5	2
Filament diameter (μm)	6	16
Filament shape	Round	Round

4.3 Molding

There are many methods available to assemble or produce a composite plate such as; compression molding, resin transfer molding (RTM), resin film infusion (RFI), etc. In the current study, compression molding was chosen as a method to assemble composites for its simplicity. As shown in figure 4-6, a hydraulic compressor, Genesis Series 15 (G30 H 15B, Wabash MPI), was used for compression molding.

a) Compressor   b) The control panel

Figure 4-6: Hydraulic compressor, Genesis Series 15 (G30 H 15B, Wabash MPI)

4.4 Fabrication procedures:

1) The surfaces of the bottom and top mold and frame were cleaned using an orbit sander.

2) Fabrics were cut parallel to the yarn direction into designated sizes.

3) Fabric layers used to make composite plate were weighted (W_f).

4) Release agent was applied onto the mold and frame surfaces.

5) The fabric layers were placed in the cavity of molds layer by layer and the resin mixture was loaded between layers. Te resin mixture was evenly distributed on each layer.

6) After loading all layers, release agent was applied onto the surface of the top mold before placing it on the bottom part which contained fabric layers and resin.

7) The mold was placed in the hydraulic press at adjusted heat 120° C and 114 kPa pressure for two hours.

8) After the hot-pressing process, the mold was cooled at room temperature for 24 hours.

9) The composite plate was removed carefully from the mold and weighted (W_c). The composite and fabrics weights are used to calculate the fiber volume fraction using equation 4-1.

$$V_f = \frac{\dfrac{W_f}{\rho_f}}{\dfrac{W_f}{\rho_f} + \dfrac{W_c - W_f}{\rho_m}} \qquad (4\text{-}1)$$

Where: ρ_f and ρ_m are respectively the fiber and matrix densities in (g/cm^3).

10) 2.5 cm from each edge was cut off and discarded to ensure working with an even plate.

11) The plate was cut into sample stripes, all strips lengths were cut parallel to the warp yarns and they were about 1.27 cm width.

12) Strips' edges in length direction were polished with fine sandpaper.

13) Thickness and width were measured for each sample at three different points and averaged.

Four-point flexural test was conducted on a computerized INSTRON 4500, as shown on figure 4-7. the flexural test fixture was designed and manufactured for the purpose of this test. Figure 4-8 shows a schematic for the test fixture. The loading noses and supports have diameters of 5 mm and the test speed was 1 mm/min. The span length (L) varied with the specimen thickness to keep the span-to-depth ratio at 16:1. From the load and specimen dimensions, the apparent mid-plane interlaminar shear stress (τ) was calculated following the ASTM D6272.

Figure 4-7: Computerized INSTRON 4500

Figure 4-9 shows the four-point fixture used to conduct the test. The fixture was designed and manufactured to give much flexibility for changing the span of the upper and lower noses.
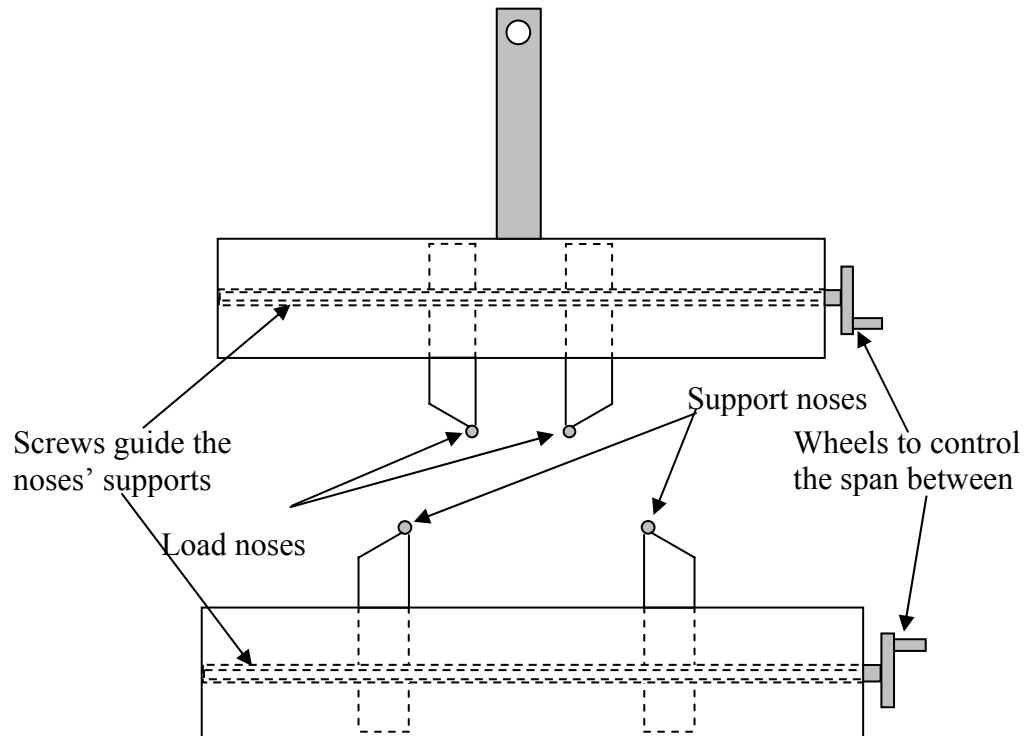
Figure 4-8: Schematic for the flexural test fixture
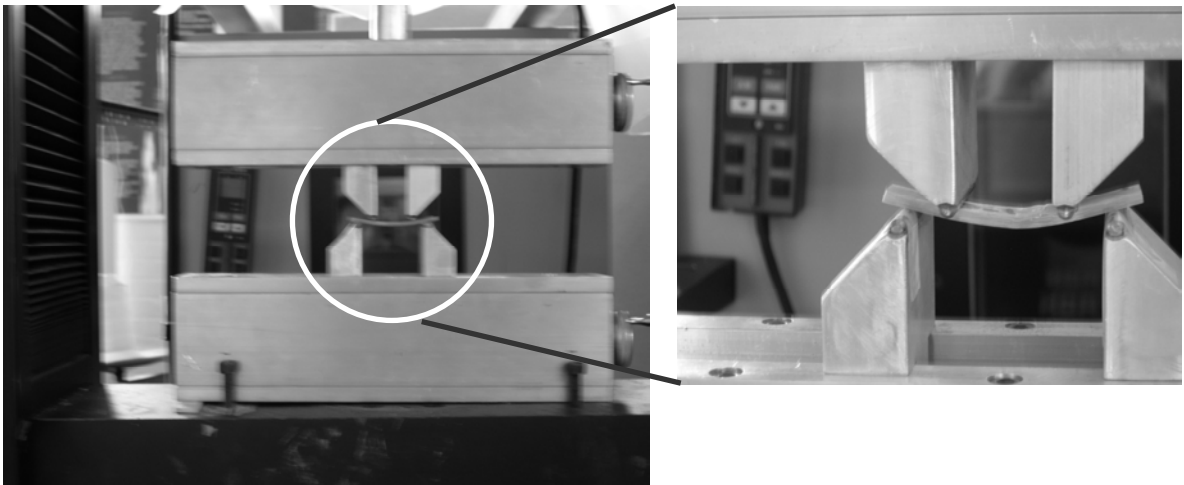
Figure 4-9: Typical pictures for the four-point fixture

V. RESULTS AND DISCUSSION

In this chapter, the following issues will be addressed: i) results of four-point flexural tests will be analyzed and discussed, ii) experimental data will be related to analytical models proposed in chapter three, and iii) model results will be compared to fiber pull-out test from literature.

5.1 Experimental results

5.1.1 Fiber volume fraction

Two woven structures were used in this study - plain weave E-glass fabric and broken twill IM7 carbon fabric. Five panels from each weave structure were manufactured varying the number of layers in each panel (5-9 layers for each structure). The fiber volume fraction of each panel was calculated using equation 4-1 and the results are listed in table 5-1. As shown in table 5-1, the fiber volume fraction increases proportionally by increasing the number of layers due to the constant thickness and the increasing number of layers of panels. The average thickness for the broken twill/carbon weave panels is 2.512 mm and for the plain/glass weave panels is 3 mm. All the individual data points

are within the 95% statistical confidence interval. Five samples were cut out from each panel to the dimensions mentioned in the previous chapter.

Table 5-1: Fiber volume fraction for the manufactured panels

	Fiber volume fraction (%)	
No. of layers	Twill weave (IM7 Carbon fiber)	Plain weave (E-glass fiber)
5	26	50
6	28	52
7	32	55
8	36	58
9	40	60

5.1.2 Load-displacement diagrams

Typical load versus crosshead displacement curves (load-displacement curves) of four-point flexural tests showed nonlinearity in the initial stage of the loading, as shown in Figure 5-1. This nonlinearity mainly stems from the self-aligning processes between the test fixture and the specimen which occur during initial loading. The nonlinear part was removed from the curve for further analysis and the linear part extended to meet the x-

axis. The intersection point of the linear part and the x-axis was assumed as the origin of the curve. Appendix D load displacement curves for all tested specimens.

Stress and strain were calculated following the ASTM standards to obtain stress-strain curves for each sample. Figure 5-2 shows typical stress-strain curves for five samples from the seven layers panel of broken twill/carbon weave. All other stress-strain curves are shown in Appendix D.
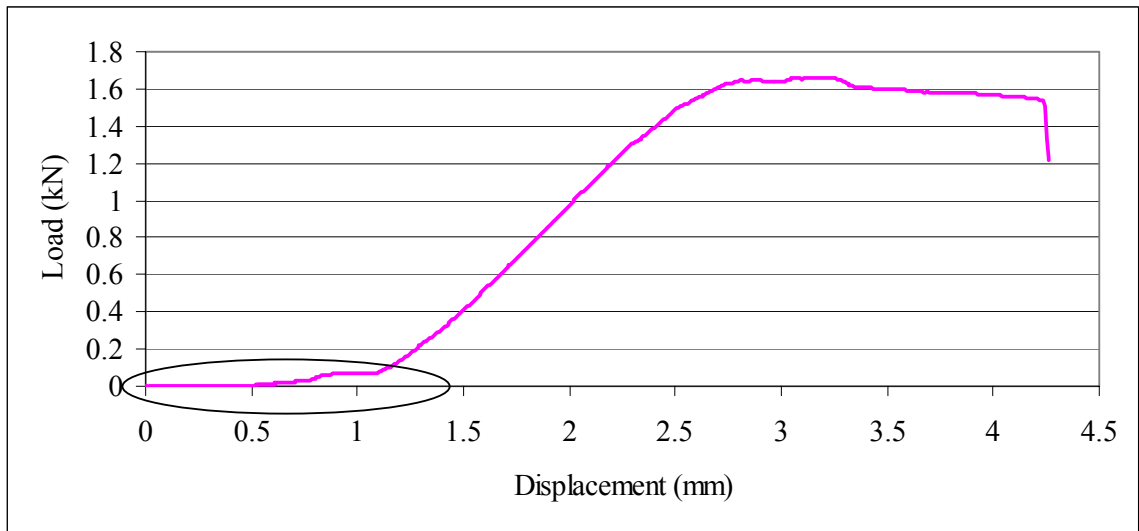
Figure 5-1: Typical load versus crosshead displacement curve

5.1.3 Shear modulus

The shear moduli were calculated using pcGINA (Gowayed 1996) for each panel for different layers and results are reported in table 5-2. As shown in table 5-2 and figures 5-3, the shear modulus increases linearly with increasing the volume fraction. Also, the

shear modulus of the plain/glass weave is greater than the twill/carbon weave and this is mainly due to the isotropy of the glass fibers. It should be noted, that the slope of the glass is greater than the slope of the carbon.
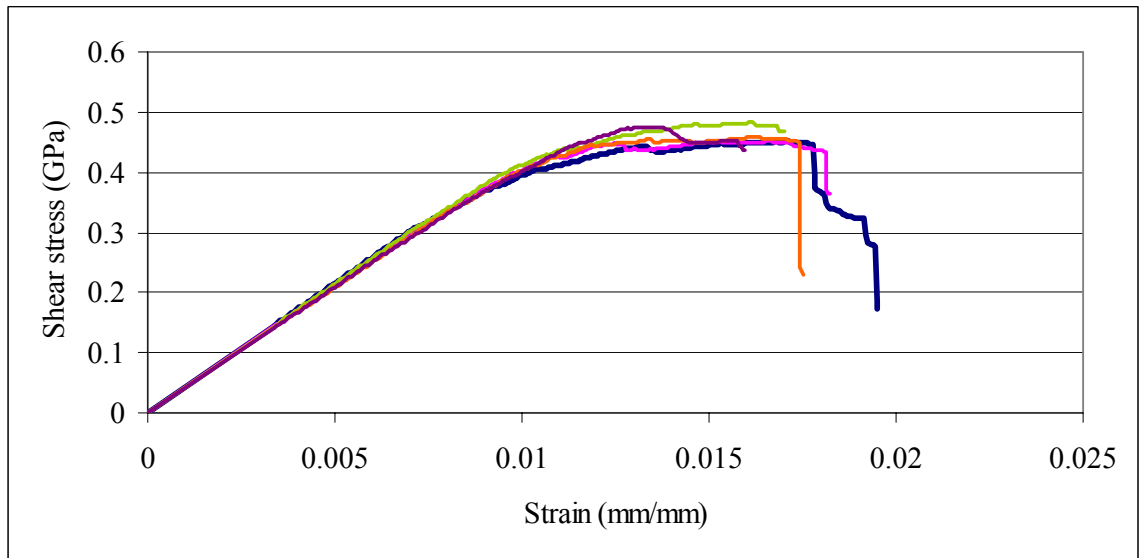
Figure 5-2: Tensile stress in the bottom layer versus strain curves for 7 layers twill/carbon weave

It is expected to find this increase not only due to the increase in the fiber volume fraction but also because of the increase in nesting between layers. As mentioned earlier, the number of layers was increased within each fabric type while maintaining a constant thickness for the panels and by doing this the nesting between layers increased as well as the fiber volume fraction.

Table 5-2: Shear moduli (GPa) calculate using pcGINA for the manufactured samples.

No. of layers	Twill weave (IM7 Carbon fiber)	Plain weave (E-glass fiber)
5	2.54	4.61
6	2.61	4.85
7	2.77	5.26
8	2.91	5.70
9	3.06	6.05

Figure 5-3: Shear moduli (pcGINA) versus fiber volume fraction

5.1.4 Nesting between layers

Nesting is an important phenomenon that affects mechanical performance of textile composites in general and its interlaminar shear strength in particular. It is defined as: *In reinforced composites, a laminate where the plies are placed and the yarns of one ply lie in the valleys between the yarns of the adjacent ply* [Morena 1997]. There were many attempts to measure the ne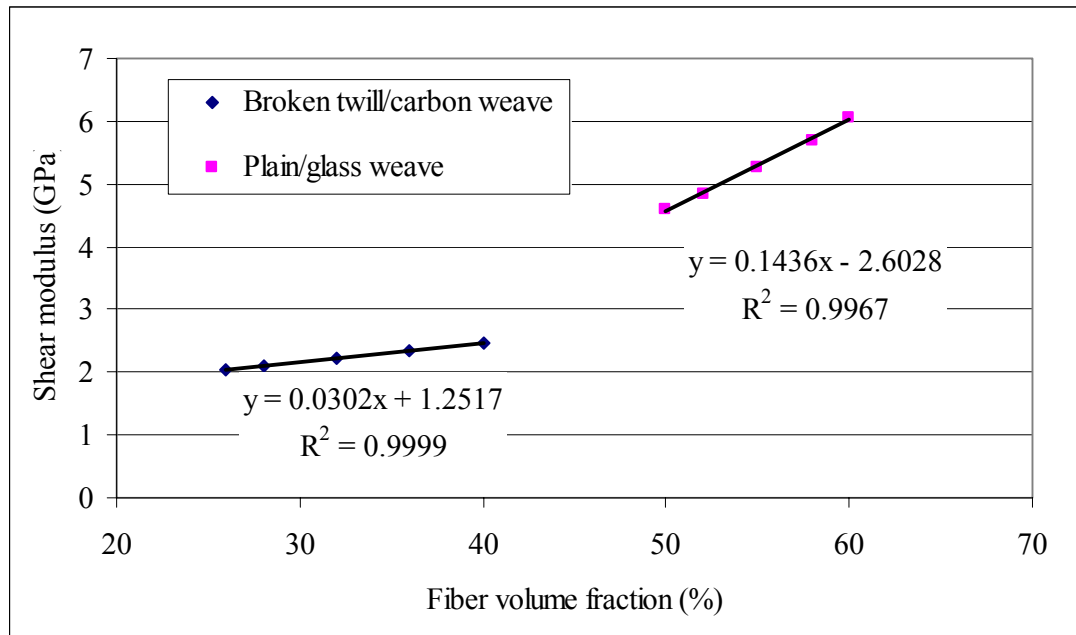sting in textile composites and obtain a quantified value to represent the nesting. The crimp angle, which is defined as: *The maximum angular deviation between the local yarn direction and the plane of the cloth layer,* was used as a measure for nesting [Jortner 1989]. The average crimp angle shows how much flattening the layers have. Since the nesting is not represented only by compaction but also by the shift between layers, Ito and Chou [1997, 1998] used two parameters to estimate the nesting; the shift between layers represented by phase angle and the layer compaction represented by waviness ratio which is a ratio of the yarn height to its wavelength. As an indicator for nesting the average thickness of the layers can be used because the layers are compressed during nesting. As an example, micrographic images of broken twill/carbon weave along the warp direction were captured; samples of the images are shown in figure 5-4. It can be seen that the thickness of layers got smaller as the number of layers increased within an almost constant thickness. The thickness for each layer was measured and averaged then compared to the panel's thickness.

5 Layers

6 Layers

7 Layers
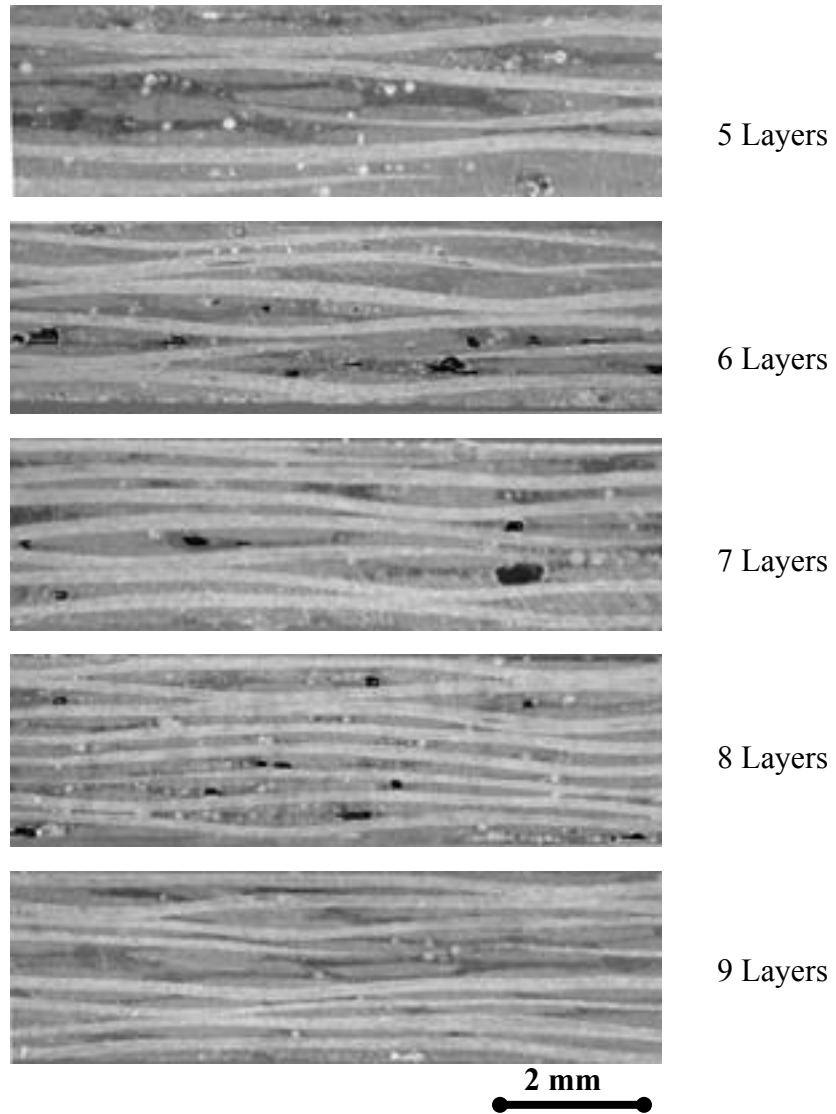
8 Layers

9 Layers

2 mm

Figure 5-4: Cross-sectional view of selected samples with dif

ferent number of layers for broken twill/carbon weave

In figure 5-5 the relationship between the fiber volume fraction and layer thickness as a
fraction of the panel thickness is shown. A power law curve fit is used to represent the
data.
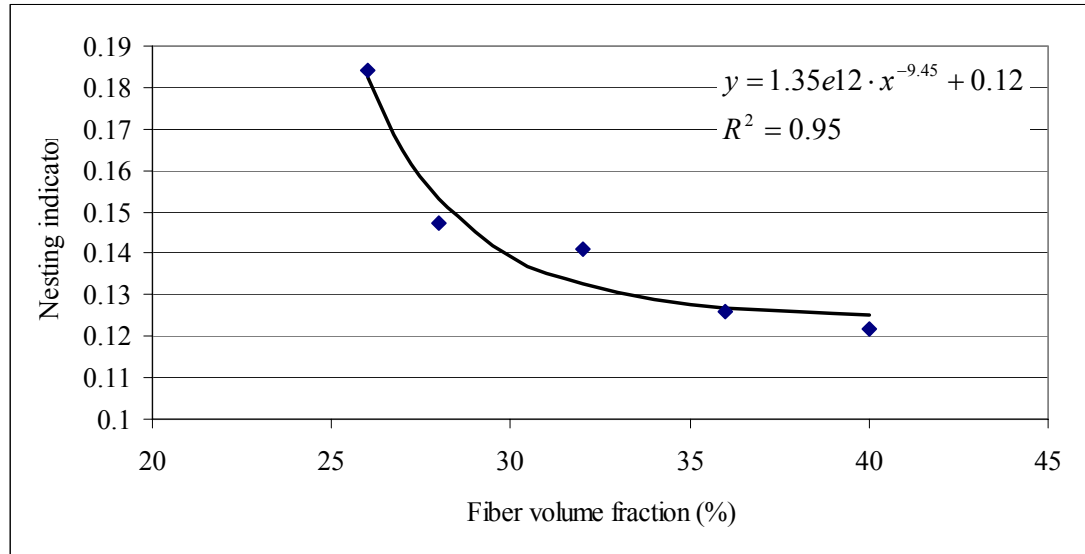
Figure 5-5: Relationship between fiber volume fraction and layer's thickness as a fraction

of the panel thickness for the broken twill/carbon weave

5.1.5 Crack initiation and maximum shear stress

There are two points in the stress-strain curves of the most importance in this study - the

first point is located at the initiation of non-linearity in the curve and the second point is

located at the maximum tensile stress at the bottom layer, figure 5-6. An audible sound

can be heard during the test, this sound is accompanied with the departure from linearity

in the stress-strain curve. This sound was assumed to result from energy release from

crack initiation. The first audible sound was heard at the point of departure from linearity

in the stress-strain curve. This was followed by more audible crack sounds in the non-

linear region with a frequency that increased with the increase in the strain value. After

crack initiation, the tensile stress at the bottom layer continued to increase until failure.
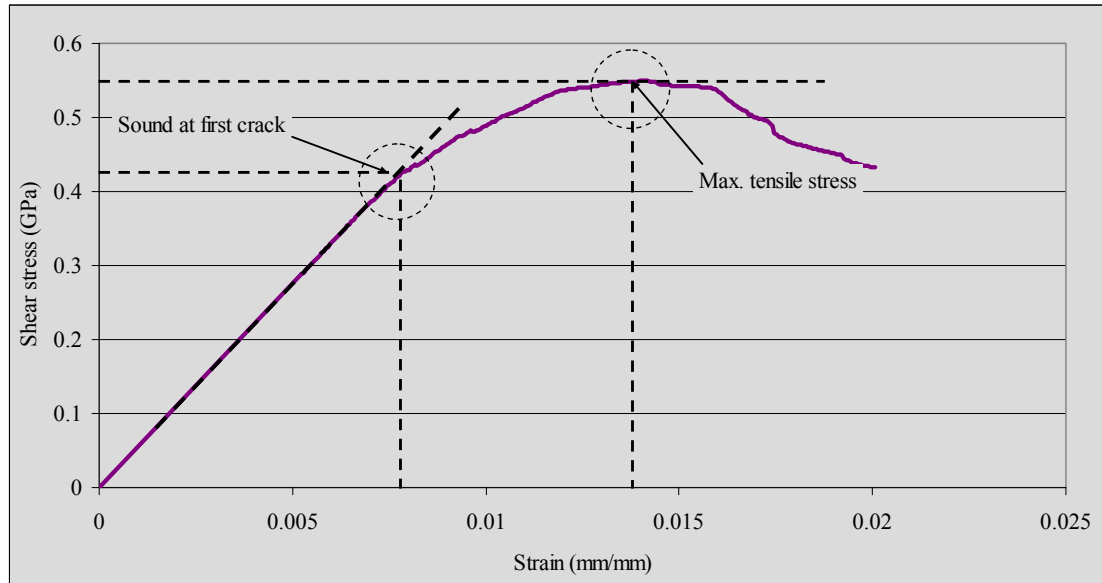
Figure 5-6: Stress-strain curve for a 9 layers sample of broken twill/carbon weave

5.1.6 Time interval between crack initiation and maximum tensile stress

The time interval between the crack initiation and the maximum tensile stress at the bottom layer, representing the time needed for crack saturation and failure, is affected by two major parameters - nesting between layers and the amount of resin between layers. It seems that nesting resists the crack propagation between layers, low resin content between layers may induce "dry" fibers that will increase the probability of crack propagation. As shown in figures 5-7 and 5-9, this time interval increased for the first two volume fractions of the broken twill/carbon weave and the first three volume fractions for the plain/glass weave and then decreased after that. Increasing nesting between layers will increase the length of the crack path and enhance delamination resistance. As nesting increases the volume of resin will decrease. This may cause some of the fibers to have little or no resin layer surrounding them creating new possible crack paths. In figure 5-8,

73

the relationship between layer's thickness, as a nesting indicator, and the time interval has the same trend as the fiber volume fraction.

Figure 5-7: Time consumed in the interval between crack initiation and maximum tensile stress versus fiber volume fraction for the broken twill/carbon weave
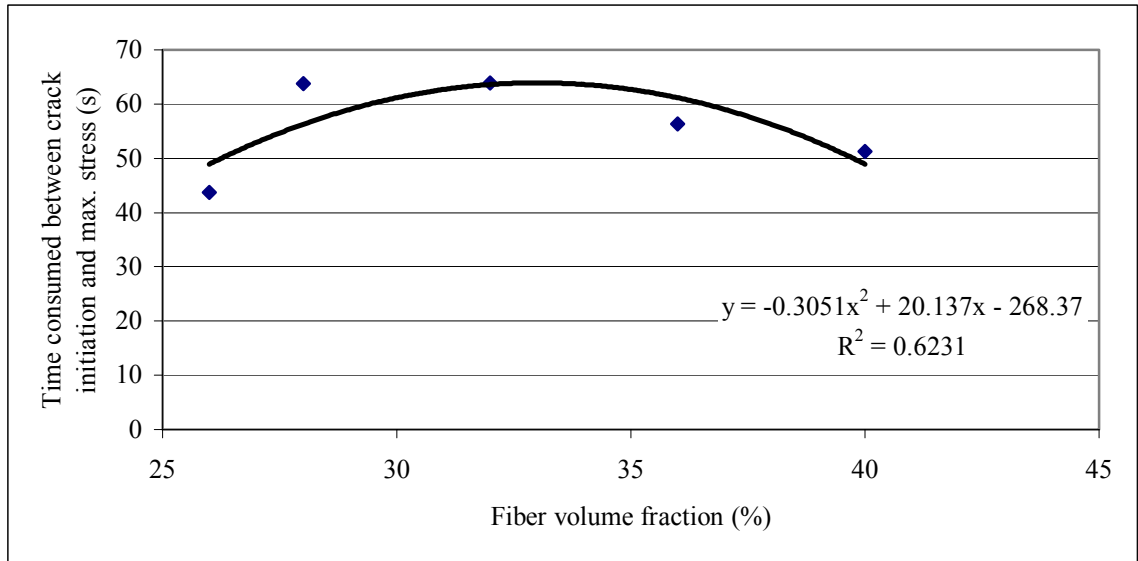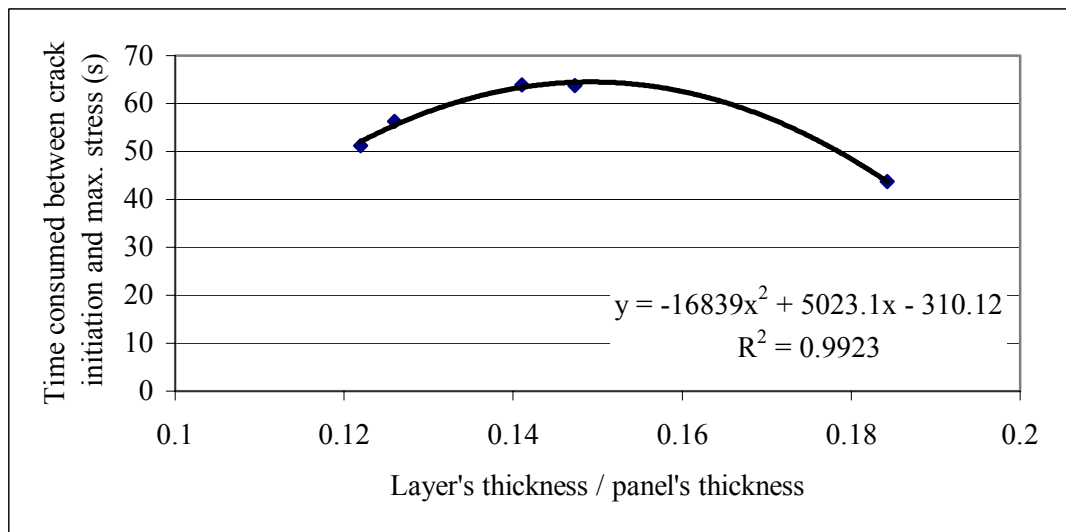

Figure 5-8: Time consumed in the interval between crack initiation and maximum tensile stress versus layer's thickness/panel's thickness for the broken twill/carbon weave

The chart shows data with equation:
$$y = -1.5192x^2 + 166.31x - 4497.8$$
$$R^2 = 0.7409$$

With y-axis "Time consumed between crack initiation and max. tensile stress (s)" and x-axis "Fiber volume fraction (%)".
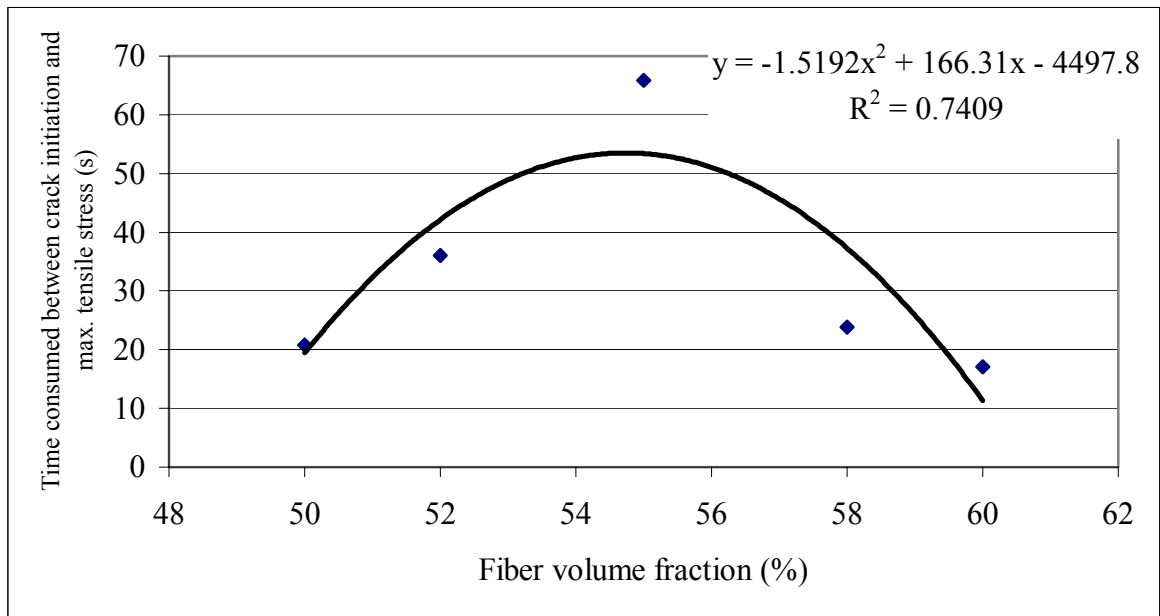
Figure 5-9: Time consumed in the interval between crack initiation and maximum tensile stress versus fiber volume fraction for the plain/glass weave

Tables 5-3 and 5-4 report stresses and strains at the crack initiation and at maximum tensile stress extracted from the curves. As shown in figure 5-10, the tensile stress at crack initiation and the maximum tensile stress increased with increasing the fiber volume fractions in the twill/carbon samples. This increase was not as evident for plain/glass samples, figure 5-12.

Figure 5-11 shows the effect of the nesting indicator on the tensile stress at crack initiation and maximum tensile stress. It shows that with decreasing the layer thickness as a fraction of panel thickness, which means increasing the nesting between layers, the

tensile stress at the bottom layer increases. A power law curve fit was used to represent the relationship. This should be expected because increasing nesting between layers makes the crack path in the resin between the layers longer raising the tensile strength.

Table 5-3: Tensile stresses and strains in the bottom layer of laminate at crack initiation and at maximum tensile stress for the broken twill/carbon weave

Fiber volume fraction (%)	At first crack sound		Max. tensile stress	
	Strain (mm/mm)	Stress (GPa)	Strain (mm/mm)	Stress (GPa)
26	0.0083	0.325	0.0142	0.415
28	0.0084	0.288	0.0158	0.391
32	0.0090	0.373	0.0155	0.464
36	0.0081	0.367	0.0142	0.485
40	0.0081	0.420	0.0134	0.535
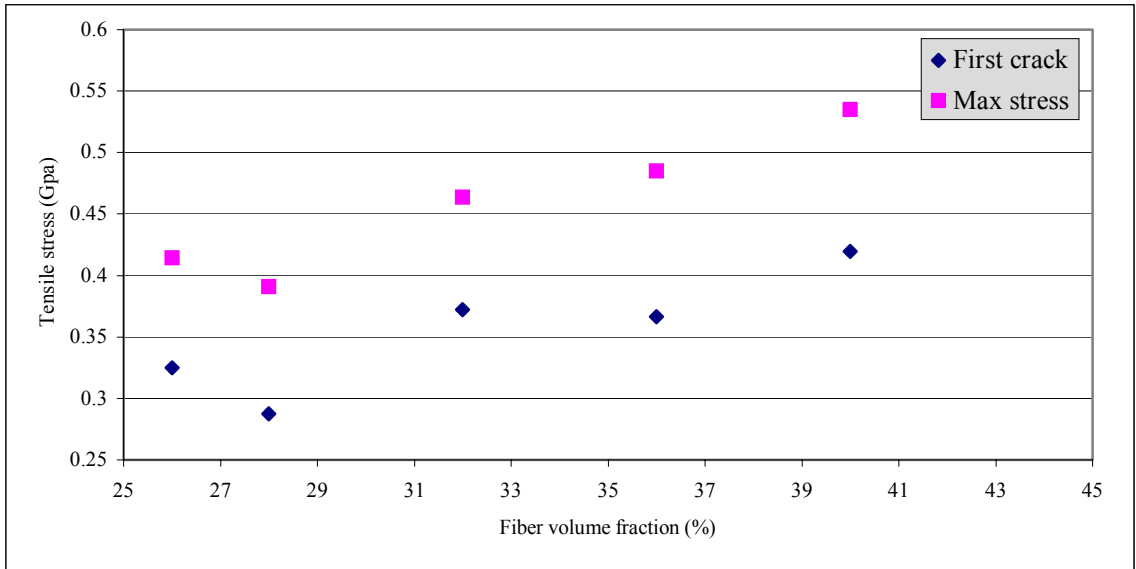
Figure 5-10: Stress at crack initiation and max stress versus fiber volume fraction for the

broken twill/carbon weave
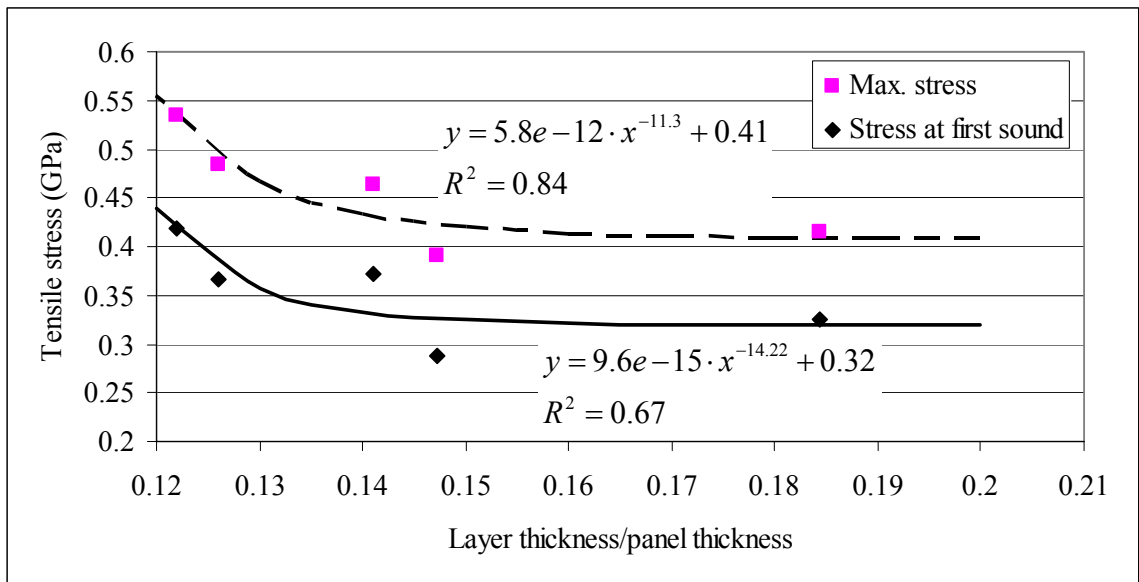
Figure 5-11: Stress at crack initiation and max stress versus layer thickness for the broken

twill/carbon weave

Table 5-4: Tensile stresses and strains in the bottom layer of laminate at maximum tensile

stress for the plain/glass weave

Fiber volume fraction (%)	At first crack sound		Max. tensile stress	
	Strain (mm/mm)	Stress (GPa)	Strain (mm/mm)	Stress (GPa)
50	0.0160	0.365	0.0186	0.402
52	0.0133	0.326	0.0171	0.379
55	0.0124	0.324	0.0185	0.388
58	0.0119	0.361	0.0139	0.394
60	0.0119	0.3661	0.0132	0.379
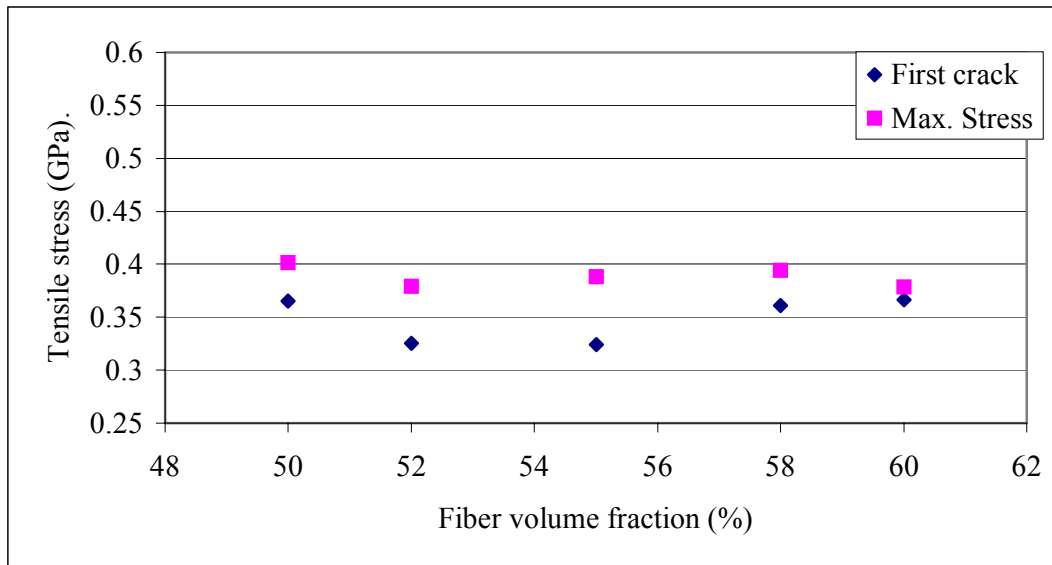
Figure 5-12: Stress at crack initiation and max. stress for the plain/glass weave

In figures 5-13 and 5-14, show groups of stress-strain curves representing each panel (five curves per panel). The nearest curve to the average was chosen to represent the panel. As shown, these two figures are summarizing the results for the moduli and the maximum tensile stress. It can be seen that increasing the number of layers, as well as fiber volume fraction, caused an increase in the slope of straight segment of each curve (i.e., an increase in the moduli).
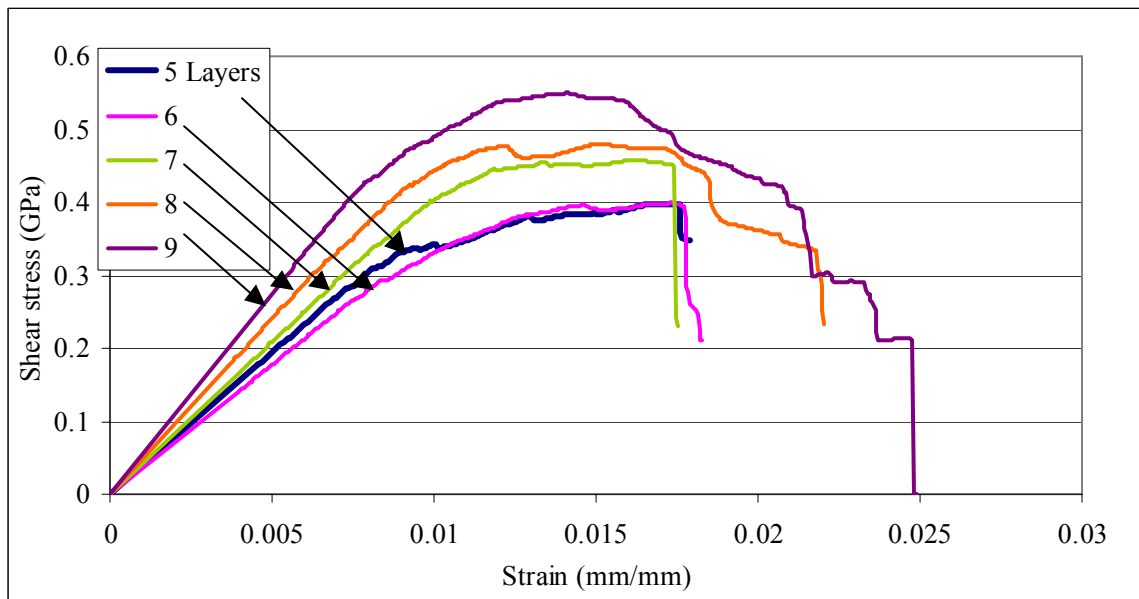
Figure 5-13: Tensile stress in the bottom layer versus strain of the broken twill/carbon fabric for different number of layers
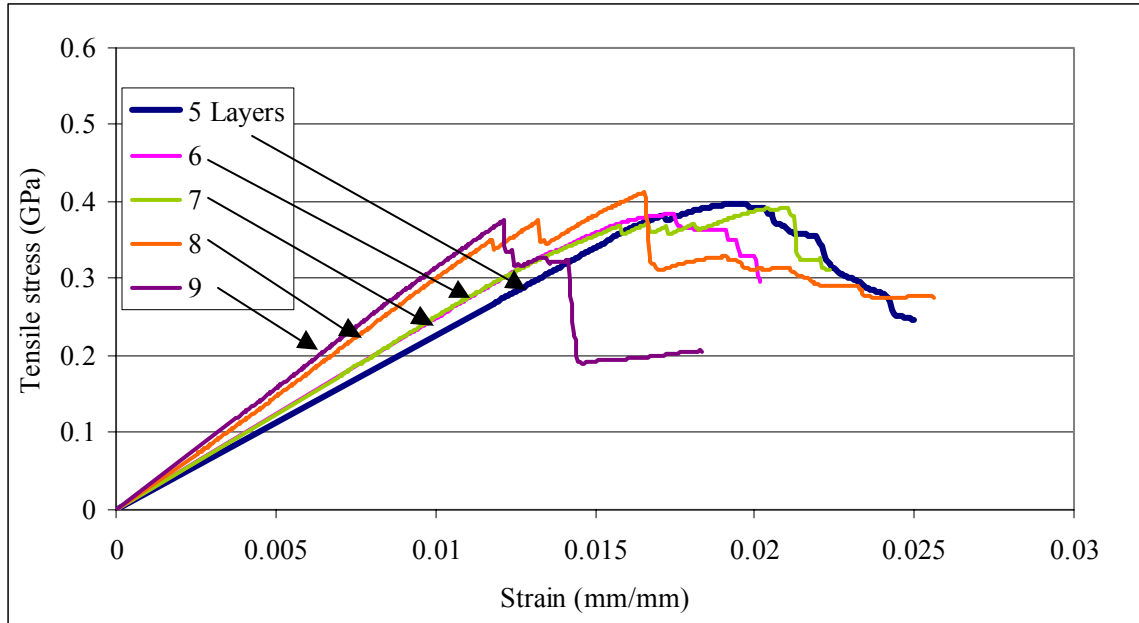
Figure 5-14: Tensile stress in the bottom layer versus strain of the plain/glass fabric for

different number of layers

5.2 Utilization of experimental data in analytical model

In this section, models proposed in chapter three will be used to analyze experimental results. A two step modeling approach will be adopted to utilize the experimental data and be able to use the micro-level models. At the first level a numerical model (pcGINA) available in literature will be used to obtain mid-plane stresses and strains from experimental data. These stress and strain values are used in the proposed micro-level models.

5.2.1 Overview on pcGINA (Graphical Integrated Numerical Analysis)

The Graphical Integrated Numerical Analysis (pcGINA) has been developed at Auburn University to model the mechanical and thermal behavior of textile composites. This is a two-part model. First a geometrical model is used to construct the textile preform and characterize the relative volume fractions and spatial orientation of each yarn in the composite space. Data acquired from the geometrical analysis is used by a hybrid finite element approach to model the composite mechanical and thermal behavior.

The geometrical model used in pcGINA starts by modeling the preform forming process – weaving or braiding, figure 5-15. An ideal fabric geometrical representation is constructed by calculating the location of a set of spatial points ''knots'' that can identify the yarn center-line path within the preform space. A B-spline function is utilized to approximate a smooth yarn centerline path relative to the identified knots. The B-spline function is chosen as the approximation function due to its ability to minimize the radius of curvature along its path and its C^2 continuity. The final step in this model is carried out by constructing a 3-D object (i.e. yarn) by sweeping a cross section along the smooth centerline forming the yarn surface.

A repeat unit cell of the modeled preform is identified from the geometric model and used to represent a complete yarn or tow pattern. A hybrid finite element approach is used to divide the unit cell into smaller subcells. Each subcell is a hexahedral brick element with fibers and matrix around each integration point. A virtual work technique is

applied in the FE solution to calculate the properties of the repeat unit cell. The unit cell properties are considered to be representative of the composite properties.

Currently, pcGINA can predict, with a good level of accuracy, the elastic properties, thermal conductivities, thermal expansion coefficients for textile composite materials for 2D fabrics (e.g., plain weaves and n-HS), biaxial and triaxial braids, angle and layers interlock weaves, and orthogonal 3D weaves.
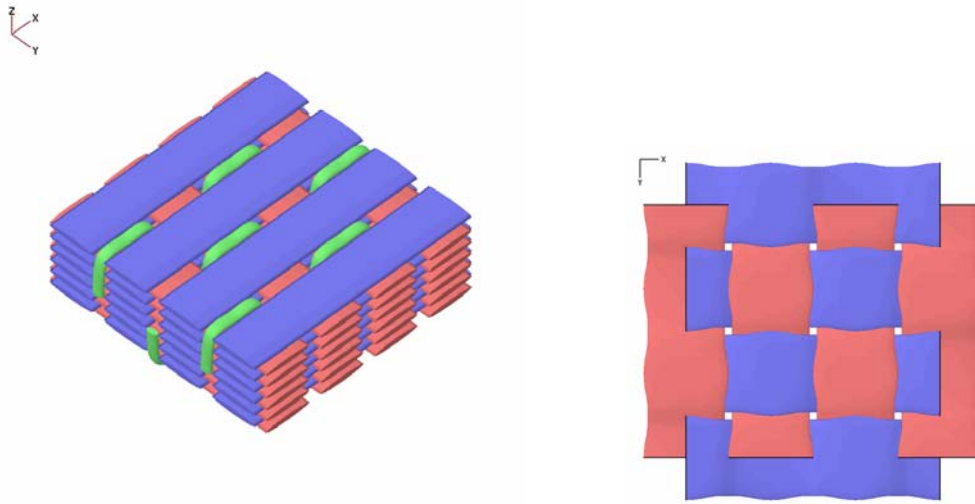
Figure 5-15: Orthogonal fabric (left) and compressed plain weave fabric (right) as modeled by pcGINA.

5.2.2 Using pcGINA

Tensile stresses at the crack initiation were used as an input tensile stress for pcGINA. Each panel was modeled using the fabric structure, fiber volume fraction and fiber properties. As outputs, pcGINA calculated the composite properties, tensile moduli, shear moduli and Poisson ratios as shown in figures 5-16 and 5-17. In addition, pcGINA calculated the stress and strains distributions in the unit cell. Figures 5-18 to 5-21, show examples of the stress and strain distribution for carbon and glass fabrics.

Figure 5-16: Results of IM7 carbon fiber, 40% fiber volume fraction

Figure 5-17: Results of E-glass fiber, 60% fiber volume fraction
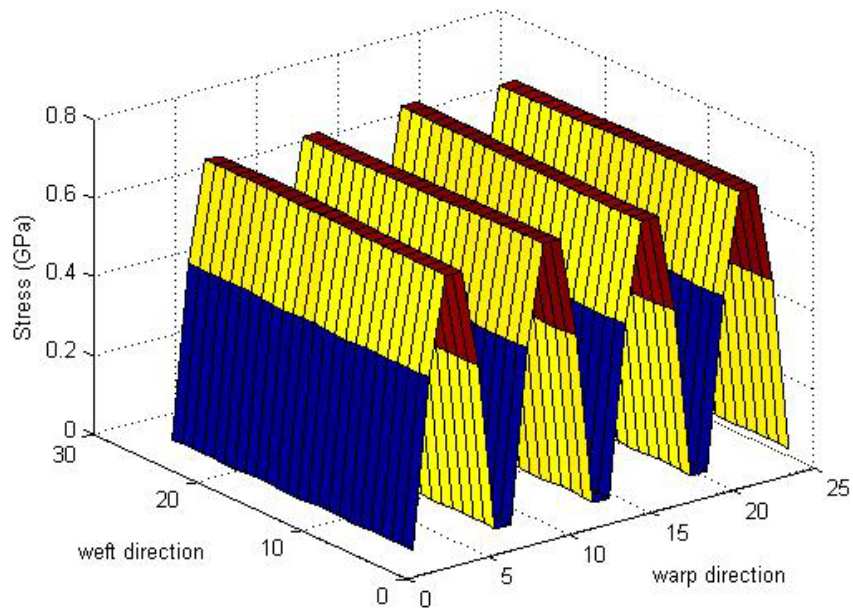
Figure 5-18: Stress distribution for IM7 carbon, 40% fiber volume fraction
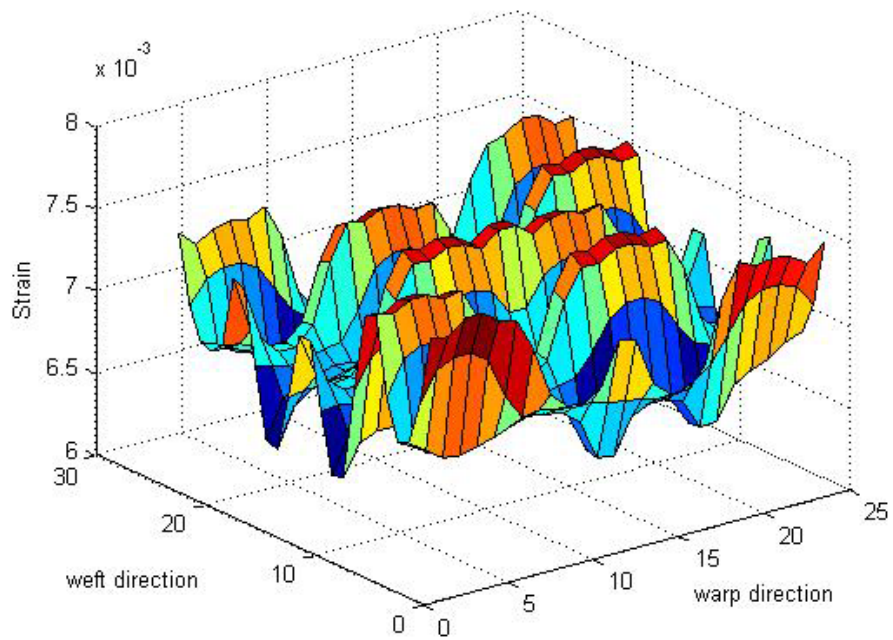
Figure 5-19: Strain distribution for IM7 carbon, 40% fiber volume fraction
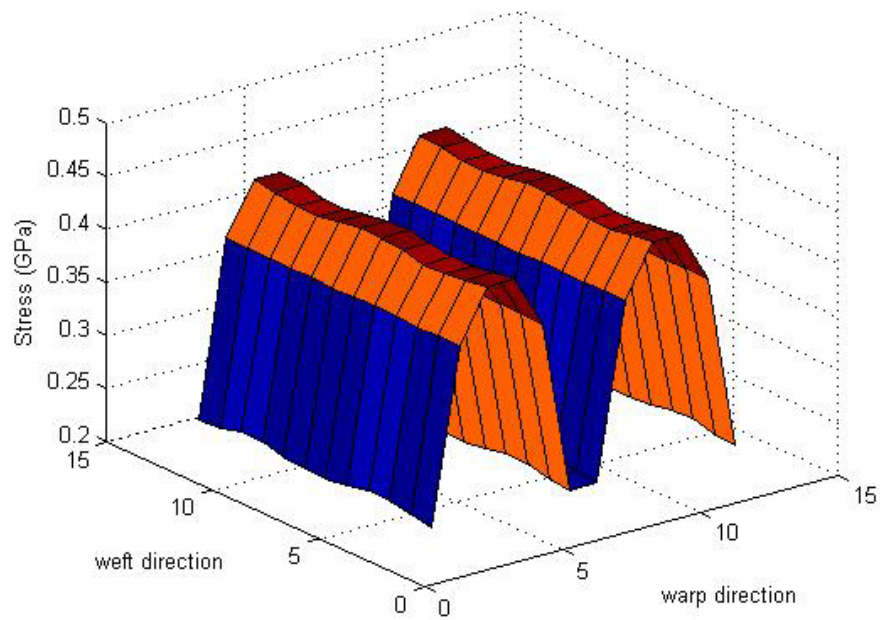
Figure 5-20: Stress distribution for E-glass, 60% fiber volume fraction
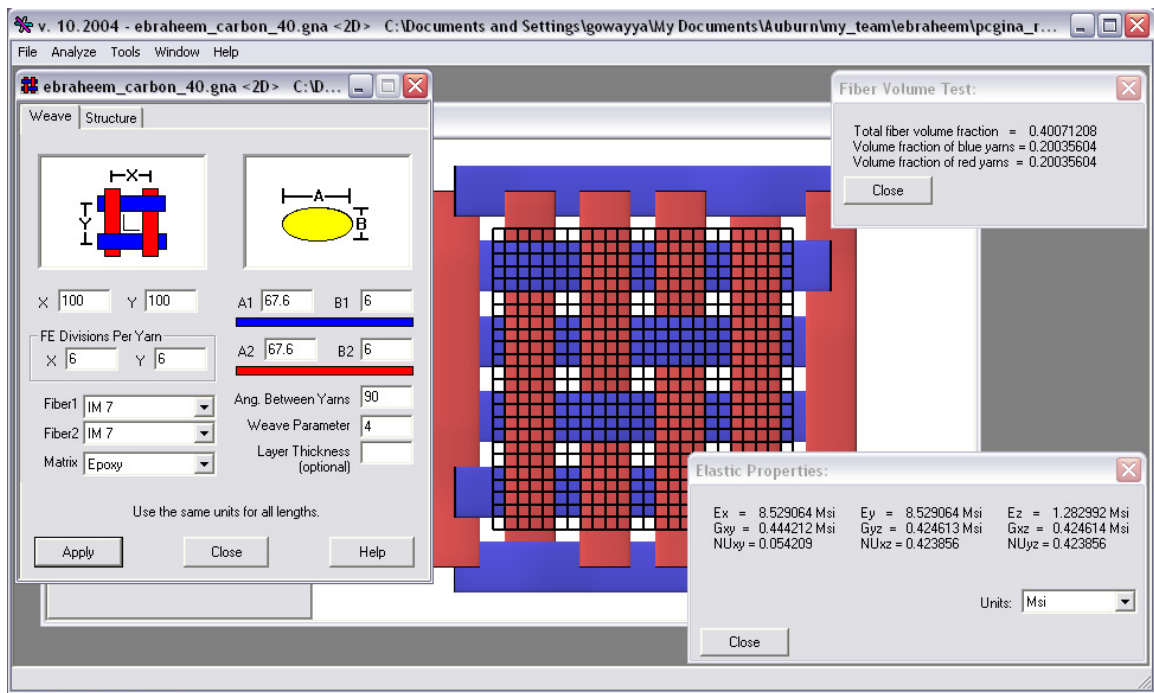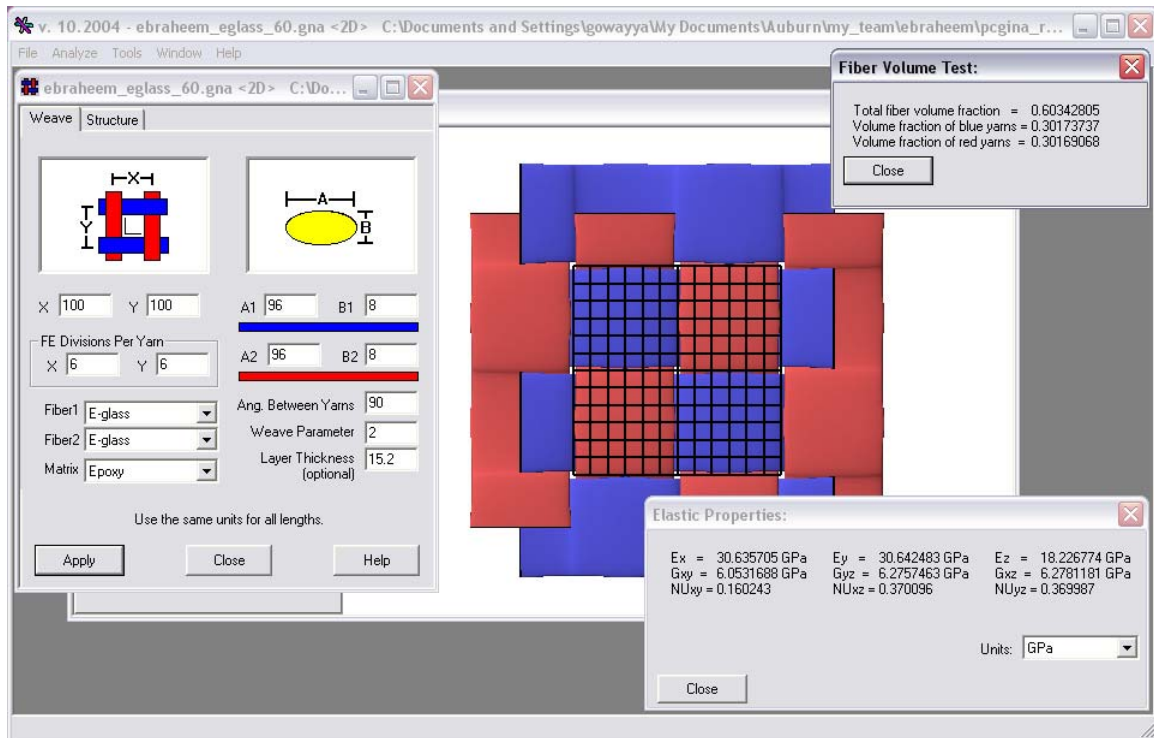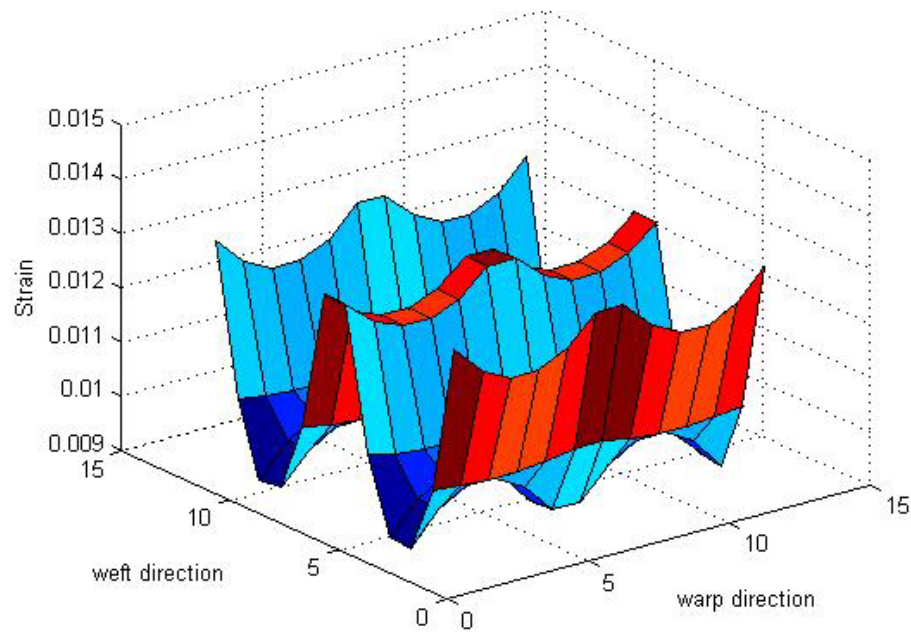
Figure 5-21: Strain distribution for E-glass, 60% fiber volume fraction

The maximum stress for each panel, located at yarn crossover point, which represents the maximum laminate stress was extracted and listed in table 5-5 along with the experimental stress value at crack initiation. As expected, stress concentration in the composite laminate was evident and decreased with the increase in fiber volume fraction. These maximum stresses were used as an input for the models proposed in third chapter assuming that interfacial shear failure between the fiber and matrix occurred at this stress value. Using the two models, the stress distribution was calculated in all the composite constituents, fiber, matrix and surrounding composite. Examples for stress distribution are shown for broken twill/carbon fabric with 40% fiber volume fraction, figures 5-22, and plain/glass fabric with 60% fiber volume fraction, figures 5-23.

Table 5-5: Laminate failure stresses; experimental and calculated using pcGINA for the manufactured samples.

No. of layers	Broken twill/carbon weave		Plain/glass weave	
	Experimental Stress(GPa)	Laminate stress (GPa)	Experimental Stress(GPa)	Laminate stress (GPa)
5	0.325	0.762	0.365	0.489
6	0.288	0.645	0.326	0.426
7	0.372	0.766	0.324	0.410
8	0.367	0.688	0.361	0.441
9	0.420	0.724	0.366	0.447

As shown in figures 5-22 and 5-23, the maximum variation in the stress distribution happened at the fiber/matrix interface in the longitudinal fibers. This stress variation was assumed to be the stress responsible for crack initiation.

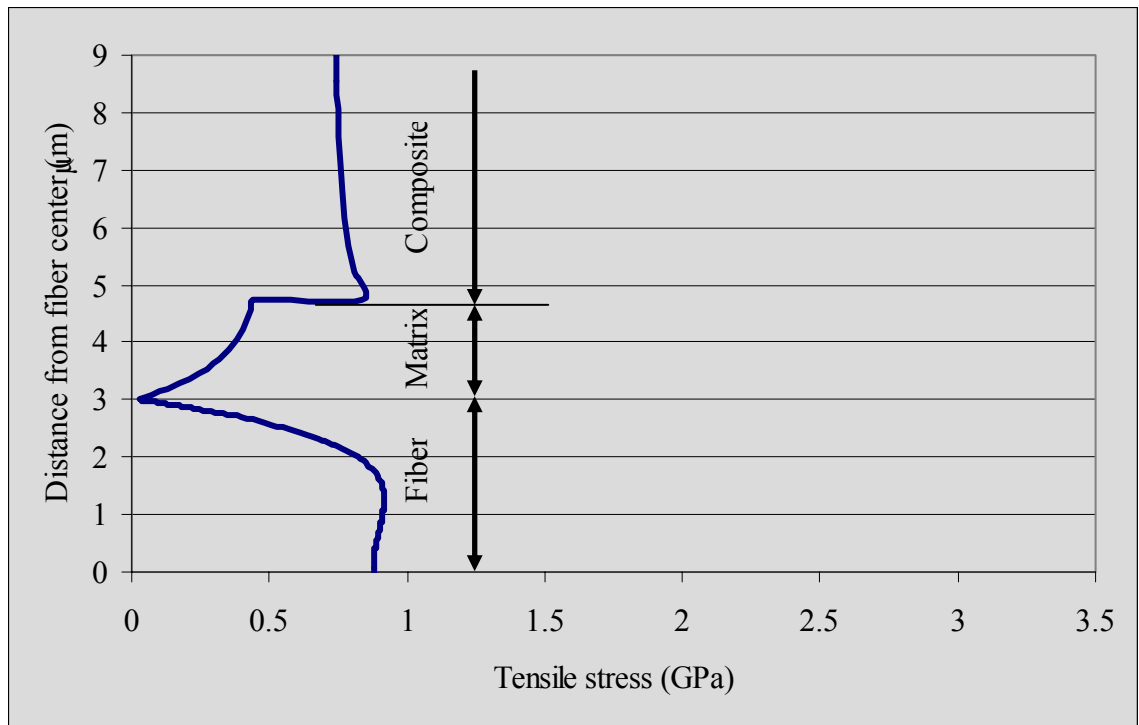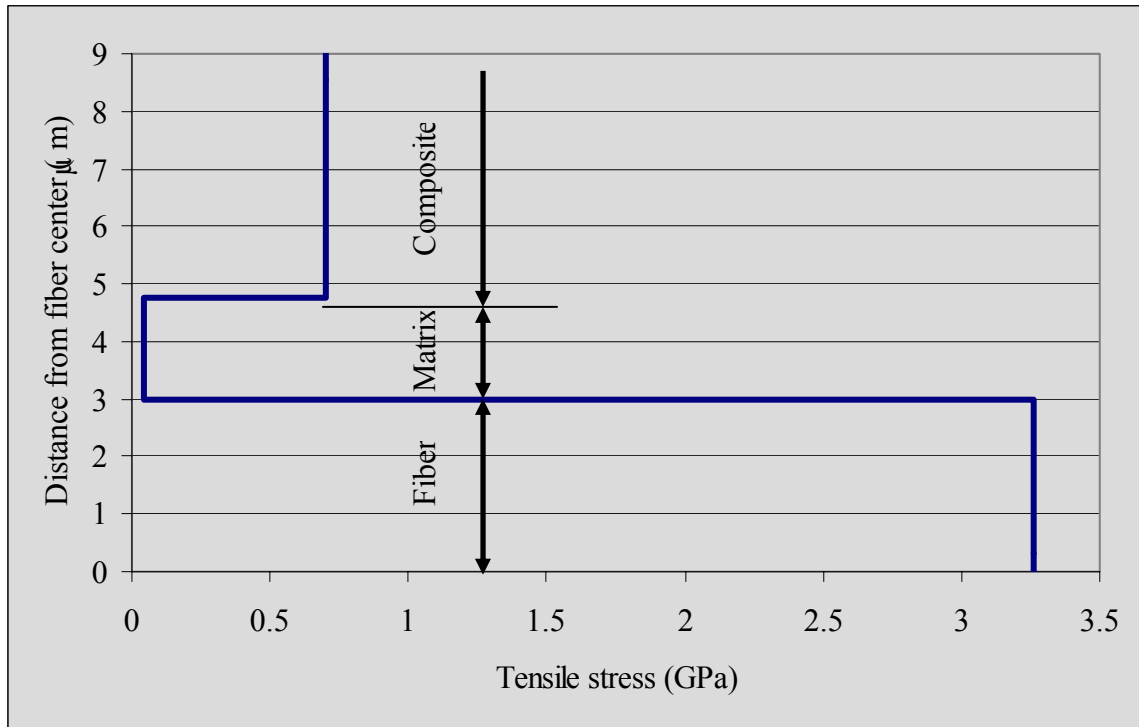Figure 5-22: Tensile stress distribution in x-direction for longitudinal and transverse

models, for broken twill/carbon fabric with 40% volume fraction
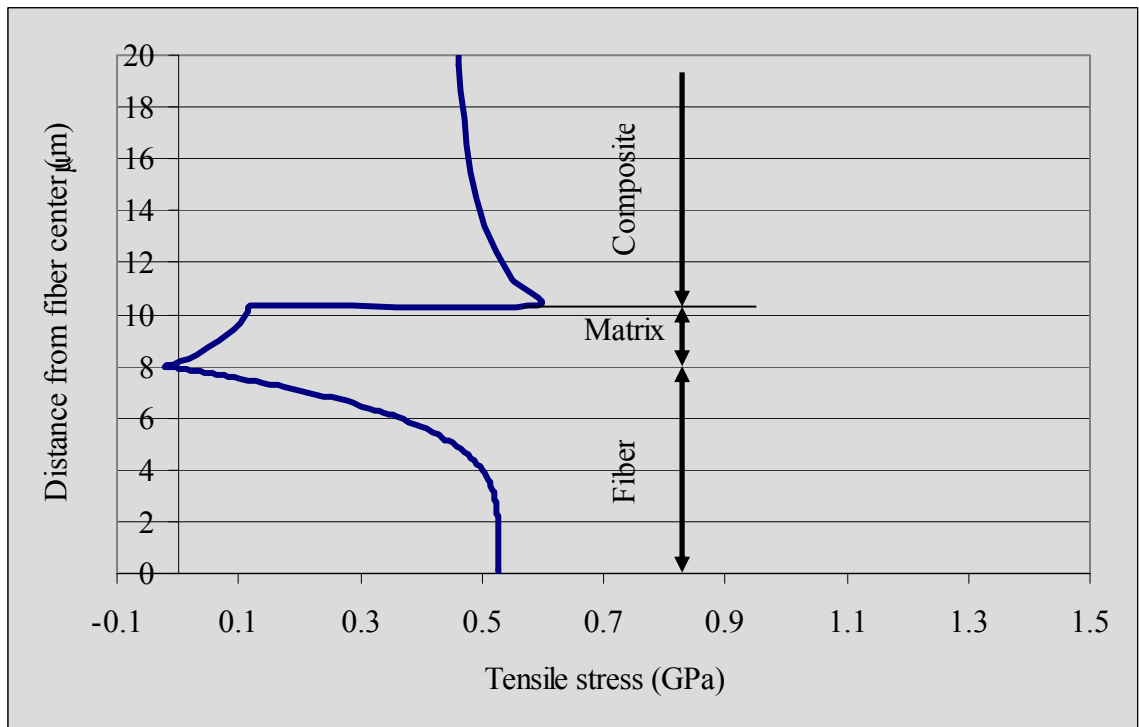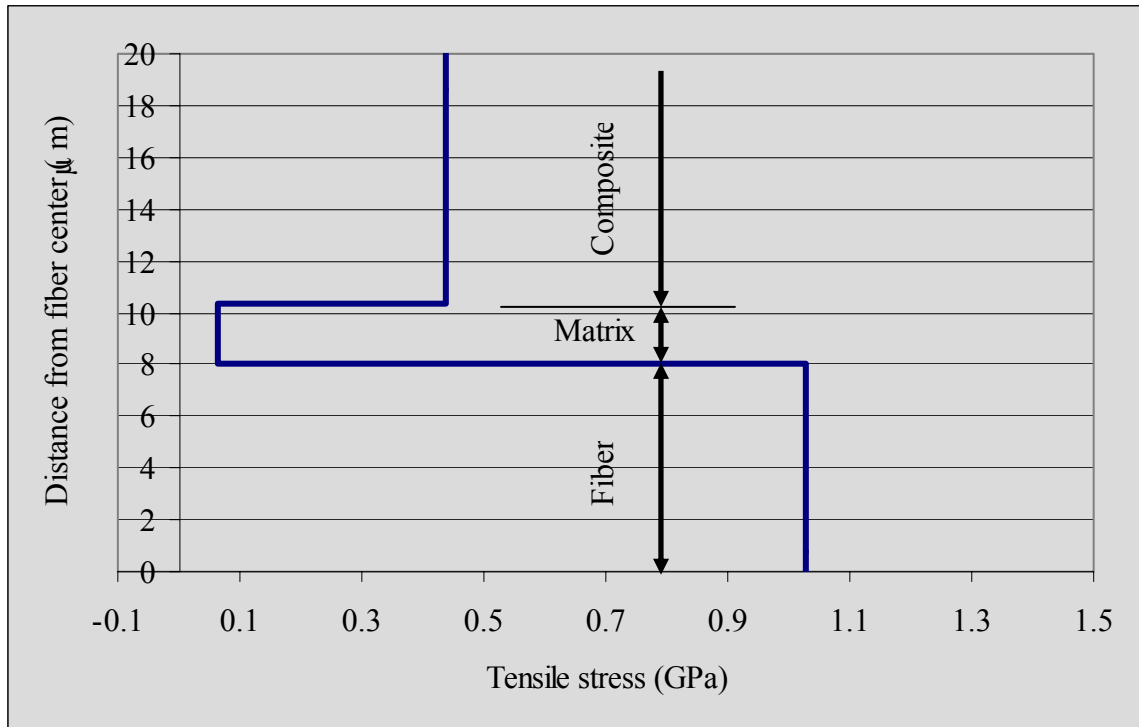
Figure 5-23: Tensile stress distribution in x-direction for longitudinal and transverse

models, for plain/glass fabric with 60% volume fraction

5.3 Comparison of model results to pull-out tests

The difference in the tensile stress at the fiber/matrix interface in the longitudinal fibers, listed in table 5-6, can be used to calculate the interface shear stress between the fiber and matrix using this equation:

$$\tau = \frac{\sigma_{tensile} \cdot r}{2 \cdot l_c}$$

Where: τ is the interface shear stress (MPa) at crack initiation point.

$\sigma_{tensile}$ is the drop of the tensile stress at fiber/matrix interface on the longitudinal fiber (MPa)

r is fiber radius (μm)

l_c is fiber critical length or the fiber length needed for stress build-up at the fiber matrix interface (μm)

The fiber critical length range was taken 150 – 300 (μm) as an accepted length for carbon/epoxy composite [Narin 2001]. All the results are listed in table 5-6 for broken twill/carbon weaves and table 5-7 for the plain/glass weaves. The results for pull-out test were found in literature (DiFrancia 1996) to be between 21 to 39 MPa for the carbon/epoxy composites and 16 to 26 MPa for the glass/epoxy composites. It can be seen from these tables that the interface shear strengths calculated from the model and reported in literature are very close in value.

Table 5-6: Interface shear strength between fiber and matrix for broken twill/carbon weaves

Fiber volume Fraction (%)	Tensile stress difference (MPa)	τ	
		$l_c = 150\ \mu m$	$l_c = 300\ \mu m$
26	4900.7	49.01	24.50
28	3879.5	38.79	19.40
32	4121.9	41.22	20.61
36	3360.4	33.60	16.80
40	3216.6	32.17	16.08

Table 5-7: Interface shear strength between fiber and matrix for plain/glass weaves

Fiber volume Fraction (%)	Tensile stress difference (MPa)	τ	
		150	300
50	1253.9	33.44	16.72
52	1061.4	28.30	14.15
55	971.46	25.91	12.95
58	984.26	26.25	13.12
60	962.48	25.67	12.83

5.4 Stress distribution in the composite

After verifying the proposed models using finite element method, existing analytical models (Weng 1984) and experimental data, these two models can be used with confidence to map the stress within the composite constituents as well as fiber/matrix interface. Radial and hoop stress distribution in the longitudinal model for twill/carbon weave are shown in figures 5-24 and 5-25 and plain/glass weave in figures 5-26 and 5-27, respectively.
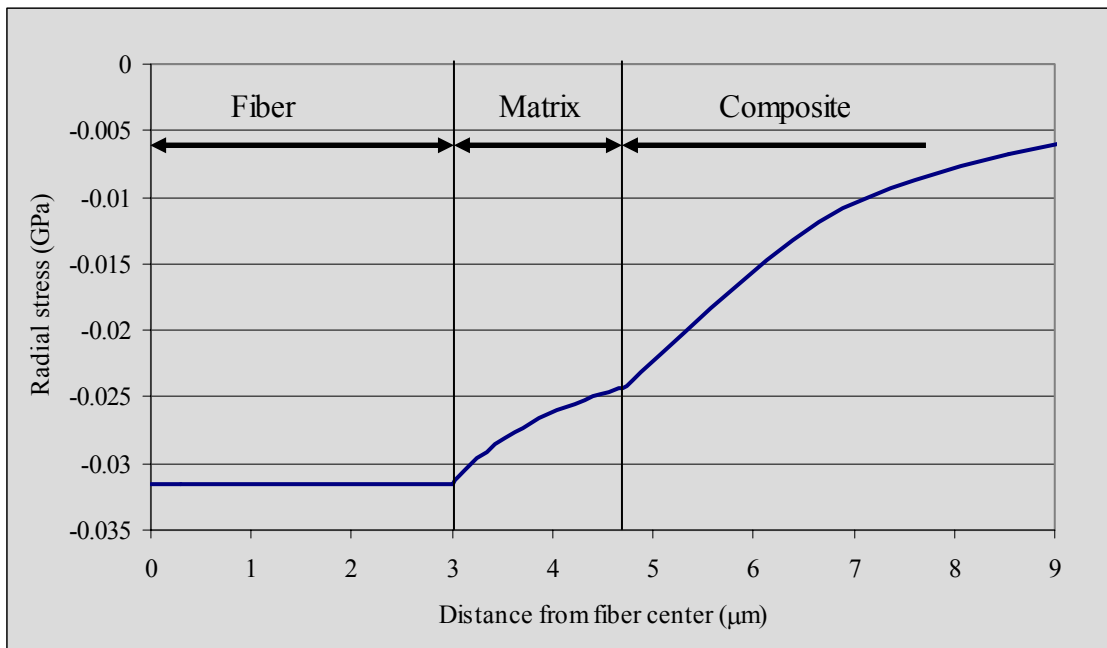
Figure 5-24: Radial stress in fiber, matrix and composite for carbon fabric with 40% fiber volume fraction
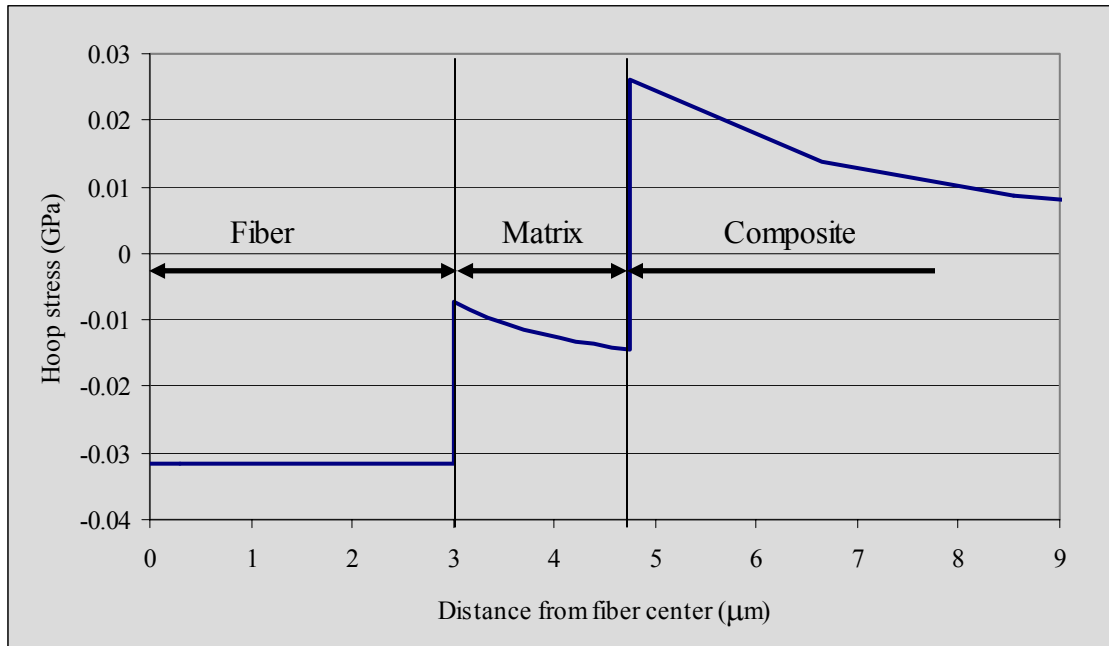
Figure 5-25: Hoop stress in fiber, matrix and composite for carbon fabric with 40% fiber
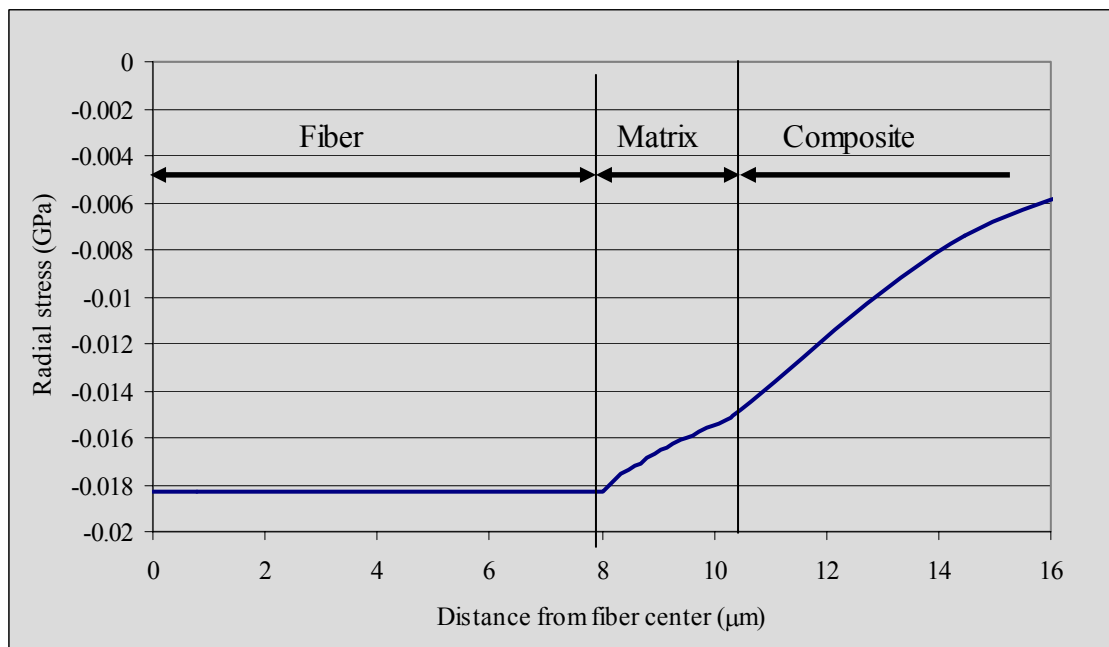
volume fraction

Figure 5-26: Radial stress in fiber, matrix and composite for glass fabric with 60% fiber
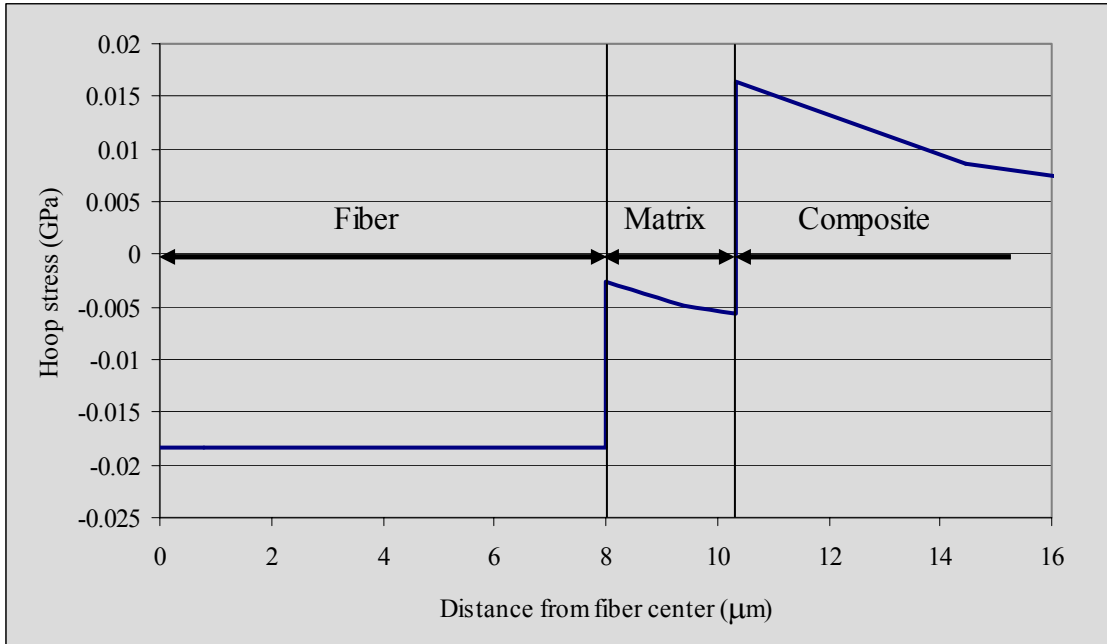
volume fraction

Figure 5-27: Hoop stress in fiber, matrix and composite for glass fabric with 60% fiber

volume fraction

In addition, the stress distribution in the transverse model can be mapped for any angle. Figures 5-28 to 5-30 show the radial, hoop and shear stress distributions for the carbon weave with 40% fiber volume fraction at three different angles, 0, 45 and 90°. Also, in figures 5-31 to 5-33, the stress distributions are shown for glass weave with 60% volume fraction at three different angles.
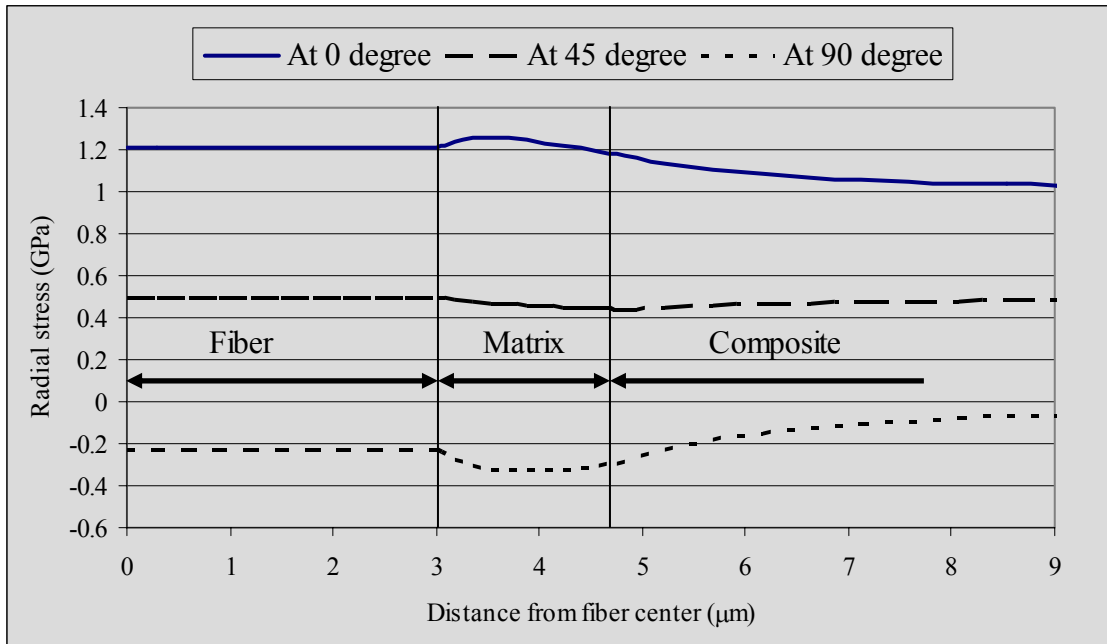
Figure 5-28: Radial stress for twill/carbon weave with 40% fiber volume fraction
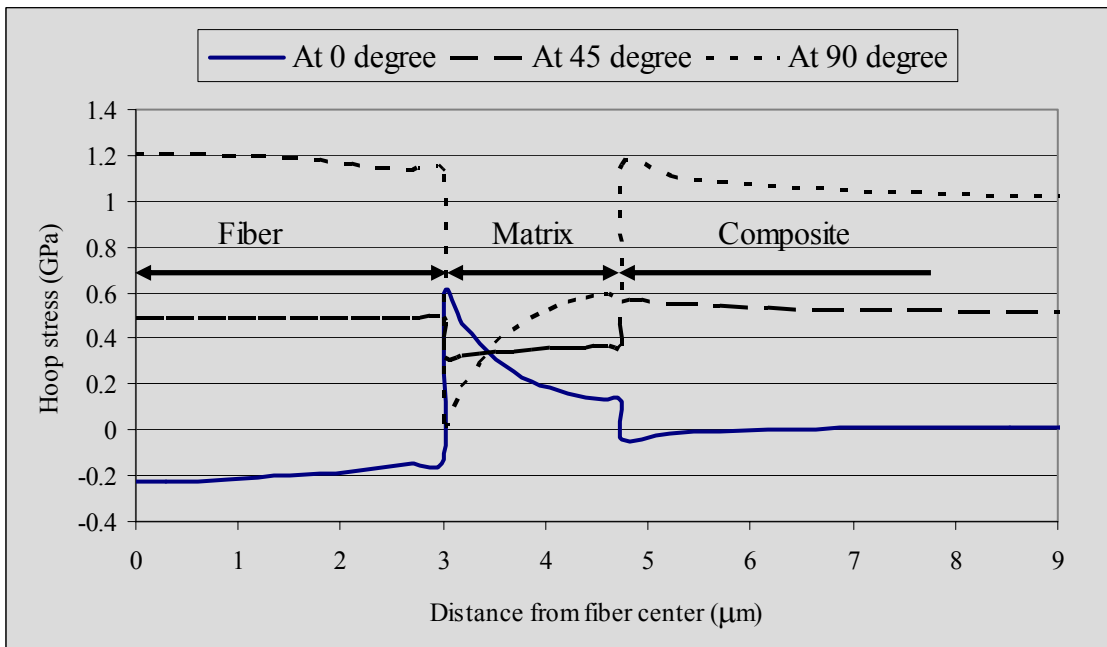
Figure 5-29: Hoop stress for twill/carbon weave with 40% fiber volume fraction
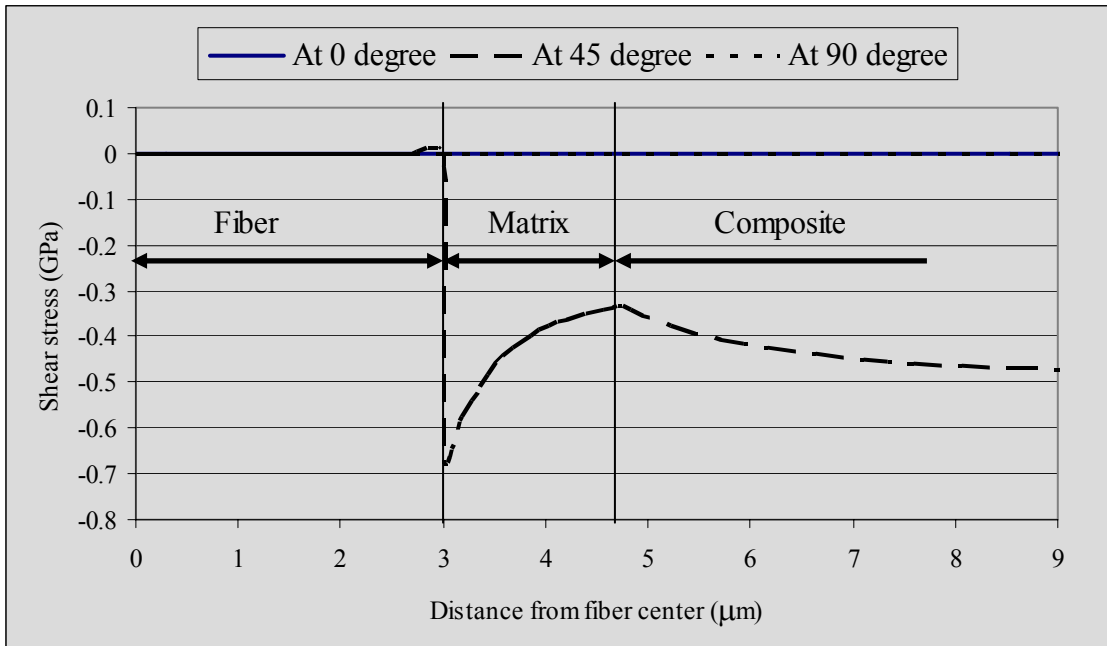
Figure 5-30: Shear stress for twill/carbon weave with 40% fiber volume fraction
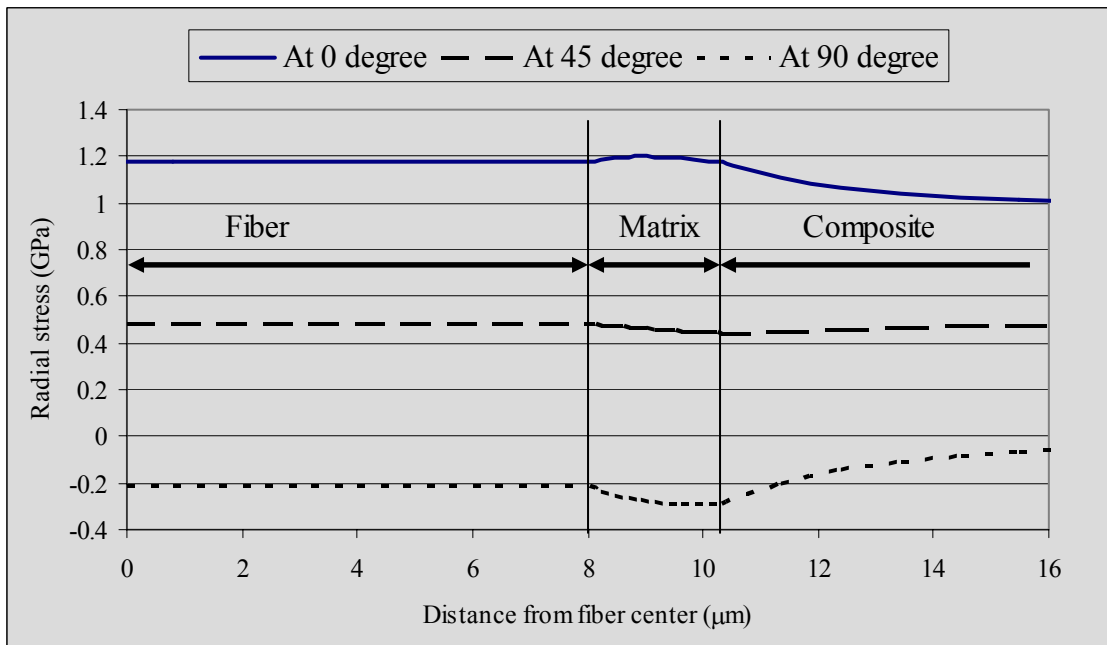
Figure 5-31: Radial stress for plain/glass weave with 60% fiber volume fraction
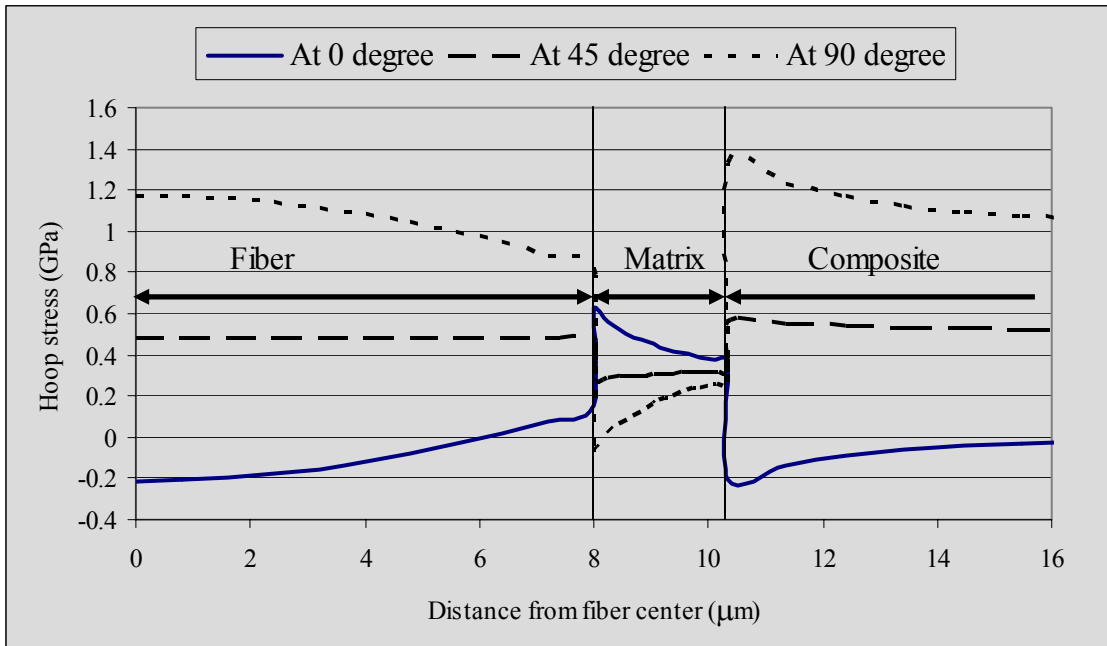
Figure 5-32: Hoop stress for plain/glass weave with 60% fiber volume fraction
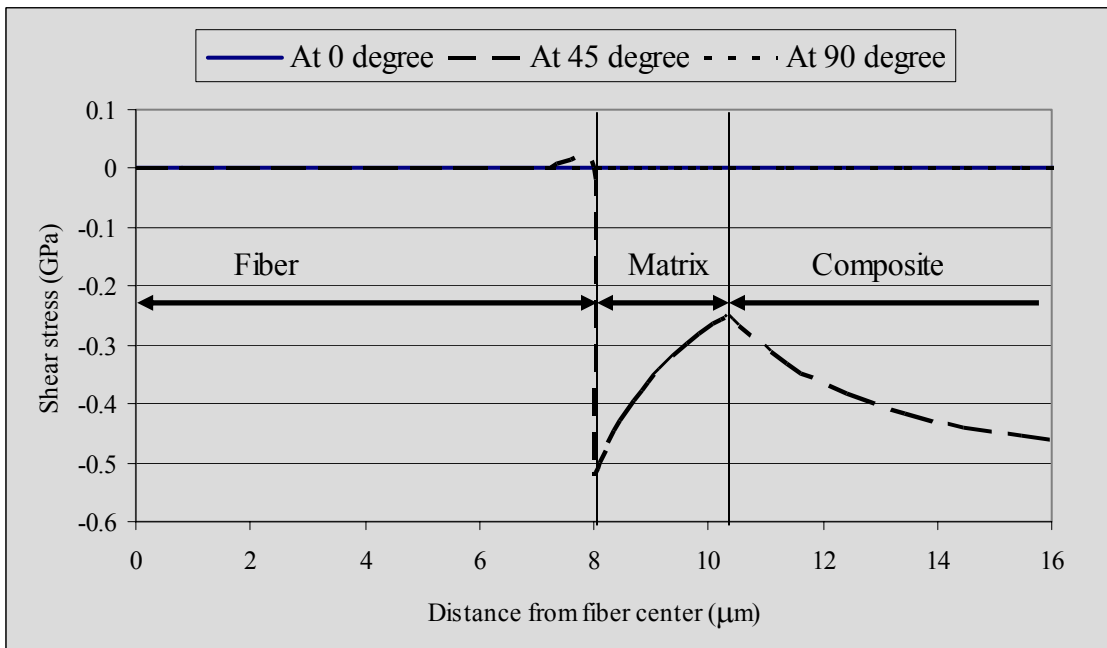
Figure 5-33: Shear stress for plain/glass weave with 60% fiber volume fraction

VI. CONCLUSIONS

6.1 Models

Two analytical models were proposed in this study to map the stress distribution in fiber, matrix and fiber/matrix interface. The first model represented the fiber, matrix and surrounding composite as longitudinal axisymmetric bodies. The second model addressed the fiber in the transverse direction. Polar coordinates were used to set the equations for the stress equilibrium in both models and stress equilibrium and displacement compatibility were used in both models at as the interface boundary conditions. Both models were verified using finite element models (FEMs). In addition, the second model results for stress concentrations were compared to a model from literature and showed good comparison. The effect of neighboring fibers was verified using a superposition technique.

6.2 Experimental work

Experimental work was conducted to verify the two proposed models. An E-glass plain weave and an IM7 carbon broken twill were used to manufacture composite plates. Five panels were produced for each fabric based on the number of fabric layers in each panel.

Five different numbers of fabric layers were used for each panel ranging from 5 to 9 layers. The four-point flexural test was used to test the specimens' shear behavior and stress-strain curves were plotted. A departure from linearity in the stress-strain curves was observed prior to reaching the maximum stress which was accompanied by an audible crack sound. This stress value was considered as the stress causing the initiation of cracks in the specimen.

The tensile stress value at the bottom fabric layer was calculated from the test results. The Graphical Integrated Numerical Analysis model was used to evaluate the average stress distribution at the unit cell level and the maximum stress was used as an input for the proposed micro-models. The stress distributions in the fiber, matrix and fiber/matrix interface were mapped and it was found that the maximum variation in the stresses in the fiber/matrix interface is in the longitudinal direction. The difference in the stresses at the interface was extracted and used to calculate the interfacial shear strength between the fiber and the matrix. The results were compared to literature data and showed good agreement.

6.3 Future work

The only proof for crack initiation is the in the change in linearity in stress-strain curve and the audible sound. So, it is important to monitor the crack initiation using high speed cameras or sensitive sound tools such as "Acoustic Emission". It is believed that

monitoring the crack initiation and progress will clarify many issues and give another dimension for study of textile composites shear behavior.

BIBLOGRAPHY

Abdelrahman, W. G. and Nayfeh, A. H., Micromechanical modeling of stress distribution in undulated composites under axial loading, Mechanics of Materials 30 (1998) 83-90

Akbarov, S. D. and Kosker, R., Stress distribution caused by anti-phase periodical curving of two neighbouring fibers in a composite material, European Journal of Mechanics A/Solids 22 (2003) 243–256

Bahei-El-Din, Y.A., Rajendran, A.M. and Zikry M.A., A micromechanical model for damage progression in woven composite systems, International Journal of Solids an1d Structures 41 (2004) 2307–2330

Barbero, E.J., Damiani, T.M. and Trovillion, J., Micromechanics of fabric reinforced composites with periodic microstructure, International Journal of Solids and Structures 42 (2005) 2489–2504

Benedikt, B., Rupnowski, P. and Kumosa, M., Visco-elastic stress distributions and elastic properties in unidirectional composites with large volume fractions of fibers, Acta Materialia 51 (2003) 3483–3493

Blackketter, D., Walrath, D. & Hansen, A., Modeling damage in a plain weave fabric-reinforced composite material. J. Camp. Technol. Res., 15 (1993) 136-42.

Cheng, J., Jordan E.H. and Walker K.P., A simple accurate method for calculating local stresses around individual fibers in periodic composites, Composites: Part B 30 (1999) 453–463 – a

Cheng, J., Jordan E.H. and Walker K.P., Closed form solution for rectangular inclusions with quadratic eigenstrains, International J. of Engineering Science 37 (1999) 1261-1276 – b

Cheng, J., Jordan, E.H. and Walker, K. P., A higher order subdomain method for finding local stress fields in composites, Int. J. Solids Structures Vol. 35, No. 36, pp. 5189 5203, 1998

Christensen R. M., A critical evaluation for a class of micromechanics models, J. Mech. Phys. Solids 1990; 38: 379–404.

DiFrancia, C. And Ward, T.C., The single-fiber pull-out test. 1: Review and interpretation, Composite Part A, 27A, 1996, pp. 597-612

Eshelby, J. D., The determination of the elastic field of an ellipsoidal inclusion and related problems. Proc. R. Soc. Land. Series A 241, (1957), 376-396.

J.D. Eshelby, Proc. R. Soc. London, Ser. A 252 (1959) 561.

Foye, R.L. in Fiber Tex '90' (Ed. J. Buckley), NASA Langley Research Center, Hampton, VA, May 1992, pp. 45-53

Gowayed, Y. and Pastore, C. and Howarth, C.S, Modification and application of a unit cell continuum model to predict the elastic properties of textile composites, Composites: Part A 27A (1996) 149-155

Gowayed, Y. and Pastore, C., Analytical techniques for the prediction of elastic properties of textile reinforced composites, Mechanics of Composite Materials, Vol. 5, pp. 579-596, 1992.

Hahn, H. T. & Pandy, R., A micromechanics model for thermoelastic properties of plain weave fabric composites. J. Engng Mater. Technol., 116 (1994) 517-523.

Hashin, Z., 1991. Thermoelastic properties of particulate composites with imperfect interface. J. Mech. Phys. Solids 39, 745-762.

Hirai, I., Uchiyama, T., Mizuta, Y. and Pilkey, W., An efficient zooming method for finite element analysis. Int. J. for Numerical Methods in Engineering, 20, (1984), 1627-1683.

Hirai, I., Uchiyama, T., Mizuta, Y. and Pilkey, W., An efficient zooming method for finite element analysis. International Journal for Numerical Methods in Engineering 1984,20,1627-1683

Honein, E. , Honein, T. and Herrmann, G., Energetics of two circular inclusions in anti-plane elastostatics, International Journal of Solids and Structures 37 (2000) 3667-3679

Honein, E., Honein, T., Herrmann, G., Further aspects of the elastic field for two circular inclusions in anti-plane elastostatics. Journal of Applied Mechanics 59, 1992, 774-779. b

Honein, E., Honein, T., Herrmann, G., On two circular inclusions in harmonic problems. Quarterly of Applied Mathematics L (3), 1992, 479-499. a

Horii, H. and Nemat-Nasser, S., Elastic fields of interacting inhomogeneities, Int. J. Solids Structures, Vol. 21, No. 7, pp. 731-745, 1985

Hutapea, P., Yuan, F.G. and Pagano, N. J., Micro-stress prediction in composite laminates with high stress gradients, Int. J. of Solids and Structures 40 (2003) 2215–2248

Ishikawa, T. and Chou, T.W., Stiffness and strength behaviour of woven fabric composites. . J. Mater. Sci., 17 (1982) 3211-3220.

Ito, M and Chou, T.-W., Elastic moduli and stress field of plain-weave composites under tensile loading, Composites Science and Technology, 57 (7), (1997), 787-800

Ito, M and Chou, T.-W., Analytical and experimental study of strength and failure behavior of plain-weave composites, J. Composite Materials, 32 (1), (1998), 2-30

Jara-Almonte, C. C. and Knight, C. E., The specified boundary stiffness/force SBSF method for finite element subregion analysis. International Journal for Numerical Methods in Engineeting 1988, 26, 1567-1578.

Jiang, Z., Liu, X., Li, G. and Lian, J., A new analytical model for three-dimensional elastic stress field distribution in short fiber composite, Materials Science and Engineering A366 (2004) 381–396

Jortner, J., Effects of crimp angle on the tensile strength of a carbon-carbon laminate, Symp. on High Temperature Composites, Proc. Amer. Soc. Composites, Technomic Publ. Co.: Lancaster, PA, (1989), 243-251

Kedward, K.T, On the short beam test method, Fiber Science and Technology (5) (1972), pp. 85-95

Kikuchi, N. and Guedes, J. M., Preprocessing and postprocessing for materials based on the homogenization method with adaptive finite element methods. Computer Method in Applied Mechanics and Engineering 1990,83,143-198.

Ko, F. K. and Chou, T. W., Composite Materials Series 3-Textile Structural Composites. Elsevier Science, Amsterdam, 1989.

Le Page, B.H., Guild, F.J., Ogin, S.L. and Smith P.A., Finite element simulation of woven fabric composites, Composites: Part A 35 (2004) 861–872

Li, M., Matsuyama, R. and Sakai, M., Interlaminar shear strength of C/ C-composites: the dependence on test methods, Carbon 37 (1999) 1749–1757

Luo, J. and Sun, C. T., Global-local methods for thermoelastic stress analysis of thick fiber-wound cylinders. Journal of Composite Materials 1991, 25, 453-468.

Meguid, S.A. and Zhu, Z.H., Stress distribution in dissimilar materials containing inhomogeneities near the interface using a novel finite element, Finite Elements in Analysis and Design 20 (1995) 283-298

Morena, J.J., Advanced Composites World Reference Dictionary, Krieger Publishing Company: Malabar, FL, 1997

Molinari, A. And El Mouden M., The problem of elastic inclusions at finite concentration, Int. J. Solids Structures Vol. 33, No. 2S22, (1996), 3131-3150

Morais, A. B., Stress distribution along broken fibers in polymer-matrix composites, Composites Science and Technology, 61, (2001) 1571-1580

Mori, T., Tanaka, K., Average stress in matrix and average elastic energy of materials with misfitting inclusion. Acta Metall. (1973) 571-580.

Naik, N. K. & Ganesh, V. K., An analytical method for plain weave fabric composites. Composites, 264 (1995) 281-289.

Naik, N. K. & Shembekar, P. S., Elastic behavior of woven fabric composites: I. Lamina analysis. .J. Comp. Mater., 2615 (1992) 2196-2225.

Nairn, J.A, Liu, Chun-Hsin, Mendels, D.A. and Zhandarov, S., Fracture mechanics analysis of the single-fiber pull-out test and the microbond test including the effects of friction and thermal stresses, Proc. 16-th Ann. Tech. Conf. of the Amer. Soc. Composites, VPI, Blacksburg VA, September 9-12, 2001.

Nayfeh, A.H., Abdelrahman, W.G., Micromechanical modeling of load transfer in fibrous composites. Mechanics of Materials, Volume 30, Issue 4, December 1998, 307-324

Nettles, A.T., Composite processing development to improve interlaminar strength using ply interface particles, (Center director's discretionary fund final report No. 93-13), NASA, Marshall Space Flight Center, MSFC, Alabama, June 1995.

Paris, F., Correa, E. and Canas, J., Micromechanical view of failure of the matrix in fibrous composite materials, Composites Science and Technology 63 (2003) 1041–1052

Pastore, C. M. and Gowayed, Y. A., A self-consistent fabric geometry model: Modification and application of a fabric geometry model to predict the elastic properties of textile composites, Journal of Composites Technology and Research, JCTRER, Vol. 16, No. 1, January 1994, pp. 32-36.

Pastore, M.E., Bogdanovich, A.E. and Gowayed Y.A., Application of a meso-volume-based analysis for textile composite structures, Composites Engineering, Vol. 3, No. 2, pp. 181-194, 1993

Rossoll, A., Moser, B. and Mortensen, A., Longitudinal deformation of fibre reinforced metals: influence of fibre distribution on stiffness and flow stress, Mechanics of Materials 37 (2005) 1–17

Savin, G. N., Stress concentration around holes, Pergamon Press, Inc., 1961

Shembekar, P. S. & Naik, N. K., Elastic behavior of woven fabric composites: II. Laminate analysis. J. Comp. Mater., 2615 (1992) 2226-2246.

Short, S.R., Characterization of interlaminar shear failures of graphite/epoxy composite materials, Composites, Vo. 26, No. 6, 1995, pp. 431-449

Srirengan, K., Whitcomb, J. and Chapman, C, Modal technique for three-dimensional global/local stress analysis of plain weave composites, Composite Structures Vol. 39, No. 12, pp. 145-156, 1997

Tandon, G. P. and Weng, G.J., Stress distribution in and around spheroidal inclusions and voids at finite concentration, Journal of Applied Mechanics, Vol. 63, 1986, 511-518

Vaidyanathan, R. and Gowayed, Y.A., Optimization of elastic properties in the design of textile composites, Polymer Composites, Vol. 17, No. 2, pp. 305-311,1996.

Vandeurzen,Ph., Ivens, J. and Verpoest, I., A three-dimensional micromechanical analysis of woven-fabric composites: I. Geometric analysis, Composites Science and Technology 56 (1996) 1303-1315

Weng, G. J., Some elastic properties of reinforced solids with special reference to isotropic ones containing spherical inclusions, Int. J. Engng. Sci., Vol. 22, No. 7, 1984, 845-856

Whitcomb, J. D. and Woo, K., Enhanced direct stiffness method for finite element analysis of textile composites. Composite Structures 1994, 28, 385-390.

Whitcomb, J., Srirengan, K. and Chapman, C., Evaluation of homogenization for global/local stress analysis of textile composites, Composite Structures 31 (1995) 137- 149

Whitcomh, J. and Srirengan, K., Effect of various approximations on predicted progressive failure in plain weave composites, Composite Structures 34 (1996) 13-20

Whitney, J.M., Experimental characterization of delamination fracture, Interlaminar response of composite materials, Composite materials series Vol. 5, 1989, Editor: N. J. Pagano, Series editor: R. B. Pipes

Wisnom, M.R and Jones, M.I, Delamination due to interaction between overall interlaminar shear and stresses at terminating plies, Composite Structures 31(1995) 39-47

Wisnom, M.R, Modeling the effect of cracks on interlaminar shear strength, Composites Part A 27A (1996) 11-24

Woo, K. and Whitcomb, J. D., Macro finite element using subdomain integration, Communications of Numerical Methods in Engineeting 1993 ,9 ,937-949.

Yongli Wu, Zhong Ling, Zhifa Dong, Stress-strain fields and the effectiveness shear properties for three-phase composites with imperfect interface, International Journal of Solids and Structures 37 (1999) 1275-1292

Zeller. R. and Dederichs, P. H. (1973). Elastic constant of polycrystals. Phys. Status Solid B 55, 831-842.

APPENDICES

APPENDIX A: MATLAB® CODE FOR THE LONGITUDINAL MODEL

```
clear;
P=0.4469e3;
Vf=0.60;

% Fiber Properties
rf=8e-3;
Ef=72.4e3;
Gf=28.96e3;
nuf=0.25;

% Matrix Properties
rm=sqrt(rf^2 /Vf);
Em=5e3;
num=0.35;
Gm=Em/(2*(1+num));

% Composite Properties

rfm=5*rm;
Efm=4.443177*6.895e3;
nufm=0.370096;
Gfm=0.910532*6.895e3;

%%%%%%%%%%%%%%%%%%%%%%%% Symbolic  %%%%%%%%%%%%%%%%%%%%%
syms K Mm Nm Mfm Nfm Szf Szm Szfm r

% Fiber Equations
Srf=K;
Scf=K;
ecf=(Scf-(nuf*Srf)-(nuf*Szf))/Ef;
ezf=(Szf-(nuf*Scf)-(nuf*Srf))/Ef;
%Sz1=Szf-(nuf*Scf)-(nuf*Srf)-(Ef*epz);
urf=r*ecf;

% Matrix Equations
Srm=Mm+(Nm/r^2);
Scm=Mm-(Nm/r^2);
```

```
ecm=(Scm-(num*Srm)-(num*Szm))/Em;
ezm=(Szm-(num*Scm)-(num*Srm))/Em;
%Sz2=Szc-(nuc*Scc)-(nuc*Src)-(Ec*epz);
urm=r*ecm;

% Composite Equations
Srfm=Mfm+(Nfm/r^2);
Scfm=Mfm-(Nfm/r^2);
ecfm=(Scfm-(nufm*Srfm)-(nufm*Szfm))/Efm;
ezfm=(Szfm-(nufm*Scfm)-(nufm*Srfm))/Efm;
%Sz3=Szm-(num*Scm)-(num*Srm)-(Em*epz);
urfm=r*ecfm;
Sz4=(Szf*(rf^2))+(Szm*((rm^2)-(rf^2)))+(Szfm*((rfm^2)-(rm^2)))-(P*(rfm^2));
% At r = rf ----> Srf = Src  && Urf = Urc
r=rf;
Sr1=subs(Srf-Srm);
Ur1=subs(ecf-ecm);
Szfmm=subs(ezm-ezf);

% At r = rm ----> Srm = Srfm  && Urm = Urfm
r=rm;
Sr2=subs(Srm-Srfm);
Ur2=subs(ecm-ecfm);
Szme=subs(ezfm-ezm);

% At r = rfm ----> Srfm = 0
r=rfm;
Sr3=subs(Srfm);
Sz4=subs(Sz4);

GG=solve(Sr1,Ur1,Sr2,Ur2,Sr3,Szfmm,Szme,Sz4);
K=subs(GG.K);
Mm=subs(GG.Mm);
Nm=subs(GG.Nm);
Mfm=subs(GG.Mfm);
Nfm=subs(GG.Nfm);
Szf=subs(GG.Szf);
Szm=subs(GG.Szm);
Szfm=subs(GG.Szfm);

jj=0;
for r=0:rf/10:rf
    jj=jj+1;
    rr(jj)=r;
    Ur(jj)=subs(urf);
```

```
    Sr(jj)=subs(Srf);
    Sc(jj)=subs(Scf);
    Sz(jj)=subs(Szf);

end

for r=rf:(rm-rf)/10:rm
    jj=jj+1;
    rr(jj)=r;
    Ur(jj)=subs(urm);
    Sr(jj)=subs(Srm);
    Sc(jj)=subs(Scm);
    Sz(jj)=subs(Szm);

end


for r=rm:(rfm-rm)/10:rfm
    jj=jj+1;
    rr(jj)=r;
    Ur(jj)=subs(urfm);
    Sr(jj)=subs(Srfm);
    Sc(jj)=subs(Scfm);
    Sz(jj)=subs(Szfm);

end



figure, plot(Sz/1e3,rr);
ylabel('Radius R (mm)');
xlabel('Axial Stress (GPa)');
```

APPENDIX B: MATLAB® CODE FOR THE TRANSVERSE MODEL

```
% Stresses as out boundary conditions
clear;
P=0.4469e3;
Vf=0.60;


% Fiber Properties
rf=8e-3;
Ef=72.4e3;
Gf=28.96e3;
nuf=0.25;
zf=3-(4*nuf);

% Matrix Properties
rm=sqrt(rf^2 /Vf);
Em=5e3;
num=0.35;
Gm=Em/(2*(1+num));
zm=3-(4*num);


Efm=4.443177*6.895e3;
nufm=0.370096;
Gfm=0.910532*6.895e3;
zfm=3-(4*nufm);

% ( 1 )  At r = rf Sr = Sr for the constant part
S(1,1)=0.5;
S(1,2)=0;
S(1,3)=0;

S(1,4)=-0.5;
S(1,5)=0.25*(rm/rf)^2;
S(1,6)=0;
S(1,7)=0;
S(1,8)=0;
S(1,9)=0;
```

```
S(1,10)=0;
S(1,11)=0;
S(1,12)=0;


% ( 2 )  At r = rf Sr = Sr
S(2,1)=0;
S(2,2)=0.25;
S(2,3)=0;

S(2,4)=0;
S(2,5)=0;
S(2,6)=-0.25;
S(2,7)=(rm/rf)^2;
S(2,8)=0.75*(rm/rf)^4;
S(2,9)=0;

S(2,10)=0;
S(2,11)=0;
S(2,12)=0;


% ( 3 )  At r = rf Trcf = Trcm
S(3,1)=0;
S(3,2)=-0.25;
S(3,3)=1.5*(rf/rm)^2;

S(3,4)=0;
S(3,5)=0;
S(3,6)=0.25;
S(3,7)=0.5*(rm/rf)^2;
S(3,8)=0.75*(rm/rf)^4;
S(3,9)=-1.5*(rf/rm)^2;

S(3,10)=0;
S(3,11)=0;
S(3,12)=0;


% ( 4 )  At r = rf Urf = Urm for the constant part 1
S(4,1)=(zf-1)*(rf/rm);
S(4,2)=0;
S(4,3)=0;
```

```
S(4,4)=-(Gf/Gm)*(zm-1)*(rf/rm);
S(4,5)=-(Gf/Gm)*(rm/rf);
S(4,6)=0;
S(4,7)=0;
S(4,8)=0;
S(4,9)=0;

S(4,10)=0;
S(4,11)=0;
S(4,12)=0;

% ( 5 )  At r = rf Urf = Urm for part 2
S(5,1)=0;
S(5,2)=(rf/rm);
S(5,3)=(zf-3)*(rf/rm)^3;

S(5,4)=0;
S(5,5)=0;
S(5,6)=-(Gf/Gm)*(rf/rm);
S(5,7)=-(Gf/Gm)*(zm+1)*(rm/rf);
S(5,8)=-(Gf/Gm)*(rm/rf)^3;
S(5,9)=-(Gf/Gm)*(zm-3)*(rf/rm)^3;

S(5,10)=0;
S(5,11)=0;
S(5,12)=0;


% ( 6 )  At r = rf Ucf = Ucm
S(6,1)=0;
S(6,2)=-(rf/rm);
S(6,3)=(zf+3)*(rf/rm)^3;

S(6,4)=0;
S(6,5)=0;
S(6,6)=(Gf/Gm)*(rf/rm);
S(6,7)=(Gf/Gm)*(zm-1)*(rm/rf);
S(6,8)=-(Gf/Gm)*(rm/rf)^3;
S(6,9)=-(Gf/Gm)*(zm+3)*(rf/rm)^3;

S(6,10)=0;
S(6,11)=0;
S(6,12)=0;
```

```
% ( 7 )  At r = rm Sr = Sr for PART 1
S(7,1)=0;
S(7,2)=0;
S(7,3)=0;

S(7,4)=0.5;
S(7,5)=-0.25;
S(7,6)=0;
S(7,7)=0;
S(7,8)=0;
S(7,9)=0;

S(7,10)=0.25;
S(7,11)=0;
S(7,12)=0;


% ( 8 )  At r = rm Sr = Sr for PART 2
S(8,1)=0;
S(8,2)=0;
S(8,3)=0;

S(8,4)=0;
S(8,5)=0;
S(8,6)=0.25;
S(8,7)=-1;
S(8,8)=-0.75;
S(8,9)=0;

S(8,10)=0;
S(8,11)=1;
S(8,12)=0.75;


% ( 9 )  At r = rm Trm = Tre
S(9,1)=0;
S(9,2)=0;
S(9,3)=0;

S(9,4)=0;
S(9,5)=0;
S(9,6)=-0.25;
S(9,7)=-0.5;
S(9,8)=-0.75;
S(9,9)=1.5;
```

```matlab
S(9,10)=0;
S(9,11)=0.5;
S(9,12)=0.75;


% ( 10 )  At r = rm Urm = Ure for PART 1
S(10,1)=0;
S(10,2)=0;
S(10,3)=0;

S(10,4)=(zm-1);
S(10,5)=1;
S(10,6)=0;
S(10,7)=0;
S(10,8)=0;
S(10,9)=0;

S(10,10)=-(Gm/Gfm);
S(10,11)=0;
S(10,12)=0;

% ( 11 )  At r = rm Urm = Ure for PART 2
S(11,1)=0;
S(11,2)=0;
S(11,3)=0;

S(11,4)=0;
S(11,5)=0;
S(11,6)=1;
S(11,7)=(zm+1);
S(11,8)=1;
S(11,9)=(zm-3);

S(11,10)=0;
S(11,11)=-(Gm/Gfm)*(zfm+1);
S(11,12)=-(Gm/Gfm);

% ( 12 )  At r = rm Ucm = Uce
S(12,1)=0;
S(12,2)=0;
S(12,3)=0;

S(12,4)=0;
S(12,5)=0;
```

```
S(12,6)=-1;
S(12,7)=-(zm-1);
S(12,8)=1;
S(12,9)=(zm+3);

S(12,10)=0;
S(12,11)=(Gm/Gfm)*(zfm-1);
S(12,12)=-(Gm/Gfm);




C(1)=0;
C(2)=0;
C(3)=0;
C(4)=0;
C(5)=0;
C(6)=0;
C(7)=0.5;
C(8)=0.5;
C(9)=-0.5;
C(10)=(Gm/Gfm)*(zfm-1);
C(11)=2*(Gm/Gfm);
C(12)=-2*(Gm/Gfm);

Co=inv(S)*C';
Af=Co(1);
Bf=Co(2);
Cf=Co(3);
AA=Co(4);
BB=Co(5);
CC=Co(6);
DD=Co(7);
EE=Co(8);
FF=Co(9);
Ae=Co(10);
Be=Co(11);
Ce=Co(12);

%Co'

r=rf;
j=0;
for theta = -90:1:90
    j=j+1;
```

```
    c=theta*pi/180;
    Q=cos(2*c);

    Scm(j)=0.5*((AA+((BB/2)*(rm/r)^2)) - (((CC/2)-(1.5*EE*(rm/r)^4)-
(6*FF*(r/rm)^2))*cos(2*c)));

    Srf(j)=0.5*(Af + ((Bf/2)*cos(2*c)));
    Scf(j)=0.5*(Af - (((Bf/2)-(6*Cf*(r/rm)^2))*cos(2*c)));
    Trc(j)=0.5*((-Bf/2)+(3*Cf*(r/rm)^2))*sin(2*c);
    Ur(j)=((Af*(zf-1)*(r/rm))+ (((Bf*(r/rm))+(Cf*(zf-
3)*(r/rm)^3))*cos(2*c)))*rm/(8*Gf);
    Uc(j)=((-Bf*(r/rm))+(Cf*(zf+3)*(r/rm)^3))*(rm/(8*Gf))*sin(2*c);

    Sxf(j)=P*1e-3*((Srf(j)*(cos(c))^2)+(Scf(j)*(sin(c))^2)-(2*Trc(j)*(sin(c)*cos(c))));
    Sxc(j)=P*1e-3*((Srf(j)*(cos(c))^2)+(Scm(j)*(sin(c))^2)-(2*Trc(j)*(sin(c)*cos(c))));

    cc(j)=theta;

end
hold on
plot(Sxf,cc,'r');
plot(Sxc,cc,'m');
xlabel('Stress in x-direction around the fiber(GPa)');
ylabel('Angle (deg)');

%plot(Sxc-Sxf,cc,'k');

grid on
```

APPENDIX C: GENERAL SOLUTION TO A BI-HARMONIC EQUATION

"KOLOSOV MUKHELISHVILI COMPLEX POTENTIAL"

The stress function $U(x,y)$ can be expressed in terms of two separate analytical functions. A function $f(z)$ is said to be analytic at appoint $z = z_o$ if it is defined at that point and has derivatives in the neighborhood of $z = z_o$. So, $f(z)$ is said to be analytic over a region R if it is analytic at all points in R. Also, $f(z)$ can be expressed as a power series centered around $z = z_o$.

$$f(z) = \sum_{n=-\infty}^{\infty} b_n (z - z_o)^n$$

$$z = x + iy$$

$$\frac{\partial f(z)}{\partial x} = \frac{\partial f(z)}{\partial z} \cdot \frac{\partial z}{\partial x} = \frac{\partial f(z)}{\partial z} = f'(z)$$

$$\frac{\partial f(z)}{\partial y} = \frac{\partial f(z)}{\partial z} \cdot \frac{\partial z}{\partial y} = i\frac{\partial f(z)}{\partial z} = if'(z)$$

Let $f(z)=P(x,y) + iQ(x,y) = P + iQ$

$$\frac{\partial f(z)}{\partial x} = f'(z) = \frac{\partial P}{\partial x} + i\frac{\partial Q}{\partial x}$$

$$\frac{\partial f(z)}{\partial y} = if'(z) = \frac{\partial P}{\partial y} + i\frac{\partial Q}{\partial y}$$

$$i \cdot \left(\frac{\partial P}{\partial x} + i\frac{\partial Q}{\partial x}\right) = \frac{\partial P}{\partial y} + i\frac{\partial Q}{\partial y}$$

$$-\frac{\partial Q}{\partial x} + i\frac{\partial P}{\partial x} = \frac{\partial P}{\partial y} + i\frac{\partial Q}{\partial y}$$

$Real \equiv Real$ & $Im \equiv Im$

$$\frac{\partial P}{\partial x} = \frac{\partial Q}{\partial y} \quad \& \quad \frac{\partial P}{\partial y} = -\frac{\partial Q}{\partial x} \qquad (Cauchy\,Re\,iman\ equation\ or\ C.R\ eq.)$$

Consider $\nabla^2 P$

$$\nabla^2 = \frac{\partial^2}{\partial x^2} + \frac{\partial^2}{\partial y^2}$$

$$\nabla^2 = \frac{\partial^2}{\partial r^2} + \frac{1}{r}\frac{\partial}{\partial r} + \frac{1}{r^2}\frac{\partial^2}{\partial \theta^2} \quad (Polar)$$

$$\nabla^2 P = \frac{\partial^2 P}{\partial x^2} + \frac{\partial^2 P}{\partial y^2}$$

$From\,C.R.Equ.$

$$\nabla^2 P = \frac{\partial^2 Q}{\partial x \partial y} - \frac{\partial^2 Q}{\partial x \partial y} = 0 \Rightarrow P\ is\ harmonic$$

Airy's stress function (NO BODY FORCE)

For 2-D it is possible to find a function *U(x,y)* such that:

i) It satisfies stress equilibrium equations.

ii) It satisfies compatibility condition.

iii) It satisfies boundary conditions.

Let $U(x,y)$ be chosen such that.

$$\sigma_{11} = \frac{\partial^2 U}{\partial y^2} \; , \quad \sigma_{22} = \frac{\partial^2 U}{\partial x^2} \quad and \quad \tau_{12} = -\frac{\partial^2 U}{\partial x \partial y}$$

In polar:

$$\sigma_{rr} = \frac{1}{r} \cdot \frac{\partial U}{\partial r} + \frac{1}{r^2} \cdot \frac{\partial^2 U}{\partial \theta^2} \qquad (Radial)$$

$$\sigma_{\theta\theta} = \frac{\partial^2 U}{\partial r^2} \qquad (Hoop)$$

$$\tau_{r\theta} = \frac{1}{r^2} \cdot \frac{\partial U}{\partial \theta} - \frac{1}{r} \cdot \frac{\partial^2 U}{\partial r \partial \theta} \qquad (Shear)$$

Strain compatibility equation in 2-D:

$$\frac{\partial^2 \varepsilon_{11}}{\partial y^2} + \frac{\partial^2 \varepsilon_{22}}{\partial x^2} = 2 \cdot \frac{\partial^2 \varepsilon_{12}}{\partial x \partial y}$$

Using the stress-strain relations:

$$\varepsilon_{11} = \frac{\sigma_{11}}{E} - \frac{\upsilon}{E}\sigma_{22}$$

$$\varepsilon_{22} = \frac{\sigma_{22}}{E} - \frac{\upsilon}{E}\sigma_{11}$$

$$\varepsilon_{12} = \frac{\sigma_{12}}{2G}$$

We can get:

$$\frac{\partial^4 U}{\partial x^4} + 2\frac{\partial^4 U}{\partial x^2 \partial y^2} + \frac{\partial^4 U}{\partial y^4} = 0$$

$$i.e\ \nabla^2\left(\nabla^2 U\right) = 0 \quad \Rightarrow Bi-harmonic\ Equation$$

$$\nabla^2 U = \sigma_{11} + \sigma_{22}$$

$$\nabla^2\left(\sigma_{11} + \sigma_{22}\right) = 0$$

$$\therefore \left(\sigma_{11} + \sigma_{22}\right) is\ harmonic$$

Let $P = \sigma_{11} + \sigma_{22}$

Let us introduce a function $\phi(z)$

$$\phi(z) = \frac{1}{4}\int f(z)\,dz$$

$$= \frac{1}{4}\int (P + iQ)\,dz = p + iq$$

$$\phi'(z) = \frac{\partial \phi}{\partial z} = \frac{1}{4}\cdot f(z) = \frac{1}{4}(P + iQ) = \frac{\partial p}{\partial x} + i\cdot\frac{\partial q}{\partial x}$$

$$\therefore \frac{\partial p}{\partial x} = \frac{1}{4}P \quad , \quad \frac{\partial q}{\partial x} = \frac{1}{4}Q$$

Using C.R. equation:

$$\frac{\partial p}{\partial x} = \frac{\partial q}{\partial y} = \frac{P}{4} \quad , \quad \frac{\partial p}{\partial y} = -\frac{\partial q}{\partial x} = -\frac{Q}{4}$$

$$4 \cdot \frac{\partial p}{\partial x} = P = (\sigma_{11} + \sigma_{22}) = \nabla^2 U$$

$$\nabla^2 U = 4 \cdot \frac{\partial p}{\partial x} = 2 \cdot \frac{\partial p}{\partial x} + 2 \cdot \frac{\partial q}{\partial y}$$

$$\nabla^2 U - 2 \cdot \frac{\partial p}{\partial x} - 2 \cdot \frac{\partial q}{\partial y} = 0$$

$$\nabla^2 (U - xp - yq) = 0$$
$$(U - xp - yq) \quad \Rightarrow Harmonic$$
$$Let \quad (U - xp - yq) = a$$
$$U = a + xp + yq$$

If b denotes the imaginary part of a function $\chi(z)$ where $\chi(z) = a + ib$

The function U can be expressed as:

$$U = \mathrm{Re}[(x - iy) \cdot (p + iq) + (a + ib)]$$

Note that: $(p + iq)$ is related to $\phi(z)$ and $(a + ib)$ is related to $\chi(z)$ the two analytical

functions of the complex variable z.

$$U(z) = \mathrm{Re}[\bar{z} \cdot \phi(z) + \chi(z)] \qquad\qquad (\text{C-1})$$

Consequently, the solution of the 2-D problem is reduced to the determination of the two

analytical functions $\phi(z)$ *and* $\psi(z) = \dfrac{\partial \chi}{\partial z}$ from the boundary conditions.

To express the stresses in terms of $\phi(z)$ *and* $\psi(z)$:

$$\frac{\partial U}{\partial x} = \frac{\partial U(z, \bar{z})}{\partial x} = \frac{\partial U}{\partial z} \cdot \frac{\partial z}{\partial x} + \frac{\partial U}{\partial \bar{z}} \cdot \frac{\partial \bar{z}}{\partial x} = \frac{\partial U}{\partial z} + \frac{\partial \bar{z}}{\partial x}$$

Similarly

$$\frac{\partial U}{\partial y} = \frac{\partial U(z,\bar{z})}{\partial y} = \frac{\partial U}{\partial z} \cdot \frac{\partial z}{\partial y} + \frac{\partial U}{\partial \bar{z}} \cdot \frac{\partial \bar{z}}{\partial y} = i \cdot \left(\frac{\partial U}{\partial z} + \frac{\partial \bar{z}}{\partial x} \right)$$

$$\therefore \frac{\partial U}{\partial x} + i \frac{\partial U}{\partial y} = \left(\frac{\partial U}{\partial z} + \frac{\partial U}{\partial \bar{z}} \right) - \left(\frac{\partial U}{\partial z} - \frac{\partial U}{\partial \bar{z}} \right) = 2 \frac{\partial U}{\partial \bar{z}}$$

$$\mathrm{Re}[\phi(z)] = \tfrac{1}{2}\left[\phi(z) + \overline{\phi(z)}\right] = \tfrac{1}{2}\left[z + \bar{z}\right] = \tfrac{1}{2}\left[x + iy + x - iy\right] = x$$

$$\mathrm{Im}[\phi(z)] = \tfrac{1}{2\cdot i}\left[\phi(z) - \overline{\phi(z)}\right] = \tfrac{1}{2\cdot i}\left[z - \bar{z}\right] = \tfrac{1}{2\cdot i}\left[x + iy - x + iy\right] = y$$

$$\frac{\partial \phi(z)}{\partial z} = \phi'(z) \qquad , \qquad \frac{\partial \phi(z)}{\partial \bar{z}} = 0$$

From Equ. (C-1)

$$\frac{\partial U}{\partial x} + i \frac{\partial U}{\partial y} = 2 \frac{\partial U}{\partial \bar{z}} = \left[\phi(z) + z \cdot \overline{\phi'(z)} + \overline{\psi(z)}\right]$$

$$\frac{\partial}{\partial y}\left(\frac{\partial U}{\partial x} + i \frac{\partial U}{\partial y} \right) = i \cdot \left[\frac{\partial}{\partial z}\left(\frac{\partial U}{\partial x} + i \frac{\partial U}{\partial y} \right) - \frac{\partial}{\partial \bar{z}}\left(\frac{\partial U}{\partial x} + i \frac{\partial U}{\partial y} \right) \right]$$

$$\frac{\partial^2 U}{\partial x \partial y} + i \frac{\partial^2 U}{\partial y^2} = -\tau_{12} + i \cdot \sigma_{11} = i \cdot \left(\sigma_{11} + i \cdot \tau_{12} \right)$$

$$\left(\sigma_{11} + i \cdot \tau_{12} \right) = \left[\phi'(z) + \overline{\phi'(z)} - z \cdot \overline{\phi''(z)} - \overline{\psi'(z)} \right] \qquad\qquad\text{(C-2)}$$

Again,

$$\frac{\partial}{\partial x}\left(\frac{\partial U}{\partial x} + i \frac{\partial U}{\partial y} \right) = \left[\frac{\partial}{\partial z}\left(\frac{\partial U}{\partial x} + i \frac{\partial U}{\partial y} \right) - \frac{\partial}{\partial \bar{z}}\left(\frac{\partial U}{\partial x} + i \frac{\partial U}{\partial y} \right) \right]$$

$$\frac{\partial^2 U}{\partial x^2} + i \frac{\partial^2 U}{\partial x \partial y} = \sigma_{22} - i \cdot \tau_{12}$$

$$\sigma_{22} - i \cdot \tau_{12} = \left[\phi'(z) + \overline{\phi'(z)} + z \cdot \overline{\phi''(z)} + \overline{\psi'(z)} \right] \qquad\qquad\text{(C-3)}$$

Add equ. (B) and (C) to get:

$$\sigma_{11} + \sigma_{22} = 2\left[\phi'(z) + \overline{\phi'(z)}\right] = 4 \cdot \text{Re}\left[\phi'(z)\right] \qquad \text{(C-4)}$$

Subtract (C-2) and (C-3) to get:

$$\sigma_{22} - \sigma_{11} - 2i \cdot \tau_{12} = 2\left[\overline{z \cdot \phi''(z)} + \overline{\psi'(z)}\right]$$

$$\therefore \sigma_{22} - \sigma_{11} + 2i \cdot \tau_{12} = 2\overline{\left[\overline{z \cdot \phi''(z)} + \overline{\psi'(z)}\right]} = 2\left[\overline{z} \cdot \phi''(z) + \psi'(z)\right]$$

$$\therefore \sigma_{22} - \sigma_{11} + 2i \cdot \tau_{12} = 2\left[\overline{z} \cdot \phi''(z) + \psi'(z)\right] \qquad \text{(C-5)}$$

Equations (C-4) and (C-5) refer to stress potential (Goursal function)

To express displacement components in terms of $\phi(z)\ and\ \psi(z)$:

From Hook's law:

$$\sigma_{ij} = (2 \cdot \mu \cdot \varepsilon_{ij}) + (\lambda \cdot \varepsilon_{kk} \cdot \delta_{ij})$$

$$\sigma_{ij} = \left(\frac{E}{1+v} \cdot \varepsilon_{ij}\right) + \left(\frac{v \cdot E}{(1+v)(1-2v)} \cdot \varepsilon_{kk} \cdot \delta_{ij}\right)$$

$\mu\ and\ \lambda\ \ are\ called\ Lame'\ 's\ function$

$i, j = 1,2\ \ ,\ \ if\ i = j \Rightarrow \delta = 1\ \ ,\ \ \ \ \ if\ i \neq j \Rightarrow \delta = 0$

$$\varepsilon_{kk} = \varepsilon_{11} + \varepsilon_{22} + \varepsilon_{33}$$

Assuming plane strain condition: $\varepsilon_{3i} = 0$

$$\varepsilon_{kk} = \varepsilon_{11} + \varepsilon_{22} = \frac{du_x}{dx} + \frac{du_y}{dy}$$

$$\sigma_{11} = \frac{\partial^2 U}{\partial y^2} = \left(2 \cdot \mu \cdot \frac{du_x}{dx}\right) + (\lambda \cdot \varepsilon_{kk})$$

$$\sigma_{22} = \frac{\partial^2 U}{\partial x^2} = \left(2 \cdot \mu \cdot \frac{du_y}{dy}\right) + (\lambda \cdot \varepsilon_{kk})$$

$$\sigma_{12} = -\frac{\partial^2 U}{\partial x \partial y} = 2 \cdot \mu \cdot \left(\frac{du_x}{dy} + \frac{du_y}{dx}\right)$$

Adding the expressions of σ_{11} and σ_{22}

$$\sigma_{11} + \sigma_{22} = \nabla^2 U = 2 \cdot (\lambda + \mu) \cdot \left(\frac{du_x}{dx} + \frac{du_y}{dy}\right)$$

$$\therefore \frac{du_y}{dy} = \frac{\nabla^2 U}{2 \cdot (\lambda + \mu)} - \frac{du_x}{dx}$$

Again,

$$\sigma_{11} = \left(2 \cdot \mu \cdot \frac{du_x}{dx}\right) + (\lambda \cdot (\varepsilon_{11} + \varepsilon_{22}))$$

$$\sigma_{11} = \left(2 \cdot \mu \cdot \frac{du_x}{dx}\right) + \left[\lambda \cdot \left(\frac{du_x}{dx} + \frac{\nabla^2 U}{2 \cdot (\lambda + \mu)} - \frac{du_x}{dx}\right)\right]$$

$$\sigma_{11} = \left(2 \cdot \mu \cdot \frac{du_x}{dx}\right) + \left[\lambda \cdot \left(\frac{\nabla^2 U}{2 \cdot (\lambda + \mu)}\right)\right]$$

$$\because \sigma_{11} = \nabla^2 U - \sigma_{22} = \nabla^2 U - \frac{\partial^2 U}{\partial x^2}$$

$$\therefore \nabla^2 U - \frac{\partial^2 U}{\partial x^2} = \left(2 \cdot \mu \cdot \frac{du_x}{dx}\right) + \left[\lambda \cdot \left(\frac{\nabla^2 U}{2 \cdot (\lambda + \mu)}\right)\right]$$

$$2 \cdot \mu \cdot \frac{du_x}{dx} = \nabla^2 U \cdot \left[\frac{\lambda + 2\mu}{2 \cdot (\lambda + \mu)}\right] - \frac{\partial^2 U}{\partial x^2} \qquad \text{(C-6)}$$

Similarly,

$$2 \cdot \mu \cdot \frac{du_y}{dy} = \nabla^2 U \cdot \left[\frac{\lambda + 2\mu}{2 \cdot (\lambda + \mu)} \right] - \frac{\partial^2 U}{\partial y^2} \tag{C-7}$$

Now,

$$\because \nabla^2 U = \sigma_{11} + \sigma_{22} = P = 4 \cdot \frac{\partial p}{\partial x} = 4 \cdot \frac{\partial q}{\partial y}$$

$$\because p + iq = \phi(z)$$

Using these in Eq. (C-6) and (C-7) to get:

$$2 \cdot \mu \cdot u_x = 2 \cdot p \cdot \left[\frac{\lambda + 2\mu}{\lambda + \mu} \right] - \frac{\partial U}{\partial x} + f(y) \tag{C-8}$$

$$2 \cdot \mu \cdot u_y = 2 \cdot q \cdot \left[\frac{\lambda + 2\mu}{\lambda + \mu} \right] - \frac{\partial U}{\partial y} + f(x) \tag{C-9}$$

Note: *f(x)* and *f(y)* are integration constants can be shown to be constants and represent rigid body motion. Drop them from the analysis.

$$2 \cdot \mu \cdot \left(u_x + iu_y \right) = 2 \cdot \left[\frac{\lambda + 2\mu}{\lambda + \mu} \right] \cdot (p + iq) - \left(\frac{\partial U}{\partial x} + i \frac{\partial U}{\partial y} \right)$$

$$2 \cdot \mu \cdot \left(u_x + iu_y \right) = 2 \cdot \left[\frac{\lambda + 2\mu}{\lambda + \mu} \right] \cdot \phi(z) - \left[\phi(z) + z \cdot \overline{\phi'(z)} + \overline{\psi(z)} \right]$$

$$2 \cdot \mu \cdot \left(u_x + iu_y \right) = \eta \cdot \phi(z) - z \cdot \overline{\phi'(z)} - \overline{\psi(z)}$$

Where:

$$\eta = \frac{\lambda + 3\mu}{\lambda + \mu} = \begin{cases} 3 - 4\nu & \textit{Plain strain} \\ \\ \dfrac{3 - \nu}{1 + \nu} & \textit{Plain stress} \end{cases}$$

In polar:

$$\sigma_r + \sigma_\theta = 2\left[\phi'(z) + \overline{\phi'(z)}\right]$$

$$\sigma_\theta - \sigma_r + 2 \cdot i \cdot \tau_{r\theta} = 2\left[\bar{z} \cdot \phi''(z) + \psi'(z)\right] \cdot e^{2i\theta}$$

$$\sigma_r - i \cdot \tau_{r\theta} = \left[\phi'(z) + \overline{\phi'(z)}\right] - \left[\bar{z} \cdot \phi''(z) + \psi'(z)\right] \cdot e^{2i\theta}$$

$$2 \cdot \mu \cdot \left(u_r + iu_\theta\right) = \left[\eta \cdot \phi(z) - z \cdot \overline{\phi'(z)} - \overline{\psi(z)}\right] \cdot e^{-i\theta}$$

$$2 \cdot \mu \cdot \left(u_r - iu_\theta\right) = \left[\eta \cdot \overline{\phi(z)} - \bar{z} \cdot \phi'(z) - \psi(z)\right] \cdot e^{i\theta}$$

Stress state around a circular hole in which a ring, consisting of several concentrically welded rings of differing materials, is inserted

It is assumed that infinitely large elastic, isotropic plane containing a circular hole of radius *"R"* is subjected to a given system of external forces (tension, compression, pure bending, etc.) and that composite ring is welded into the hole, the ring being made of concentric elastic rings (K_1, K_2, K_3, ... K_s) of various materials. The stress state due to the external forces is to be determined in the composite ring and also in the elastic plane. It is

assumed that in the hole-free plate subject to the same external stresses as the same plate with a hole, the stress function *"U"* is a polynomial of the *(m+1)-th* degree.
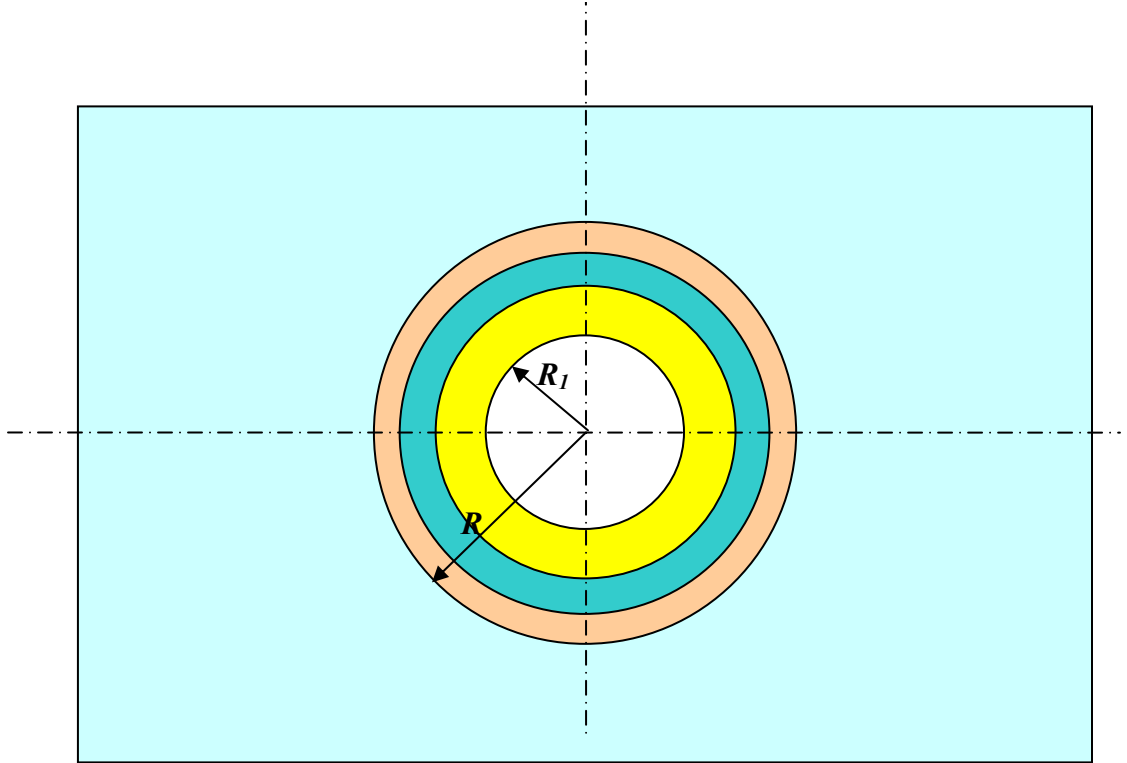
Figure C-1: Infinitely large elastic, isotropic plane contains circular hole surrounded by concentric elastic rings subjected to a given system of external forces

For the elastic plate:

$$\phi(z) = \phi^o(z) + iC \sum_{k=1}^{\infty} \alpha_{-k} \cdot \frac{R^k}{z^k}$$

$$\psi(z) = \psi^o(z) - iC \sum_{k=1}^{\infty} \beta_{-k} \cdot \frac{R^k}{z^k}$$

Where:

$$\phi^o(z) = iC \sum_{k=1}^{m} A_k \cdot \frac{z^k}{R^k} \quad , \quad \psi^o(z) = -iC \sum_{k=0}^{m} B_k \cdot \frac{z^k}{R^k}$$

For each layer:

$$\phi^{(j)}(z) = iC \sum_{-\infty}^{\infty} a_k^{(j)} \cdot \frac{z^k}{R^k} \quad , \quad \psi^{(j)}(z) = -iC \sum_{-\infty}^{\infty} b_k^{(j)} \cdot \frac{z^k}{R^k}$$

Boundary Conditions:

At $R = R_1$

$$\sigma_r^{(1)} - i\tau_{r\theta}^{(1)} = 0$$

At $R = R_j$

$$\sigma_r^{(j)} - i\tau_{r\theta}^{(j)} = \sigma_r^{(j-1)} - i\tau_{r\theta}^{(j-1)}$$

$$u_r^{(j)} - iu_\theta^{(j)} = u_r^{(j-1)} - iu_\theta^{(j-1)}$$

At $R = R_{s+1}$

$$\sigma_r^{(s)} - i\tau_{r\theta}^{(s)} = \sigma_r - i\tau_{r\theta}$$

$$u_r^{(s)} - iu_\theta^{(s)} = u_r - iu_\theta$$

$$\phi(z) = iC \sum_{-\infty}^{\infty} a_k \cdot \frac{z^k}{R^k}$$

$$\phi'(z) = iC \cdot k \cdot \sum_{-\infty}^{\infty} a_k \cdot \frac{z^{k-1}}{R^k}$$

$$\phi''(z) = iC \cdot k \cdot (k-1) \cdot \sum_{-\infty}^{\infty} a_k \cdot \frac{z^{k-2}}{R^k}$$

$$\psi(z) = -iC \sum_{-\infty}^{\infty} b_k \cdot \frac{z^k}{R^k}$$

$$\psi'(z) = -iC \cdot k \cdot \sum_{-\infty}^{\infty} b_k \cdot \frac{z^{k-1}}{R^k}$$

$$\sigma_r^{(1)} - i\tau_{r\theta}^{(1)} = \left[\phi'(z) + \overline{\phi'(z)}\right] - \left[\overline{z} \cdot \phi''(z) + \psi'(z)\right] \cdot e^{2i\theta} = 0$$

$$i \cdot C \cdot k \cdot \sum a_k \frac{z^{k-1}}{R^k} + i \cdot C \cdot k \cdot \sum a_k \frac{\overline{z^{k-1}}}{R^k}$$

$$= e^{2i\theta} \cdot \left[\overline{z} \cdot i \cdot C \cdot k \cdot (k-1) \cdot \sum a_k \frac{z^{k-2}}{R^k} - i \cdot C \cdot k \cdot \sum b_k \frac{z^{k-1}}{R^k}\right]$$

$$\sum a_k \frac{z^{k-1}}{R^k} + \sum a_k \frac{\overline{z^{k-1}}}{R^k} = e^{2i\theta} \cdot \left[\overline{z} \cdot (k-1) \cdot \sum a_k \frac{z^{k-2}}{R^k} - \sum b_k \frac{z^{k-1}}{R^k}\right]$$

Replace z by $R_1 \cdot e^{i\theta}$ and $\bar{z}$ by $R_1 \cdot e^{-i\theta}$

$$\sum a_k \frac{R_1^{k-1}}{R^k} \cdot e^{i\theta(k-1)} + \sum a_k \frac{R_1^{k-1}}{R^k} \cdot e^{-i\theta(k-1)} - (k-1) \cdot \sum a_k \frac{R_1^{k-1}}{R^k} \cdot e^{i\theta(k-1)}$$

$$+ \sum b_k \frac{R_1^{k-1}}{R^k} \cdot e^{i\theta(k+1)} = 0$$

For e^0

$$\frac{a_1}{R} + \frac{a_1}{R} - 0 + b_{-1} \cdot \frac{R}{R_1^2} = 0$$

$$2a_1 \frac{1}{R} + b_{-1} \cdot \frac{R}{R_1^2} = 0$$

$$2a_1 \frac{R_1}{R} + b_{-1} \cdot \frac{R}{R_1} = 0 \qquad \text{"First relation ---------} \rightarrow \text{"Confirmed"}$$

For the elastic plate:

$$\phi(z) = iC \left[\sum_{k=1}^{m} A_k \cdot \frac{z^k}{R^k} + \sum_{k=1}^{m} \alpha_{-k} \cdot \frac{R^k}{z^k} \right]$$

$$\psi(z) = -iC \left[\sum_{k=0}^{m} B_k \cdot \frac{z^k}{R^k} + \sum_{k=1}^{m+2} \beta_{-k} \cdot \frac{R^k}{z^k} \right]$$

For each layer:

$$\phi^{(j)}(z) = iC \sum_{k=-m}^{m+2} a_k^{(j)} \cdot \frac{z^k}{R^k} \qquad , \qquad \psi^{(j)}(z) = -iC \sum_{k=-(m+2)}^{m} b_k^{(j)} \cdot \frac{z^k}{R^k}$$

Uni-axial tension applied to a plate containing a circular hole into which an elastic ring is inserted. Consider a composite ring welded into a circular hole in an infinitely large isotropic plate which is stressed by a uniform tensile stress *P*. The stress and displacement components in the plate and in the ring are to be determined.

The stress functions for the continuous hole-free plate are of the type:

$$\phi^o(z) = \frac{P}{4} z \ ; \ \psi^o(z) = -\frac{P}{2} z$$

Considering the stress function *"U"* is a polynomial of the second degree (*i.e m=1*), the following stress function are obtained.

For the plate:

$$\phi(z) = \frac{PR}{4}\left[\frac{z}{R} + \alpha_{-1}\frac{R}{z} \right]$$

$$\psi(z) = -\frac{PR}{4}\left[2\frac{z}{R} + \beta_{-1}\frac{R}{z} + \beta_{-3}\frac{R^3}{z^3} \right]$$

For each ring:

$$\phi(z) = \frac{PR}{4}\left[a_3\frac{z^3}{R^3} + a_1\frac{z}{R} + a_{-1}\frac{R}{z} \right]$$

$$\psi(z) = -\frac{PR}{4}\left[b_1\frac{z}{R} + b_{-1}\frac{R}{z} + b_{-3}\frac{R^3}{z^3} \right]$$

135

Stresses and displacements in the plate:

$$\sigma_r = \frac{P}{2}\left[\left(1 - \frac{1}{2}\beta_{-1}\cdot\frac{R^2}{r^2}\right) + \left(1 - 2\alpha_{-1}\cdot\frac{R^2}{r^2} - \frac{3}{2}\beta_{-3}\cdot\frac{R^4}{r^4}\right)\cdot\cos(2\cdot\theta)\right]$$

$$\sigma_\theta = \frac{P}{2}\left[\left(1 + \frac{1}{2}\beta_{-1}\cdot\frac{R^2}{r^2}\right) - \left(1 - \frac{3}{2}\beta_{-3}\cdot\frac{R^4}{r^4}\right)\cdot\cos(2\cdot\theta)\right]$$

$$\tau_{r\theta} = -\frac{P}{2}\left[1 + \alpha_{-1}\cdot\frac{R^2}{r^2} + \frac{3}{2}\beta_{-3}\cdot\frac{R^4}{r^4}\right]\cdot\sin(2\cdot\theta)$$

$$u_r = \frac{P\cdot R}{8\mu}\left\{\left[(\eta-1)\frac{r}{R} + \beta_{-1}\cdot\frac{R}{r}\right] + \left[2\frac{r}{R} + \alpha_{-1}\cdot(\eta+1)\frac{R}{r} + \beta_{-3}\cdot\frac{R^3}{r^3}\right]\cdot\cos(2\cdot\theta)\right\}$$

$$u_\theta = \frac{P\cdot R}{8\mu}\left[-2\frac{r}{R} - \alpha_{-1}\cdot(\eta-1)\frac{R}{r} + \beta_{-3}\cdot\frac{R^3}{r^3}\right]\cdot\sin(2\cdot\theta)$$

Stresses and displacements in each ring:

$$\sigma_r = \frac{P}{2}\left[\left(a_1 - \frac{1}{2}b_{-1}\cdot\frac{R^2}{r^2}\right) + \left(\frac{b_1}{2} - 2a_{-1}\cdot\frac{R^2}{r^2} - \frac{3}{2}b_{-3}\cdot\frac{R^4}{r^4}\right)\cdot\cos(2\cdot\theta)\right]$$

$$\sigma_\theta = \frac{P}{2}\left[\left(a_1 + \frac{1}{2}b_{-1}\cdot\frac{R^2}{r^2}\right) - \left(\frac{b_1}{2} - 6\cdot a_3\frac{r^2}{R^2} - \frac{3}{2}b_{-3}\cdot\frac{R^4}{r^4}\right)\cdot\cos(2\cdot\theta)\right]$$

$$\tau_{r\theta} = \frac{P}{2}\left[3\cdot a_3\frac{r^2}{R^2} - \frac{b_1}{2} - a_{-1}\cdot\frac{R^2}{r^2} - \frac{3}{2}b_{-3}\cdot\frac{R^4}{r^4}\right]\cdot\sin(2\cdot\theta)$$

$$u_r = \frac{P\cdot R}{8\mu}\left\{\begin{array}{l}\left[a_1(\eta-1)\dfrac{r}{R} + b_{-1}\cdot\dfrac{R}{r}\right] \\ + \left[a_3(\eta-3)\dfrac{r^3}{R^3} + b_1\dfrac{r}{R} + a_{-1}\cdot(\eta+1)\dfrac{R}{r} + b_{-3}\cdot\dfrac{R^3}{r^3}\right]\cdot\cos(2\cdot\theta)\end{array}\right\}$$

$$u_\theta = \frac{P\cdot R}{8\mu}\left[a_3(\eta+3)\frac{r^3}{R^3} - b_1\frac{r}{R} - a_{-1}\cdot(\eta-1)\frac{R}{r} + b_{-3}\cdot\frac{R^3}{r^3}\right]\cdot\sin(2\cdot\theta)$$

In case of fiber presence instead of hole
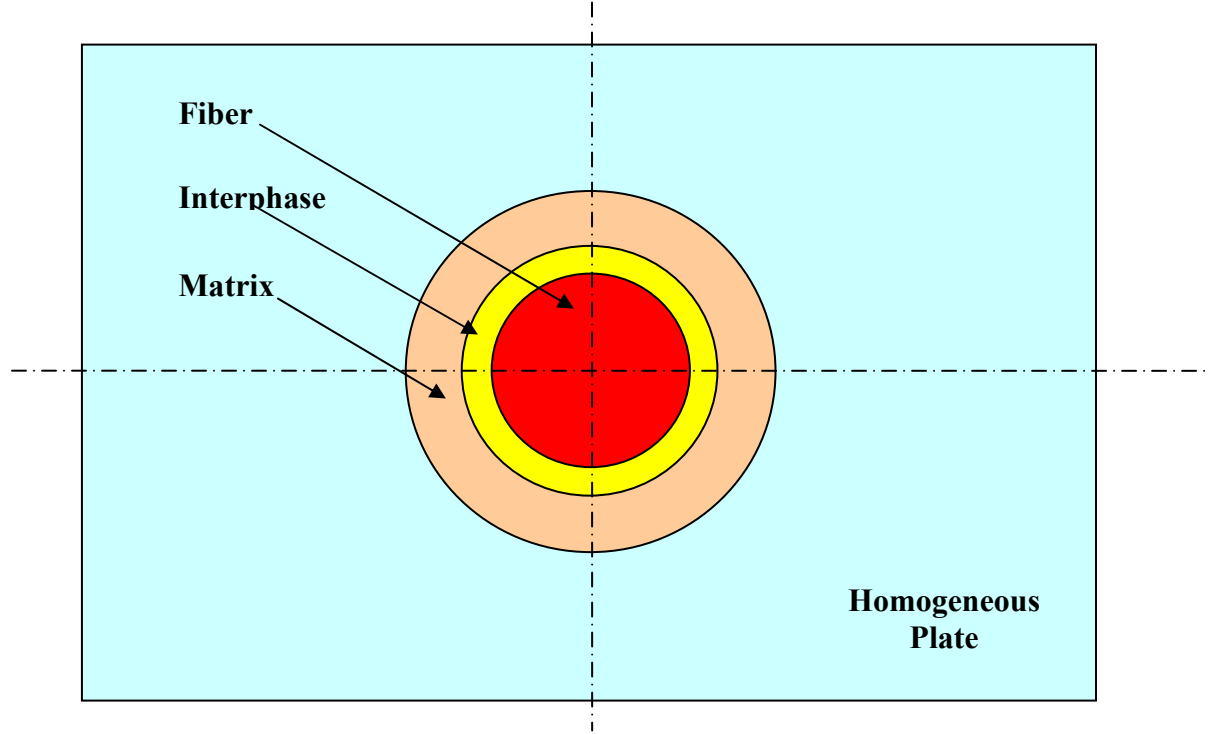
Figure C-2: Infinitely large homogeneous plate contains circular fiber surrounded by

concentric elastic rings subjected to a given system of external forces

In this case, the equations of the layers can be used for the interphase and the matrix.

For the fiber, the radial stress should be finite value at the fiber center; i.e.

$b_{-1} = a_{-1} = b_{-3} = 0$ and the equations will be in the following form:

$$\sigma_r = \frac{P}{2}\left[a_1 + \left(\frac{b_1}{2}\right) \cdot \cos(2 \cdot \theta)\right]$$

$$\sigma_\theta = \frac{P}{2}\left[a_1 - \left(\frac{b_1}{2} - 6 \cdot a_3 \frac{r^2}{R^2}\right) \cdot \cos(2 \cdot \theta)\right]$$

$$\tau_{r\theta} = \frac{P}{2}\left[3 \cdot a_3 \frac{r^2}{R^2} - \frac{b_1}{2}\right] \cdot \sin(2 \cdot \theta)$$

$$u_r = \frac{P \cdot R}{8\mu}\left\{\left[a_1(\eta - 1)\frac{r}{R}\right] + \left[a_3(\eta - 3)\frac{r^3}{R^3} + b_1\frac{r}{R}\right] \cdot \cos(2 \cdot \theta)\right\}$$

$$u_\theta = \frac{P \cdot R}{8\mu}\left[a_3(\eta + 3)\frac{r^3}{R^3} - b_1\frac{r}{R}\right] \cdot \sin(2 \cdot \theta)$$

APPENDIX D: LOAD-DISPLACEMENT AND STRESS-STRAIN CURVES
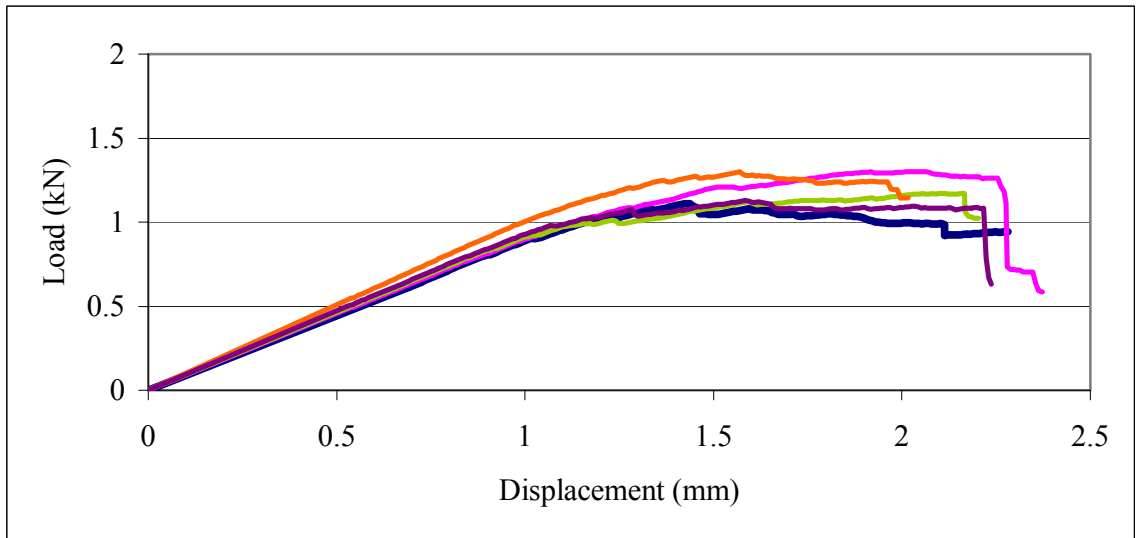
Figure D-1. Load-displacement curves for 5 layers broken twill/carbon fabric
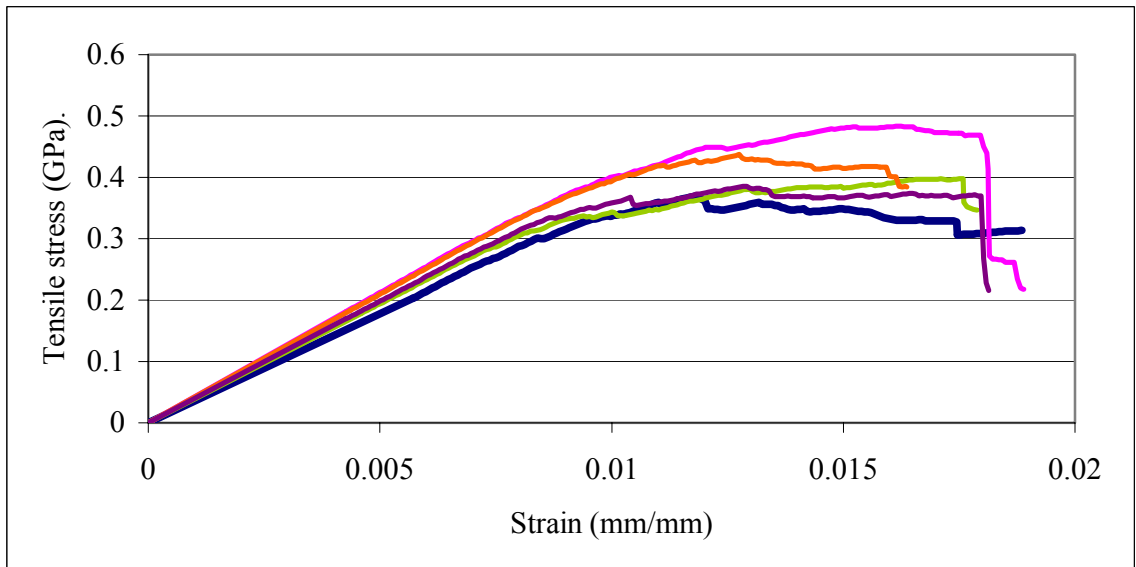
Figure D-2. Stress-strain curves for 5 layers broken twill/carbon fabric
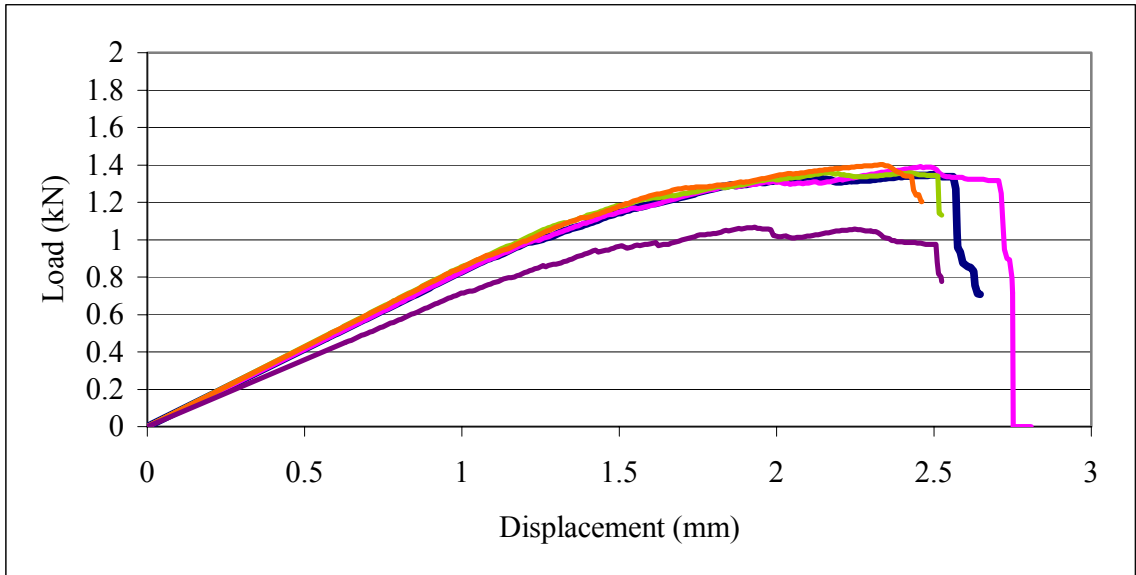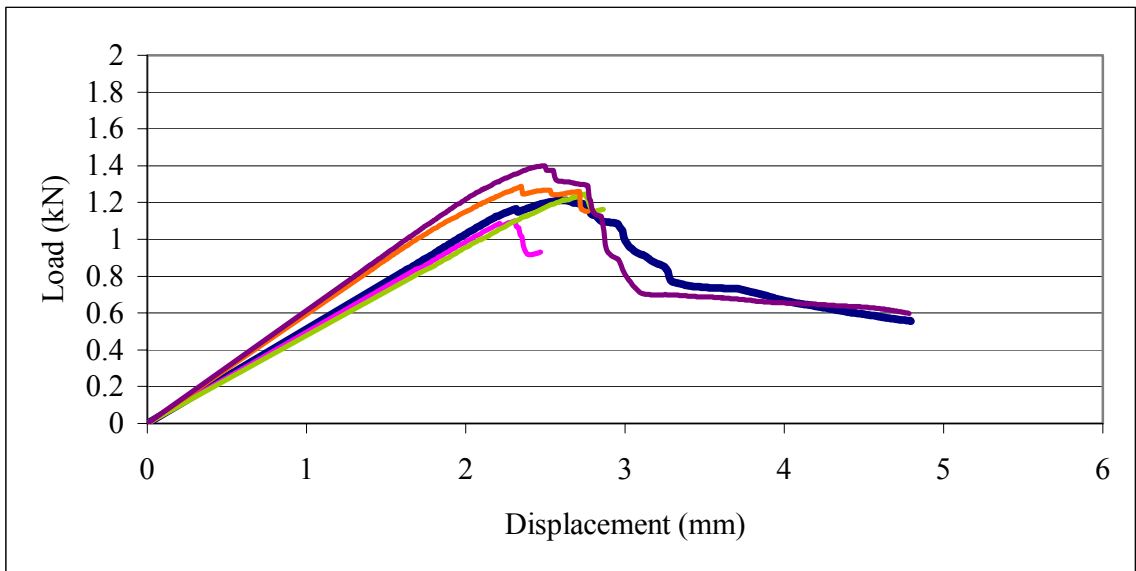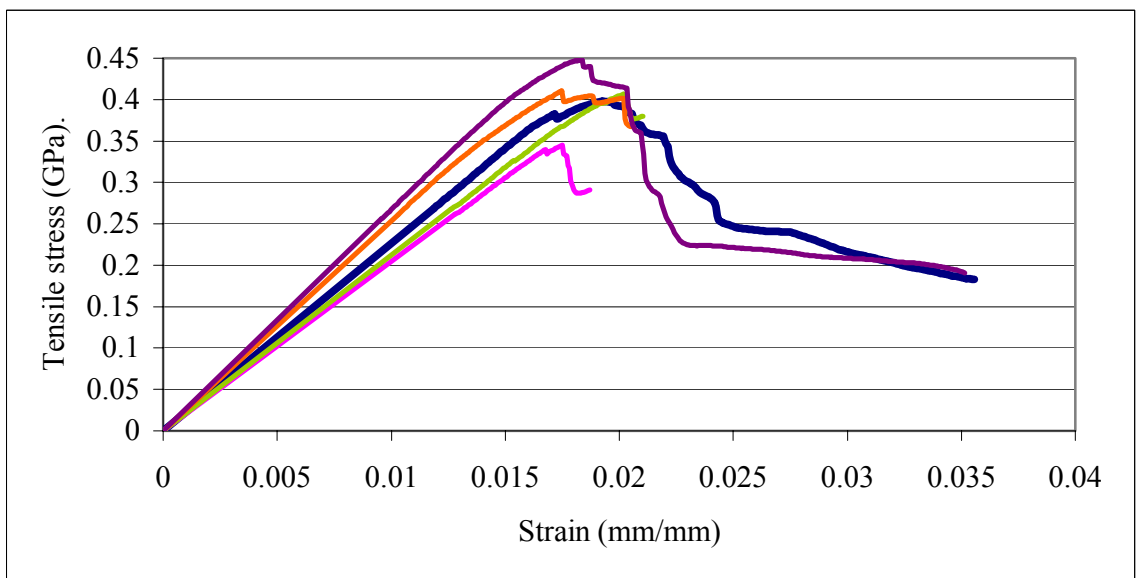
Figure D-3. Load-displacement curves for 6 layers broken twill/carbon fabric
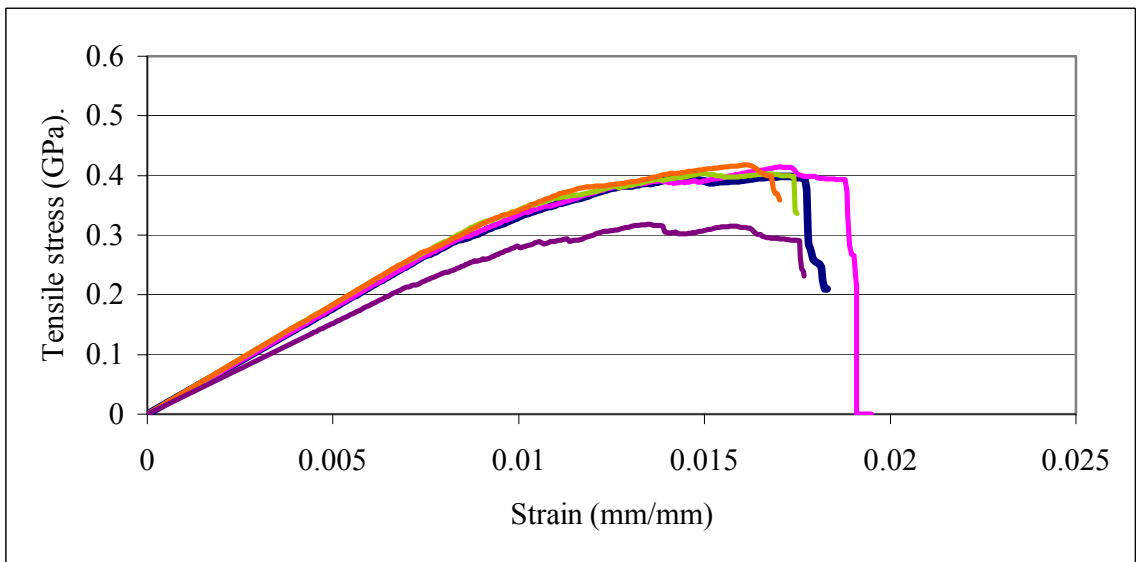
Figure D-4. Stress-strain curves for 6 layers broken twill/carbon fabric

141
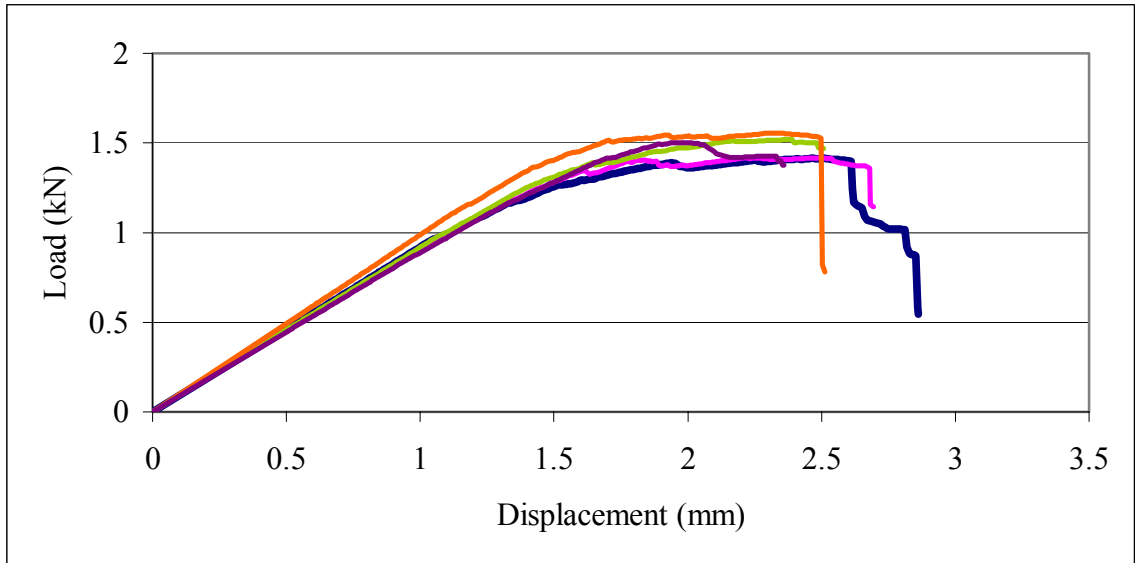
Figure D-5. Load-displacement curves for 7 layers broken twill/carbon fabric
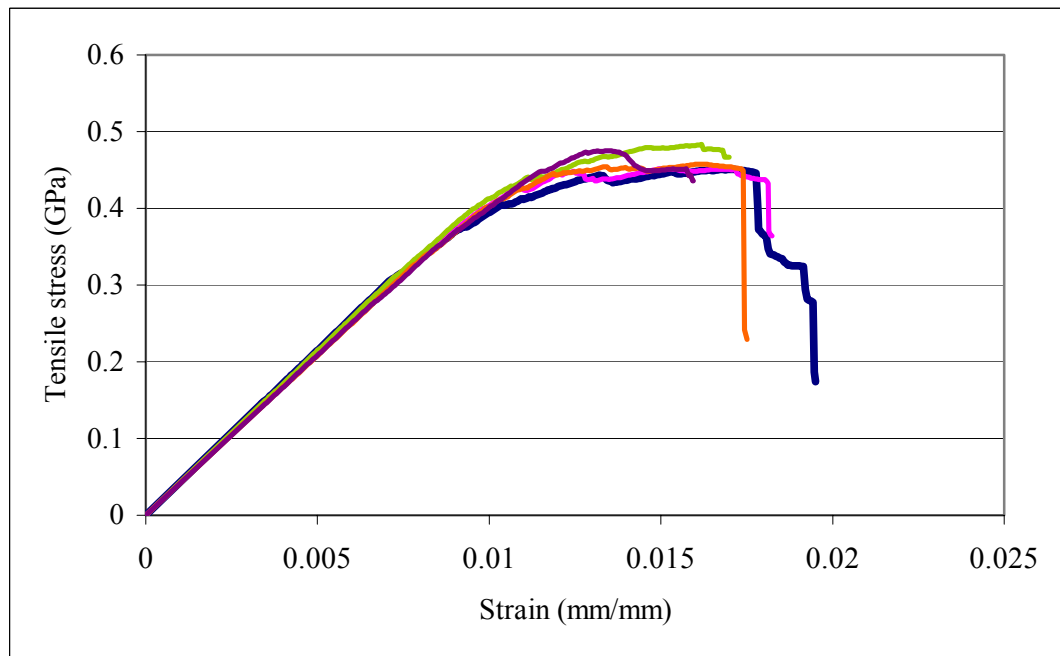
Figure D-6. Stress-strain curves for 7 layers broken twill/carbon fabric

142
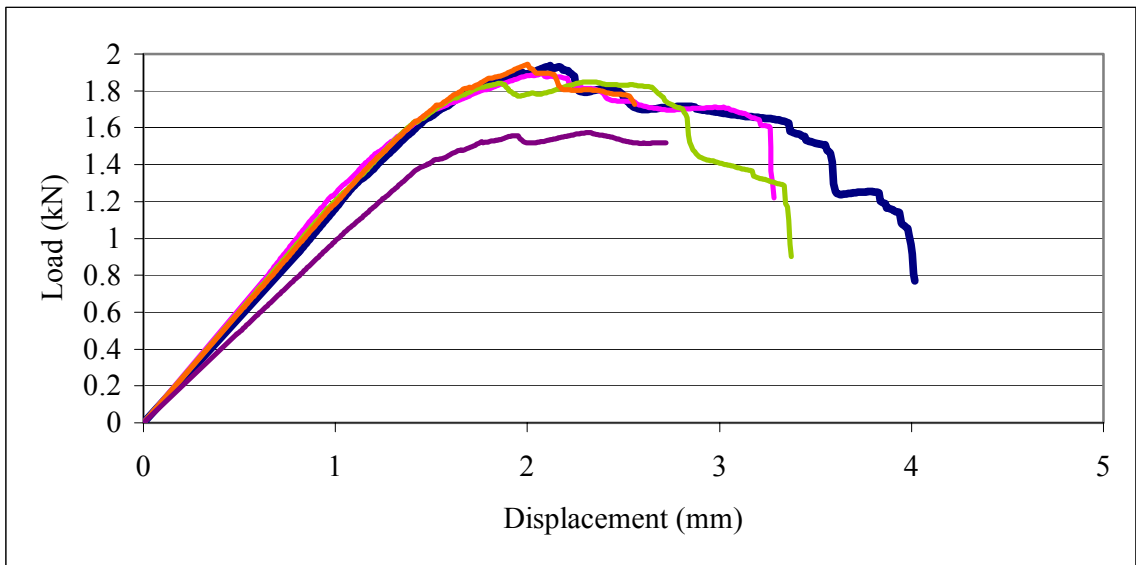
Figure D-7. Load-displacement curves for 8 layers broken twill/carbon fabric
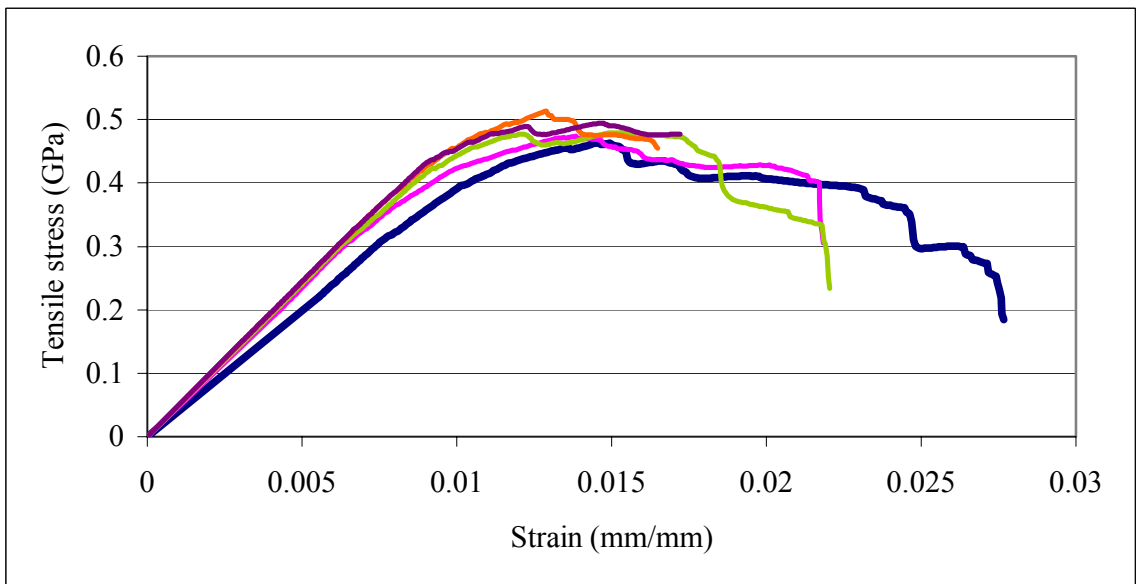
Figure D-8. Stress-strain curves for 8 layers broken twill/carbon fabric
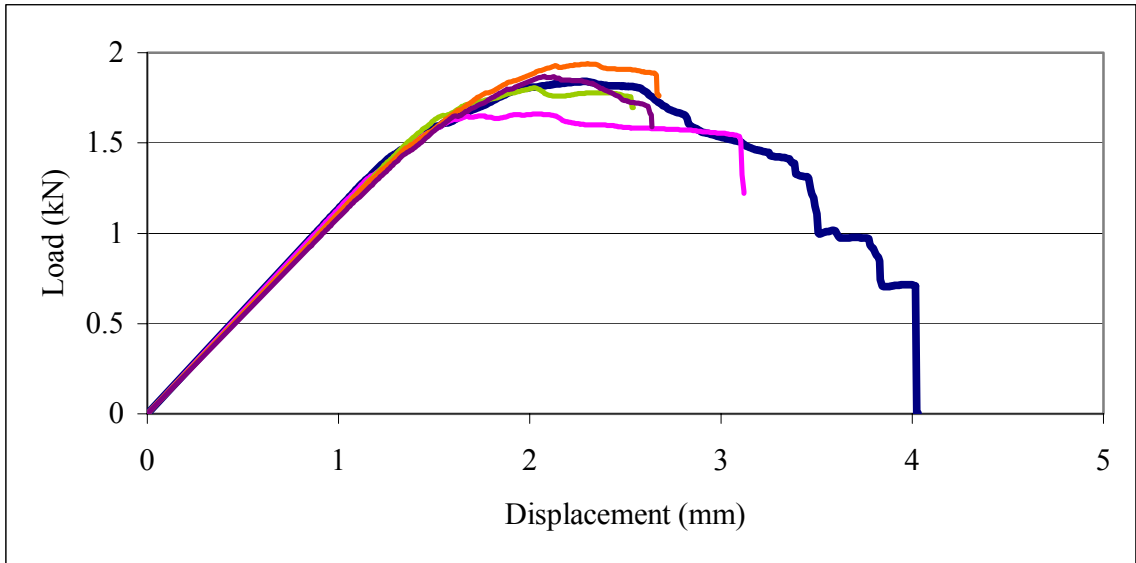
Figure D-9. Load-displacement curves for 9 layers broken twill/carbon fabric
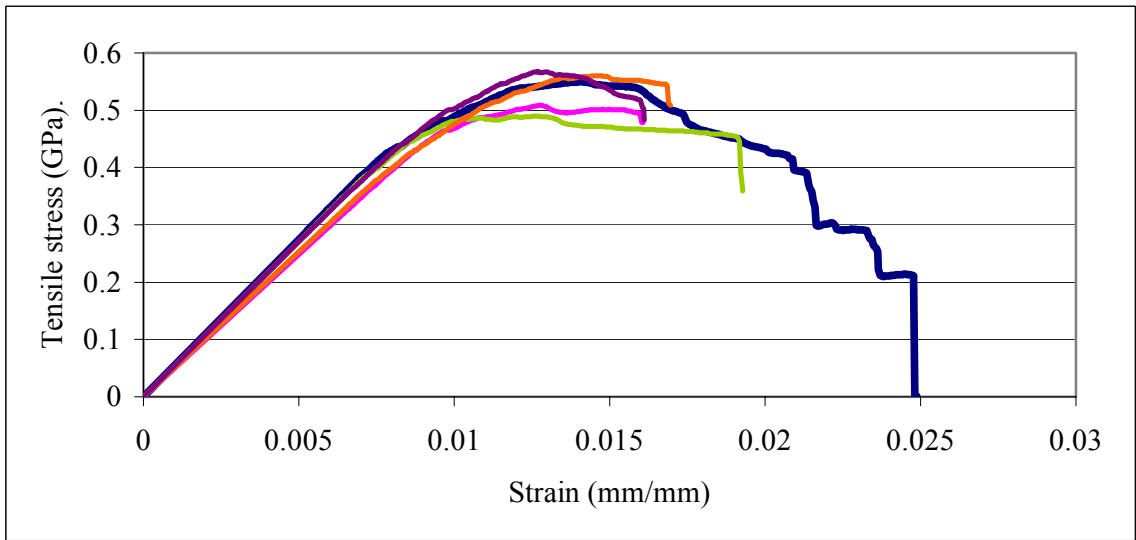
Figure D-10. Stress-strain curves for 9 layers broken twill/carbon fabric

144

Figure D-11. Load-displacement curves for 5 layers plain/glass fabric
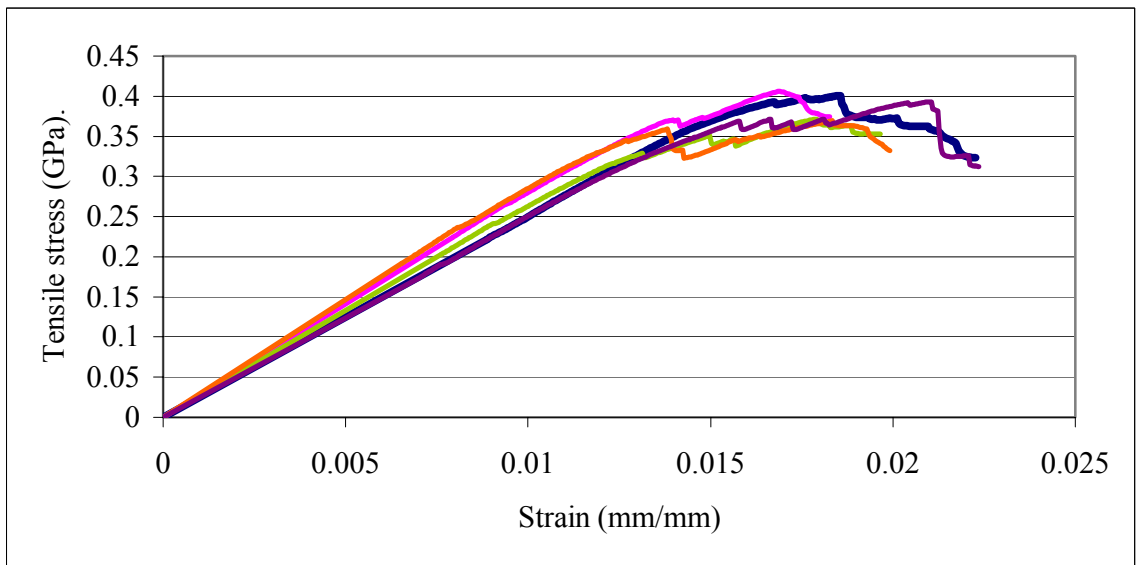

Figure D-12. Stress-strain curves for 5 layers plain/glass fabric

145
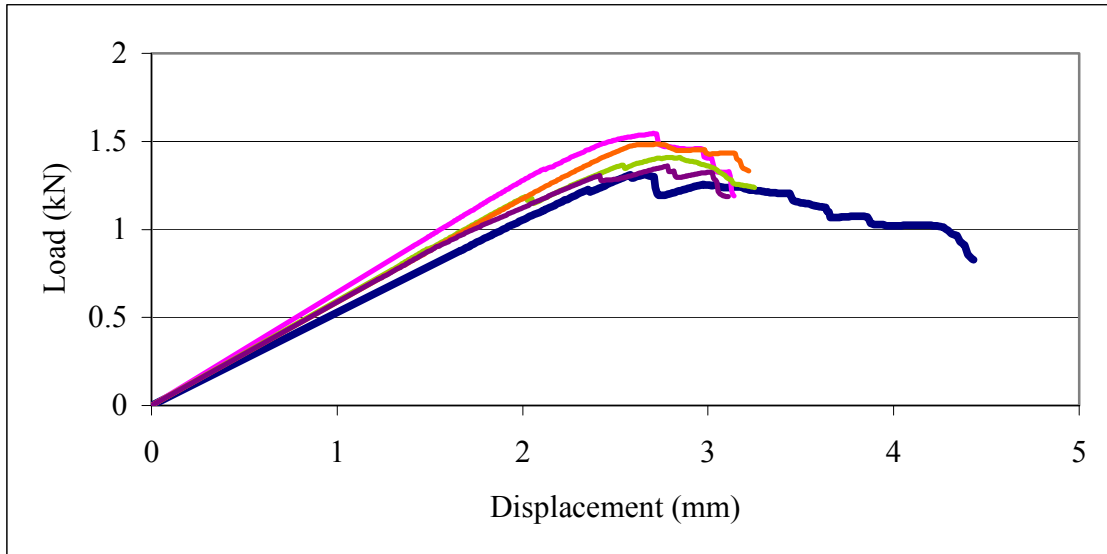
Figure D-13. Load-displacement curves for 6 layers plain/glass fabric
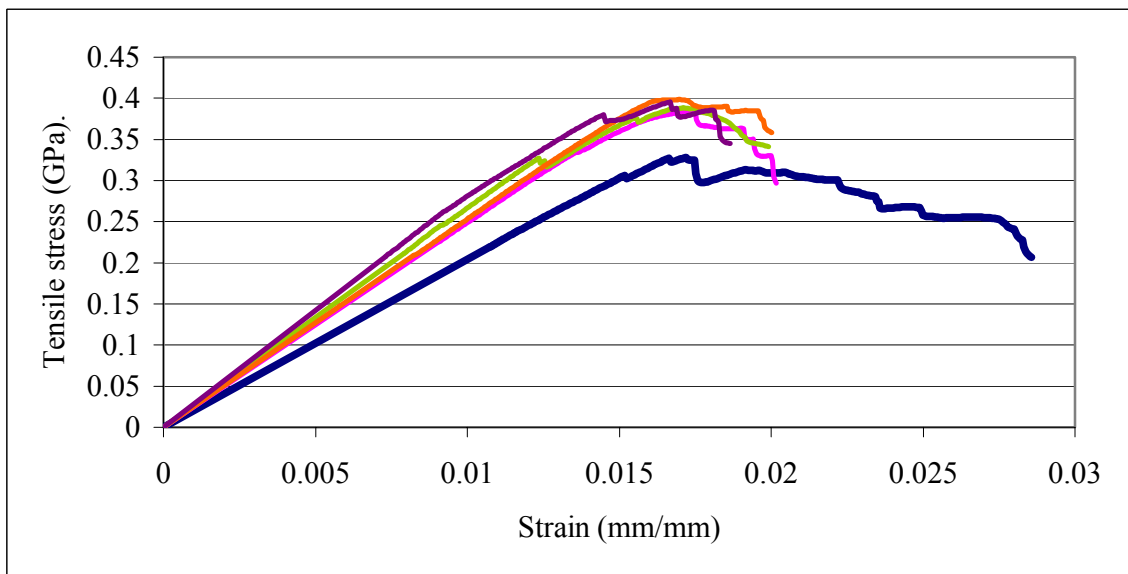
Figure D-14. Stress-strain curves for 6 layers plain/glass fabric

146
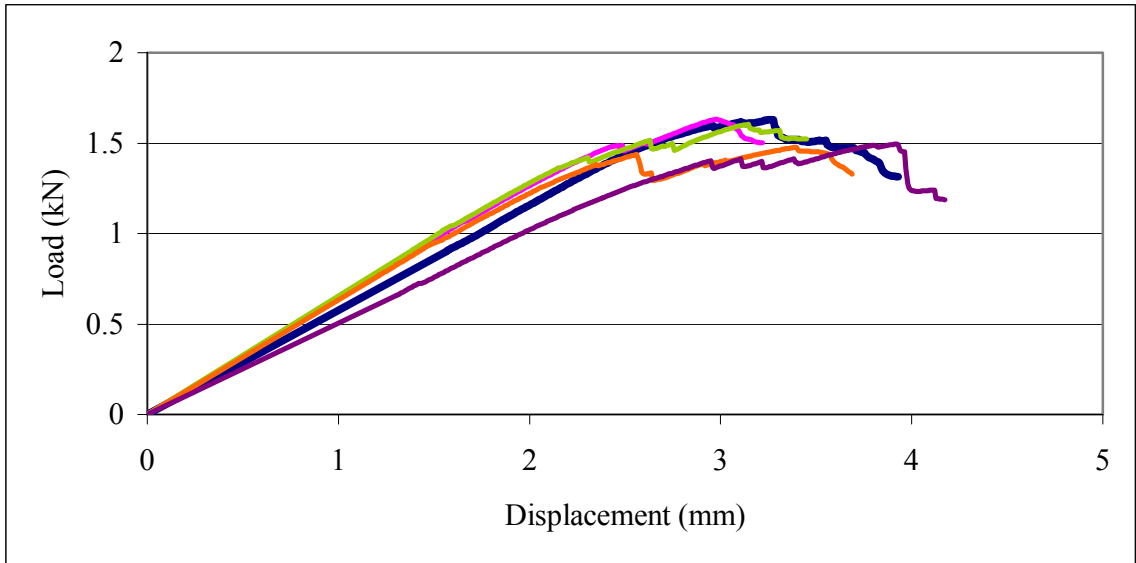
Figure D-15. Load-displacement curves for 7 layers plain/glass fabric

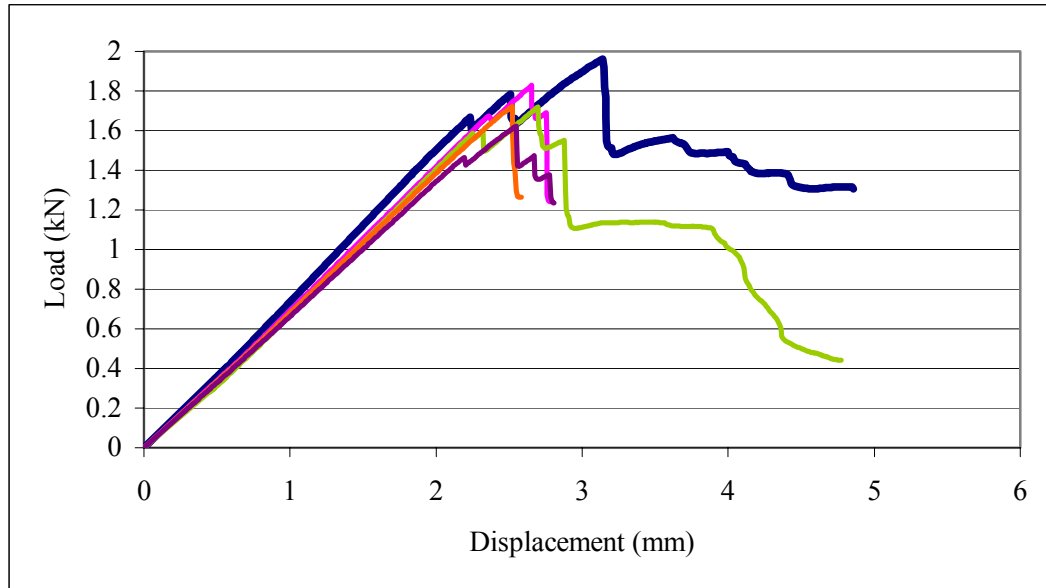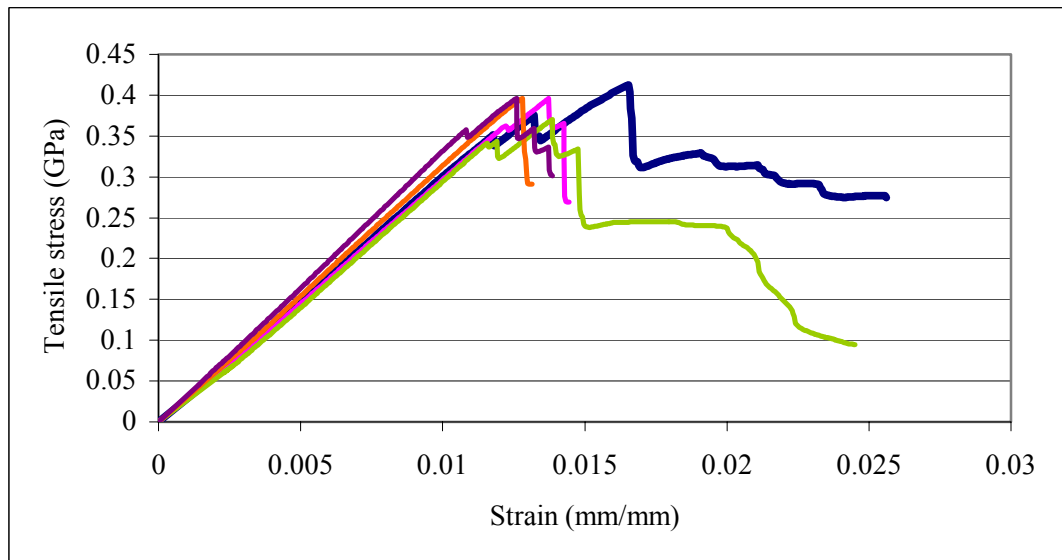Figure D-16. Stress-strain curves for 7 layers plain/glass fabric

147

Figure D-17. Load-displacement curves for 8 layers plain/glass fabric

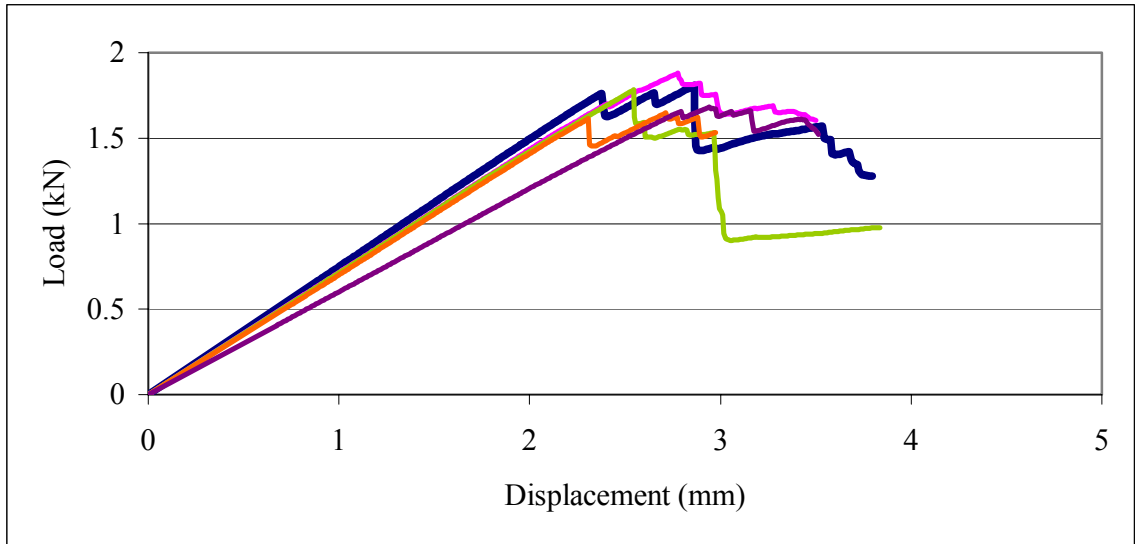Figure D-18. Stress-strain curves for 8 layers plain/glass fabric

148

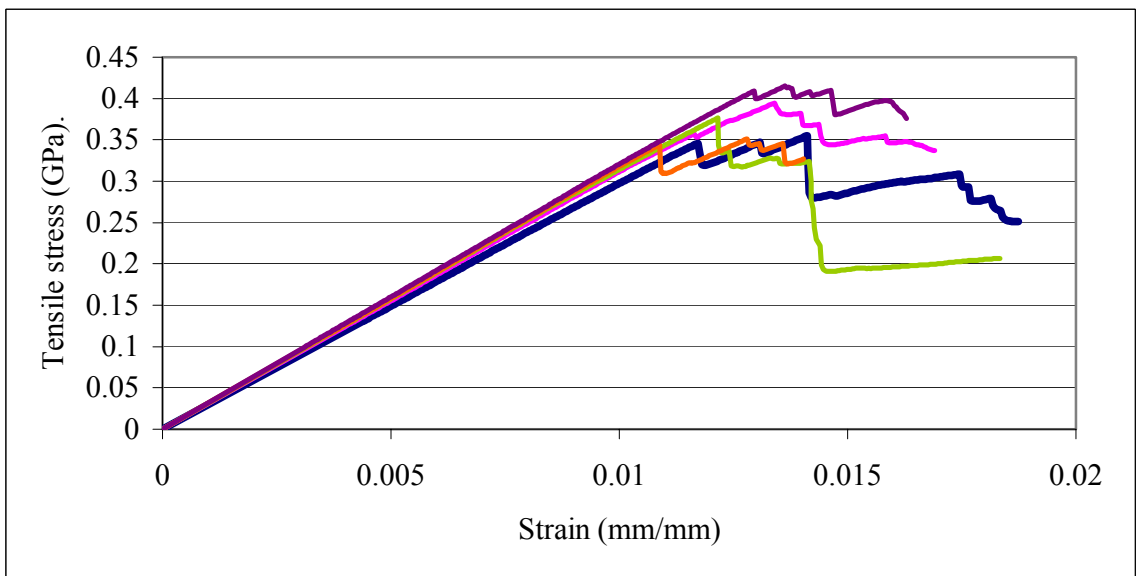Figure D-19. Load-displacement curves for 9 layers plain/glass fabric

Figure D-20. Stress-strain curves for 9 layers plain/glass fabric